ACOUSTIC TRANSDUCTION – MATERIALS AND DEVICES

Period 1 January 1999 to 31 December 1999

Annual Report

VOLUME IV

OFFICE OF NAVAL RESEARCH
Contract No: N00014-96-1-1173

**APPROVED FOR PUBLIC RELEASE –
DISTRIBUTION UNLIMITED**

Reproduction in whole or in part is permitted for any
purpose of the United States Government

Kenji Uchino

20000815 040

THE MATERIALS RESEARCH LABORATORY
UNIVERSITY PARK, PA

REPORT DOCUMENTATION PAGE

Public reporting burden for this collection of information is estimated to average 1 hour per response, including the time for reviewing instructions, searching existing data sources, gathering and maintaining the data needed, and completing and reviewing the collection of information. Send comments regarding this burden estimate or any other aspect of this collection of information, including suggestions for reducing this burden, to Washington Headquarters Services, Directorate for Information Operations and Reports, 1215 Jefferson Davis Highway, Suite 1204, Arlington, VA 22202-4302, and to the Office of Management and Budget, Paperwork Reduction Project (0704-0188), Washington, DC 20503.

1. AGENCY USE ONLY (Leave blank)	2. REPORT DATE 06/12/2000	3. REPORT TYPE AND DATES COVERED ANNUAL REPORT 01/01/2000-12/31/2000

4. TITLE AND SUBTITLE

ACOUSTIC TRANSDUCTION -- MATERIALS AND DEVICES

5. FUNDING NUMBERS

ONR CONTRACT NO.
N00014-96-1-11173

6. AUTHOR(S)

KENJI UCHINO

7. PERFORMING ORGANIZATION NAME(S) AND ADDRESS(ES)

Materials Research Laboratory
The Pennsylvania State University
University Park, PA 16802

8. PERFORMING ORGANIZATION REPORT NUMBER

9. SPONSORING / MONITORING AGENCY NAME(S) AND ADDRESS(ES)

Office of Naval Research   Office of Naval Research
ONR 321SS   Regional Office Chicago
Ballston Centre Tower One 536 S Clark Str., RM 208
800 N Quincy Street   Chicago IL 60605-1588
Arlington VA 22217-5660

10. SPONSORING / MONITORING AGENCY REPORT NUMBER

11. SUPPLEMENTARY NOTES

12a. DISTRIBUTION / AVAILABILITY STATEMENT

12b. DISTRIBUTION CODE

13. ABSTRACT (Maximum 200 words)

SEE FOLLOWING PAGE

14. SUBJECT TERMS

15. NUMBER OF PAGES

16. PRICE CODE

17. SECURITY CLASSIFICATION OF REPORT	18. SECURITY CLASSIFICATION OF THIS PAGE	19. SECURITY CLASSIFICATION OF ABSTRACT	20. LIMITATION OF ABSTRACT
UNCLASSIFIED	UNCLASSIFIED	UNCLASSIFIED	

GENERAL INSTRUCTIONS FOR COMPLETING SF 298

The Report Documentation Page (RDP) is used in announcing and cataloging reports. It is important that this information be consistent with the rest of the report, particularly the cover and title page. Instructions for filling in each block of the form follow. It is important to *stay within the lines* to meet *optical scanning requirements*.

Block 1. Agency Use Only *(Leave blank)*.

Block 2. Report Date. Full publication date including day, month, and year, if available (e.g. 1 Jan 88). Must cite at least the year.

Block 3. Type of Report and Dates Covered. State whether report is interim, final, etc. If applicable, enter inclusive report dates (e.g. 10 Jun 87 - 30 Jun 88).

Block 4. Title and Subtitle. A title is taken from the part of the report that provides the most meaningful and complete information. When a report is prepared in more than one volume, repeat the primary title, add volume number, and include subtitle for the specific volume. On classified documents enter the title classification in parentheses.

Block 5. Funding Numbers. To include contract and grant numbers; may include program element number(s), project number(s), task number(s), and work unit number(s). Use the following labels:

C	- Contract	PR	- Project
G	- Grant	TA	- Task
PE	- Program Element	WU	- Work Unit Accession No.

Block 6. Author(s). Name(s) of person(s) responsible for writing the report, performing the research, or credited with the content of the report. If editor or compiler, this should follow the name(s).

Block 7. Performing Organization Name(s) and Address(es). Self-explanatory.

Block 8. Performing Organization Report Number. Enter the unique alphanumeric report number(s) assigned by the organization performing the report.

Block 9. Sponsoring/Monitoring Agency Name(s) and Address(es). Self-explanatory.

Block 10. Sponsoring/Monitoring Agency Report Number. *(If known)*

Block 11. Supplementary Notes. Enter information not included elsewhere such as: Prepared in cooperation with...; Trans. of...; To be published in.... When a report is revised, include a statement whether the new report supersedes or supplements the older report.

Block 12a. Distribution/Availability Statement. Denotes public availability or limitations. Cite any availability to the public. Enter additional limitations or special markings in all capitals (e.g. NOFORN, REL, ITAR).

> DOD - See DoDD 5230.24, "Distribution Statements on Technical Documents."
> DOE - See authorities.
> NASA - See Handbook NHB 2200.2.
> NTIS - Leave blank.

Block 12b. Distribution Code.

> DOD - Leave blank.
> DOE - Enter DOE distribution categories from the Standard Distribution for Unclassified Scientific and Technical Reports.
> NASA - Leave blank.
> NTIS - Leave blank.

Block 13. Abstract. Include a brief *(Maximum 200 words)* factual summary of the most significant information contained in the report.

Block 14. Subject Terms. Keywords or phrases identifying major subjects in the report.

Block 15. Number of Pages. Enter the total number of pages.

Block 16. Price Code. Enter appropriate price code *(NTIS only)*.

Blocks 17. - 19. Security Classifications. Self-explanatory. Enter U.S. Security Classification in accordance with U.S. Security Regulations (i.e., UNCLASSIFIED). If form contains classified information, stamp classification on the top and bottom of the page.

Block 20. Limitation of Abstract. This block must be completed to assign a limitation to the abstract. Enter either UL (unlimited) or SAR (same as report). An entry in this block is necessary if the abstract is to be limited. If blank, the abstract is assumed to be unlimited.

ABSTRACT

This report describes the research performed over the period of 1 January 1999 to 31 December 1999 on a MURI under Office of Naval Research contract N00014-96-1-1173 on the topic "Acoustic Transduction: Materials and Devices" brings together work from the Materials Research Laboratory (MRL), the Applied Research Laboratory (ARL), and the Center for Acoustics and Vibrations (CAV) at The Pennsylvania State University. As has become customary over many years research on the program is described in detail in the 87 technical appendices to this report and only a brief narrative description connecting this research is given in the text.

Perhaps the most outstanding accomplishment of the year is a "spin on" from our earlier single crystal studies now involving Brookhaven National Laboratory and Professor Gonzalo's group in Madrid, Spain. Using exceptionally homogeneous polycrystal lead zirconate titanate samples prepared in MRL, precise synchotron x-ray analysis has confirmed a new monoclinic phase at lower temperature in composition close to the important morphotropic phase boundary. This work demands a re-thinking of both intrinsic and extrinsic contributions to response in this most important practical transducer material family. Domain Engineering/Domain Averaging in lead zinc niobate:lead titanate (PZN:PT) in lead magnesium niobate:lead titante (PMN:PT) and inn barium titanate (BaTiO$_3$) continues to offer single crystal systems with outstanding transducer and actuator properties and new insights into the field induced strain mechanisms in all perovskite type piezoelectrics. Excellent progress with the new high strain irradiated P(VDF:TrFE) relaxor ferroelectric copolymer system has helped catalyze a new DARPA initiative in this area and a re-awakening of interest in the whole area of electrostrictive polymer systems.

A primary objective of this MURI grouping was to help shorten the time constant for new materials and device concepts to be applied in practical Navy Systems. We believe this has now been realized in joint work on the composite cymbal type flextensional arrays for large area projectors, and in the progress made towards a micro-tonpilz array system.

Original work on new step and repeat piezoelectric high strain systems continues to make good progress now using commercial motion rectifiers to produce both linear and rotary systems with high torque capability. New composite designs are pushing toward 1 mm diameter motors in the size regimen where there are real difficulties for conventional electromagnetic designs.

A new area of activity this year is in piezoelectric transformers where a circular symmetry design in conjunction with controlled inhomogeneous poling is shown to offer capabilities which are of real interest for energy recovery actuator power systems. Basic studies have evolved a new environmental SEM technique for high resolution domain wall studies without changing problems. Work is continuing on reliable measurements of electrostrictive constants in simple solids confirming by both direct and converse methods and permitting the first generalization of trends in these fundamentally important coupling constants.

ACOUSTIC TRANSDUCTION – MATERIALS AND DEVICES

Period 1 January 1999 to 31 December 1999

Annual Report

VOLUME IV

Kenji Uchino

APPENDICES

VOLUME I

GENERAL SUMMARY PAPERS

1. Cross, L.E., "Newnham Festschrift Introduction." Guest Editorial, <u>Mat. Res. Innovations</u> **2**, 251 (1999).

2. Newnham, R.E., "Ceramics into the Next Millennium," *British Ceramic Transactions* **98**(5), 251-255 (1999).

3. Uchino, K. and S. Takahashi, "New Trend in Multilayer Ceramic Actuators," Proc. Int'l Symp. Dielectric Ceramics, Amer. Ceram. Soc. '98; Ceramic Trans., Vol. 100, Dielectric Ceramic Materials, p.455 - 468 (1999).

4. Uchino, K., "Smart Composite Materials," Chap.5.19, Comprehensive Composite Materials, Elsevier Science, Oxford, UK (2000). [in press]

5. Kelly, A., R. Davidson, and K. Uchino "Smart Composite Materials Systems," Chap.5.20, Comprehensive Composite Materials, Elsevier Science, Oxford, UK (2000). [in press]

6. Fousek, J., L.E. Cross, and D.B. Litvin, "Possible Piezoelectric Composites Based on the Flexoelectric Effect." <u>Materials Letters</u> **39**, 287-291 (1999).

2.0 MATERIALS STUDIES
2.1 Polycrystal Perovskite Ceramics

7. Noheda, B., D.E. Cox, G. Shirane, J.A. Gonzalo, L.E. Cross, and S.-E. Park, "A Monoclinic Ferroelectric Phase in the Pb(Zr$_{1-x}$Ti$_x$)O$_3$ Solid Solution." <u>Applied Physics Letters</u> **74**(14), 2059-2061 (1999).

8. Noheda, B., J.A. Gonzalo, R. Guo, S.-E. Park, L.E. Cross, D.E. Cox, and G. Shirane, "The monoclinic phase in PZT: new light on morphotropic phase boundaries," Proceedings of the Workshop on Fundamental Physical of Ferroelectrics, Aspen, CO (February 2000).

9. Noheda, B., J.A. Gonzalo, L.E. Cross, R. Guo, S.-E. Park, D.E. Cox, and G. Shirane, "Tetragonal-to-monoclinic phase transition in a ferroelectric perovskite: The structure of PbZr$_{0.52}$Ti$_{0.48}$O$_3$," *Physical Review B* **61**(13), 8687 (April 2000).

10. Guo, R., L.E. Cross, S.-E. Park, B. Noheda, D.E. Cox, and G. Shirane, "Origin of the high piezoelectric response in PbZr$_{1-x}$Ti$_x$O$_3$," *Physical Review Letters* **84**(23) (June 2000).

11. Zhang, Q.M., "Electromechanical Properties of Lead Zirconate Titanate Piezoceramics Under the Influence of Mechanical Stresses," IEEE Transactions on Ultrasonics, Ferroelectrics, and Frequency Control **46**(6) (November 1999).

12. Wang, H., W. Jiang, and W. Cao, " Characterization of Lead Zirconate Titanate Piezoceramic Using High Frequency Ultrasonic Spectroscopy," <u>J. Appl. Phys.</u> **85**, 8083-8091 (1999).

13. Zhao, J., V. Mueller, and Q.M. Zhang, "The Influence of External Stress on the Electromechanical Response of Electrostrive 0.9PMN-0.1PT in the DC Field Biased State," <u>J. Mater. Res</u>. **14**, 948-956 (1999).

2.0 MATERIALS STUDIES
2.1 Polycrystal Perovskite Ceramics (continued)

14. Zhao, J., A.E. Glazounov, and Q.M. Zhang, "Change in Electromechanical Properties of 0.9PMN-0.1PT Relaxor Ferroelectric Induced by Uniaxial Compressive Stress Directed Perpendicular to the Electric Field," Appl. Phys. Lett. 74, 436-438 (1999).

15. Albert, E.F., A.S. Bhalla, and T. Takenaka, "Large Hydrostatic Piezoelectric Constant and Temperature Dependence of the Piezoelectric Properties $Bi(Ni_{1/2}Ti_{1/2})O_3$:PbTiO$_3$ Ceramics," Ferroelectrics Letters 25, 45-52 (1999).

16. Alberta, E.F. and A.S. Bhalla, "Investigation of the Lead Indium Niobate–Lead Magnesium Niobate Solid Solution," Materials Letters 40, 114-117 (1999).

17. Alberta, E.F. and A.S. Bhalla, "Electrical Properties of the Morphotropic Phase Boundary in $Pb(In_{1/2}Ta_{1/2})O_3$-PbTiO$_3$ Ceramics," Ferroelectrics Letters 26, 117-123 (1999).

18. Kim, J.S., S.J. Kim, H.G. Kim, D.C. Lee, and K. Uchino, "Piezoelectric and Dielectric Properties of Fe_2O_3-Doped $0.57Pb(Sc_{1/2}Nb_{1/2})O_3$-0.43PbTiO$_3$ Ceramic Materials," Jpn. J. Appl. Phys. 38(Part 1, No. 3A), 1433-1437 (1999)..

VOLUME II

19. Liu, S.F., I.R. Abothu, S. Komarneni, P. Poosanaas, D.S. Paik, Y. Ito, and K. Uchino, "PLZT Ceramics Prepared from Conventional and Microwave Hydrothermal Powders," Ferroelectrics 231, 179-185 (1999).

20. Chen, Y. H., S. Hirose, D. Viehland, S. Takahashi, and K. Uchino, "Mn-Modified $Pb(Mg_{1/3}Nb_{2/3})O_3$-PbTiO$_3$ Ceramics: Improved Mechanical Quality Factors for High Power Transduction Applications," Jpn. J. Appl. Phys. (1999). [accepted].

21. Chen, Y.H., S. Hirose, D. Viehland, and K. Uchino, "Doping Effects in $Pb(Mg_{1/3}Nb_{2/3})O_3$-PbTiO$_3$ Ceramics for High Power Transduction Applications," Mater. Res. Soc. Fall Mtg. '99, LL.5.9, Boston (Nov. 29-Dec.3, 1999).

22. Du, X.H., Q.M. Wang, U. Belegundu, and K. Uchino, "Piezoelectric Property Enhancement in Polycrystalline Lead Zirconate Titanate by Changing Cutting Angle," J. Ceram. Soc. Jpn. 107(2), 190-191 (1999).

2.2 Single Crystal Systems

23. Wada, S., S.E. Park, L.E. Cross, and T.R. Shrout, "Engineered Domain Configuration in Rhombohedral PZN-PT Single Crystals and their Ferroelectric Related Properties." Ferroelectrics 221, 147-155 (1999).

24. Liu, S.-F., S.E. Park, T.R. Shrout, and L.E. Cross. "Electric Field Dependence of Piezoelectric Properties for Rhombohedral $0.955Pb(Zn_{1/3}Nb_{2/3})O_3$–0.045PbTiO$_3$ Single Crystals." Journal of Applied Physics 85 (5), 2810-2814 (1999).

25. Erhart, J. and W. Cao, "Effective Material Properties in Twinned Ferroelectric Crystals," J. Appl. Phys. 86, 1073- 1081 (1999).

2.0 MATERIALS STUDIES
2.2 *Single Crystal Systems (continued)*

26. Yin, J., B. Jiang, and W. Cao, "Elastic, Piezoelectric and Dielectric Properties of $0.955Pb(Zn_{1/3}Nb_{2/3})O_3$-$0.045PbTiO_3$ Single Crystal with Designed Multidomains," <u>IEEE Transactions UFFC</u> **47**, 285-291 (2000).

27. Wada, S., S.E. Park, L.E. Cross, and T.R. Shrout, "Defect-induced Domain Configuratrion in Relaxor PZN Single Crystal and Its Origin." <u>Trans. of the Mat. Res. Soc. Of Japan</u> **24**(1), 19-22 (1999).

28. Belegundu, U., X. Du, and K. Uchino, "Switching Current In $Pb(Zn_{1/3}Nb_{2/3})O_3$-$PbTiO_3$ Single Crystals, MRS Meeting, Boston (November 1999).

29. Park, S.-E., S. Wada, L.E. Cross, and T.R. Shrout, "Crystallographically Engineered $BaTiO_3$ Single Crystals for High-Performance Piezoelectrics." <u>Journal of Applied Physics</u> **86**(5), 2746-2750 (1999).

30. Du, X.H., Q.M. Wang, U. Belegundu, A. Bhalla, and K. Uchino, "Crystal Orientation Dependence of Piezoelectric Properties of Single Crystal Barium Titanate," <u>Mater. Lett.</u> **40**, 109-113 (1999).

31. Lu, .Y., Z.-Y. Cheng, E. Park, S.F. Liu and Q.M. Zhang, "Linear Electro-optic Effect of $0.88Pb(Zn_{1/3}Nb_{2/3})$-$0.12PbTiO_3$ Single Crystal," <u>Jpn. J. Appl. Phys</u>. 141-145 (2000).

2.3 *High Strain Polymers*

32. Bharti, V., H.S. Xu, G. Shanthi, Q.M. Zhang, and K. Liang, "Polarization and Structural Properties of High Energy Electron Irradiated P(VDF-TrFE) Copolymer Films," <u>J. Appl. Phys</u>. **87**, 452-461 (2000).

33. Cheng, Z.-Y., T.-B. Xu, V. Bharti, S. Wang, and Q.M. Zhang, "Transverse Strain Response in the Electrostrictive P(VDF-TrFE) Copolymer," <u>Appl. Phys. Lett</u>. **74**, 1901-1903 (1999).

34. Cheng, Z.-Y, V. Bharti, T.B. Xu, S. Wang, Q.M. Zhang, T. Ramotowski, F. Tito, and R. Ting, "Transverse Strain Responses in Electrostrictive P(VDF-TrFE) Films and Development of a Dilatometer for the Measurement," <u>J. Appl. Phys</u>. **86**, 2208-2214 (1999).

35. Bharti, V., Z-Y Cheng, S. Gross, T.B. Xu, and Q.M. Zhang, "High Electrostrictive Strain under High Mechanical Stress in High Energy Electron Irradiated Poly(vinylidene fluoride-trifluoroethylene) Copolymer Films," <u>Appl. Phys. Lett</u>. **75**, 2653-2655 (1999).

3.0 TRANSDUCER STUDIES
3.1 *Composite Structures*

36. Geng, X. and Q.M. Zhang, "Resonance Modes and Losses in 1-3 Composites for Ultrasonic Transducer Applications," <u>J. Appl. Phys</u>. **85**, 1342-1350 (1999).

37. Tressler, J. and K. Uchino, "Piezoelectric Composite Sensors," Chap.5.25, Comprehensive Composite Materials, Elsevier Science, Oxford, UK (2000). [in press]

38. Tressler, J.F., S. Alkoy, A. Dogan, and R.E. Newnham, "Functional Composites for Sensors, Actuators and Transducers," <u>Composites Part A: Applied Science & Manufacturing</u> **30**, 477-482 (1999).

3.0   TRANSDUCER STUDIES
3.1   Composite Structures (continued)

39.   Tressler, J.F. and R.E. Newnham, "Capped Ceramic Underwater Sound Projector: The "Cymbal" Transducer," J. of Acoustical Soc. America **105**(2), part 1, 591-600 (1999).

VOLUME III

40.   Zhang, J., W.J, Hughes., P. Bouchilloux, R. Meyer Jr., K. Uchino, and R.E. Newnham, "A Class V Flextensional Transducer: The Cymbal," Ultrasonics **37**, 387-393 (1999).

41.   Zhang, J., W.J. Hughes, R.J. Meyer Jr., K. Uchino, and R.E. Newnham, "Cymbal Array: A Broad Band Sound Projector," Ultrasonics **37**, 523-529 (2000).

3.0   TRANSDUCER STUDIES
3.1   Composite Structures (continued)

42.   Zhang, J., W.J. Hughes, A.C. Hladky-Hennion and R.E. Newnham, "Concave Cymbal Transducers," Materials Research Innovations **2** (5), 252-255 (1999).

43.   Alkoy, S., R.E. Newnham, A.C. Hladky, A. Dogan, and J.K. Cochran, Jr., "Piezoelectric Hollow Spheres for Microprobe Hydrophones," Ferroelectrics **226**, 11-25 (1999).

44.   Carlson, W.B., R.E. Newnham and D.P. Williams, "Piezotensegritic Structures for Transducer Applications," Materials Research Innovations **3**, 175-178 (1999).

45.   Newnham, R.E. and A. Amin, "Smart Systems: Microphones, Fish Farming, and Beyond," Chemtech **29**(12), 38-47 (1999).

3.2   3-Dimensional Acoustic Intensity Probes

46.   Bastyr, K.J., G.C. Lauchle, and J.A. McConnell, "Development of a Velocity Gradient Underwater Acoustic Intensity Sensor," J. Acoust. Soc. Am. **106**, 3178-3188 (1999).

47.   Lauchle, G.C. and W.A. Kargus, IV, "Scaling of Turbulent Wall Pressure Fluctuations Downstream of a Rearward Facing Step," J. Acoust. Soc. Am. **107**, L1-L6 (2000).

3.3   Piezoelectric Transformers

48.   Koc, B., S. Alkoy, and K. Uchino, "A Circular Piezoelectric Transformer with Crescent Shape Input Electrodes," Proc. IEEE Ultrasonic Symp., Lake Tahoe, Nevada, Oct. 17-21 (1999).

49.   Koc, B. and K. Uchino, "Disk Type Piezoelectric Transformer with Crescent Shape Input Electrodes," Proc. NATO- Advanced Research Workshop: Piezoelectric Materials, Advance in Science, Technology and Applications, Predeal, Romania (May 24-27, 1999).

4.0 ACTUATOR STUDIES
4.1 Materials and Designs

50. Uchino, K., "Recent Trend of Piezoelectric Actuator Developments," Proc. Int'l Symp. Micromechatronics and Human Science '99, p.3-9, Nagoya, Japan (Nov. 23-26, 1999).
51. Yao, K., W. Zhu, K. Uchino, Z. Zhang and L.C. Lim, "Design and Fabrication of a High Performance Multilayer Piezoelectric Actuator with Bending Deformation," **46** (4), 1020-1027 (1999).
52. Wang, Q.-M., X.-H. Du, B. Xu, and L.E. Cross, "Electromechanical Coupling and Output Efficiency of Piezoelectric Bending Actuators." IEEE Transactions on Ultrasonics, Ferroelectrics, and Frequency Control **46** (3), 638-646 (1999).
53. Wang, Q.-M. and L.E. Cross, "Analysis of High Temperature Reduction Processing of RAINBOW Actuator." Materials Chemistry and Physics **58**, 20-25 (1999).
54. Glazounov, A.E., Q.M. Zhang, and C. Kim, "Torsional Actuator Based on Mechanically Amplified Shear Piezoelectric Response," Sensors and Actuators **A79**, 22-30 (2000).
55. Yoo, J.-H., J.-I Hong, and W. Cao, "Piezoelectric Ceramic Bimorph Coupled to Thin Metal Plat as Cooling Fan for Electronic Devices," Sensors and Actuators **79**, 8-12 (1999).

4.2 Photostriction

56. Poosanaas, P., K. Tonooka and K. Uchino, "Photostrictive Actuators," J. Mechatronics (1999) [in press].
57. Poosanaas, P. and K. Uchino, "Photostrictive Effect in Lanthanum-Modified Lead Zirconate Titanate Ceramics near the Morphotropic Phase Boundary," J. Mater. Chem. and Phys. **61**, 36-41 (1999).

VOLUME IV

4.3 High Force Torsional Actuators

58. Frank, J.E., G.H. Koopmann, W. Chen, and G.A. Lesieutre, "Design and Performance of a High Force Piezoelectric Inchworm Actuator," Proceedings of SPIE 6th Annual International Symposium on Smart Structures and Materials, 1999.
59. Koopmann, G.H., G.A. Lesieutre, J. Frank, and W. Chen, "Design and Performance of a Linear Piezoelectric Wedgeworm Actuator," Piezoelectric Materials: Advances in Science, Technology and Applications, 383-390 (2000).
60. Frank, J. E.M. Mockensturm, W. Chen, G.H. Koopmann, and G.A. Lesieutre, "Roller-Wedgeworm: A Piezoelectrically-Driven Rotary Motor," 10th International Conference on Adaptive Structures and Technologies, Paris (October 1999).

4.4   Piezoelectric Mini Motors

61.   Glazounov, A.E., S. Wang, Q.M. Zhang, and C. Kim, "High Efficiency Piezoelectric Motor Combining Continuous Rotation with Precise Control Over Angular Positioning," Appl. Phys. Lett. **75**, 862-864 (1999).

62.   Uchino, K. and B. Koc, "Compact Piezoelectric Ultrasonic Motors," Ferroelectrics **230**, 73-86 (1999).

63.   Kim, J.S., M.J. Park, and K. Uchino, "Composite Ultrasonic Motors Using a Piezoelectric Disk and an Elastic Body of "Windmill" Type," Ferroelectrics **232**, 185-190 (1999).

64.   Koc. B., P. Bouchilloux, and K. Uchino, "Piezoelectric Micromotor Using A Metal-Ceramic Composite Structure," IEEE Trans. Ultrasonic, Ferroelectrics, and Frequency Control (1999).

5.0   MODELING and CHARACTERIZATION
5.1   Simulation

65.   Cao, W., S. Tavener, and S. Xie, "Simulation of Boundary Condition Influence in a Second-Order Ferroelectric Phase Transition," J. Appl. Phys. **86**, 5739-5746 (1999).

66.   Shen, M. and W. Cao, "Acoustic Band-Gap Engineering Using Finite Size Layered Structures of Multiple Periodicity," Appl. Phys. Lett. **75**, 3713-3715 (1999).

67.   Uchino, K., and H. Aburatani, "Field Induced Acoustic Emission in Ferroelectric Ceramics," Proc. 101st Annual Mtg. of Amer. Ceram. Soc., Symp. Dielectric Materials and Devices, SE-56, Indianapolis, April 25 - 28 (1999). [accepted]

68.   Uchino, K., J. Zheng, Y.H. Chen, X. Du. S. Hirose, and S. Takahashi, "Loss Mechanisms in Piezoelectrics—Extrinsic and Intrinsic Losses." Mater. Res. Soc. Fall Mtg. '99, LL.1.6, Boston, Nov. 29-Dec.3 (1999).

69.   Uchino, K. and S. Hirose, "Loss Mechanisms in Piezoelectrics," submitted to *IEEE UFFC Transactions* (1999).

VOLUME V

70.   Uchino, K., J. Zheng, Y.H. Chen, X. Du, and S. Hirose, "Loss Mechanisms in Piezoelectrics," Mater. Res. Soc. Fall Mtg. '99, Boston (Nov. 29-Dec.3, 1999).

5.2   Thin and Thick Films

71.   Abothu, I.R., Y. Ito, P. Poosanaas, S. Kalpat, S. Komarneni, and K. Uchino, "Sol-Gel Processing of Piezoelectric Thin Films," Ferroelectrics **232**, 191-195 (1999).

72.   Kalpat, S., I.R. Abothu, A. Akiba, H. Goto, S. Trolier-McKinstry, and K. Uchino, "Dielectric and Piezoelectric Property Dependence on Highly Textured (100), (111) and Random Thin Films Grown by RF Sputtering," Symp. LL Proc., Mater. Res. Soc. Fall Mtg. '99, LL.1.3, Boston, Nov. 29-Dec.3 (1999).

73.   Xu, F., F. Chu, and S. Trolier-McKinstry, "Longitudinal Piezoelectric Coefficient Measurement for Bulk Ceramics and Thin Films Using Pneumatic Pressure Rig," J. Appl. Phys. **86** (1) 588 -594 (1999).

5.0   MODELING and CHARACTERIZATION

5.2   Thin and Thick Films (continued)

74.   Shepard, J. F., Jr., F. Chu, I. Kanno, and S. Trolier-McKinstry, "Characterization and Aging Response of the d_{31} Piezoelectric Coefficient of Lead Zirconate Titanate Thin Films," J. Appl. Phys. **85**(9), 6711-6716 (1999).

75.   Xu, B., Y. Ye, L.E. Cross, J.J. Bernstein, and R. Miller, "Dielectric Hysteresis from Transverse Electric Fields in Lead Zirconate Titanate Thin Films." Applied Physics Letters **74** (23), 3549-3551 (1999).

76.   Xu, B., R.G. Polcawich, S. Trolier-McKinstry, Y. Ye, L.E. Cross, J.J. Bernstein, and R. Miller, "Sensing Characteristics of In-Plane Polarized Lead Zirconate Titante Thin Films," Applied Physics Letter **75** (26), 4180 (December 1999).

77.   Xu, B, L.E. Cross, and D. Ravichandran, "Synthesis of Lead Zirconate Titanate Stannate Antiferroelectric Thick Films by Sol-Gel Processing." J. Am. Ceramic Soc. **82** (2), 306-312 (1999).

78.   Xu, B., Y. Ye, Q.-M. Wang, and L.E. Cross, "Dependence of Electrical Properties on Film Thickness in Lanthanum-Doped Lead Zirconate Titanate Stannate Antiferroelectric Thin Films." Journal of Applied Physics **85** (7), 3753-3758 (1999).

5.3   Domain Studies

79.   Belegundu, U., X.H. Du, A. Bhalla, and K. Uchino, "Effect of Electric Field on Domain Formation in Relaxor Based $Pb(Zn_{1/3}Nb_{2/3})O_3$-$PbTiO_3$ Single Crystals, Ferroelectrics Letters **26** (5-6), 107-116 (1999).

80.   Belegundu, U., X.H. Du, L.E. Cross and K. Uchino, "In Situ Observation of Domains in $0.9Pb(Zn_{1/3}Nb_{2/3})O_3$-$0.1PbTiO_3$ Single Crystals," Ferroelectrics 221, 67-71 (1999). (First Author Supervised by Candidate).

81.   Hatch, D.M. and W. Cao, "Determination of Domain and Domain Wall Formation at Ferroic Transitions," Ferroelectrics **222**, 1-10 (1999).

82.   Cao, W. and S.N. Zhu, "Observation of Ferroelectric Domains in $LiTaO_3$," Ferroelectrics **226**, 27-35 (1999).

83.   Zhu, S.N. and W. Cao, "Imaging of 180 Ferroelectric Domains in $LiTaO_3$ by Scanning Electron Microscopy," Phys. Stat. Sol. (a) **173**, 495-502 (1999).

84.   Mueller, V., H. Beige, and Q.M. Zhang, "Nonlinear Ferroelectric Domain Wall Response," Ferroelectrics **222**, 295-302 (1999).

85.   Liu, R., R. Guo, A.S. Bhalla, L.E. Cross, M. Levy, and R.M. Osgood Jr., "Optical Observation of Dynamic Ferroelectric Phase Transition and Static Domain Structures in Crystal Ion Sliced (CIS) $LiNbO_3$ Film." Materials Letters **39**, 264-267 (1999).

5.4   Electrostriction

86.   Eury, S., R. Yimnirun, V. Sundar, P.J. Moses, S.J. Jang, and R.E. Newnham, "Converse Electrostriction in Polymers and Composites," Mat. Chem. and Phys. **61**, 18-23 (1999).

87.   Yimnirun, R., S.M-L. Eury, V. Sundar, P.J. Moses, S. Jang, and R.E. Newnham, "Electrostriction Measurement on Low Permittivity Dielectric Materials," Journal of European Ceramics Society **19**, 1269-1273 (1999).

ACTUATOR STUDIES

Torsional and High Force Actuators

APPENDIX 58

Design and Performance of a
High Force Piezoelectric Inchworm Motor

Jeremy Frank, Gary H. Koopmann, Weiching Chen, and George A. Lesieutre

Center for Acoustics and Vibration, Penn State University, University Park, PA 16802

ABSTRACT

A linear inchworm motor was developed for applications in adaptive, conformable structures for flow control. The device is compact (82 x 57 x 13 mm), and capable of unlimited displacement and high force actuation (150 N). The static holding force is 350 N. Four piezoceramic stack elements (two for clamping and two for extension) are integrated into the actuator, which is cut from a single block of titanium alloy. Actuation is in the form of a steel shaft pushed through a precision tolerance hole in the device. Unlimited displacements are achieved by repetitively advancing and clamping the steel shaft. Although each step is only on the order of 10 microns, a step rate of 100 Hz results in a speed of 1 mm/s. Since the input voltage can readily control the step size, positioning on the sub-micron level is possible.

Keywords: Inchworm actuator, piezoceramic actuator, piezoelectric actuator

1. INTRODUCTION

The possible applications of a high force, high displacement linear actuator are numerous, and the development of such a device has received considerable attention in recent years, as evidenced by the patents disclosed.[1-16] Two types of linear piezoelectric actuators, 'quasi-static inchworm' and 'ultrasonic travelling wave' have been most common.[17-22] With the goal of improving the maximum dynamic actuation force, the quasi-static inchworm actuator was developed to actuate adaptive, conformable structures in flow control systems (Figure 1).
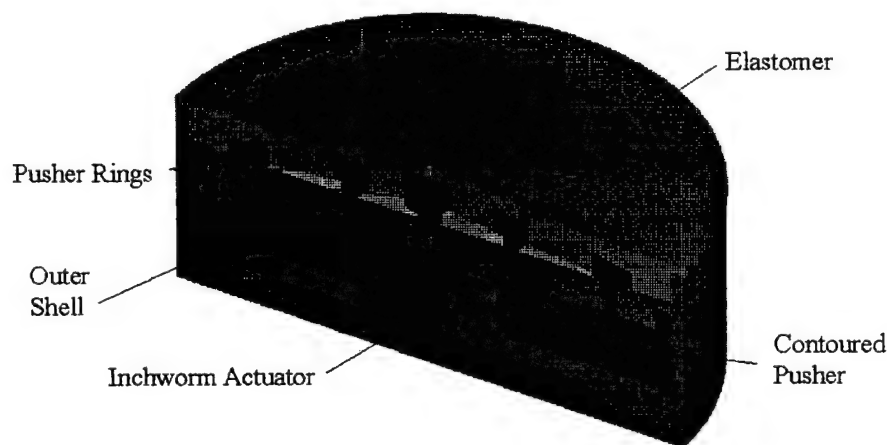

Figure 1 Application of the actuator in a flow control structure

Pusher Rings

Outer Shell

Inchworm Actuator

Elastomer

Contoured Pusher

Further author information –
J.F.: Email: jef@kirkof.meche.psu.edu Ph.D. candidate - Correspondence: Telephone: 814-865-7262; Fax: 814-863-4592
G.H.K.: Email: ghk@kirkof.meche.psu.edu Professor, Director of the Center of Acoustics and Vibration
W.C.: Email: chen@kirkof.meche.psu.edu Research Associate
G.A.L.: Email: g-lesieutre@psu.edu Associate Professor, Associate Director, CAV

2. DESIGN OF THE INCHWORM ACTUATOR

In previous designs, the dynamic actuation force has been limited by machining clearance issues and passive clamping schemes. With the current design, similar to a design investigated by Daimler-Benz,[23] we achieve higher forces by using the piezoceramic stacks to directly clamp a shaft, and by minimizing the tolerance between the shaft and the structure. As seen in Figure 2, the design concept consists of four integrated piezoceramic stacks, two for clamping and two for extension. The structure of the actuator consists of an outer frame, and an inner block which is able to move vertically on structural monolithic springs. In step 1, the lower clamping stack is energized, clamping the steel shaft to the inner block. Next, in step 2 the pushing stacks are energized, lifting the inner block and steel shaft a distance of 10 to 15 microns. Finally, the upper clamping stack is energized, clamping the shaft to the outer frame. At the same time, the lower clamping stack and the pushing stacks are de-energized, allowing the spring flexures to return the inner block to its original position, ready for the next step. When this process is repeated at high frequency, motion is achieved.

Figure 2 Conceptual schematic of the inchworm actuator

Using 21 mm long PZT stacks, poled in the d_{33} direction, the blocked force is 2000 N with a corresponding free defection of approximately 20 microns (see Figure 3). Because of the small deflection, any clearance between the clamp and the shaft will result in a significant loss of potential clamping force. For this reason, the hole through which the steel shaft passes is reamed, ground and honed to as precise a tolerance as possible. The shaft is of hardened, precision ground stainless steel, and is chosen specifically to match the machined hole. This procedure reduces the tolerance between the shaft and the hole to about 5 microns, resulting in a minimized loss of clamping force.
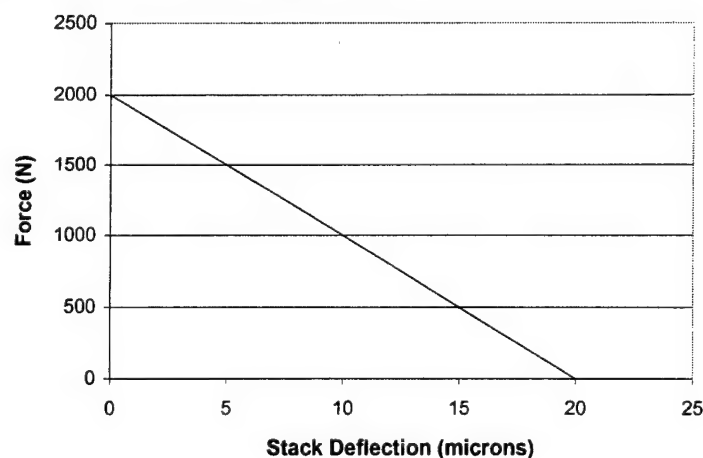

Figure 3 Force/displacement characteristics of the piezoceramic stacks

A picture of the prototype actuator is shown in Figure 4. The structure is cut using an EDM process from a single block of titanium alloy, resulting in a sleek design with no assembly necessary. Of particular interest are the monolithic flexures, also

cut directly out of the material, that allow relative motion of the moving parts. The inner block of the titanium frame, for example, is connected to the outer frame only by four monolithic flexures. These flexures allow vertical motion but not horizontal motion of the inner block, and provide the necessary pre-compression force to the piezoceramic stacks. This force prevents the stacks from receiving a tensile load, which is known to cause failure. The two clamping stacks are also pre-compressed into the frame with monolithic flexures. The flexures support the upper and lower clamp (seen in Figure 4), which provide the clamping force on the shaft when the stacks are energized. The clamp flexures also support the vertical shear load, which must not be supported by the piezoceramics.

Figure 4 Photograph of the inchworm actuator

3. TESTING THE PROTOTYPE ACTUATOR

The prototype actuator was tested to characterize its performance. The variables of the signals driving the stacks included waveform shape, level, duty cycle and relative phasing. With a need for flexibility in mind, LABVIEW software was used to generate inchworm drive signals through a PC digital to analog output board. A typical set of drive signals, seen in Figure 5, shows that the pusher stacks are driven with a sine wave while the clamping stacks are driven with overlapping square waves. Since the clamping mechanism is only active when the piezoceramics are energized, the overlap in the clamp signals is necessary to prevent backslip when actuating an external force. The use of square waves as drive signals limits the upper range of available drive frequencies by inducing higher order longitudinal resonances in the piezoceramic stacks.[22.] However, only a square wave can provide the signal overlap that is essential to ensure clamping of the shaft at all times.
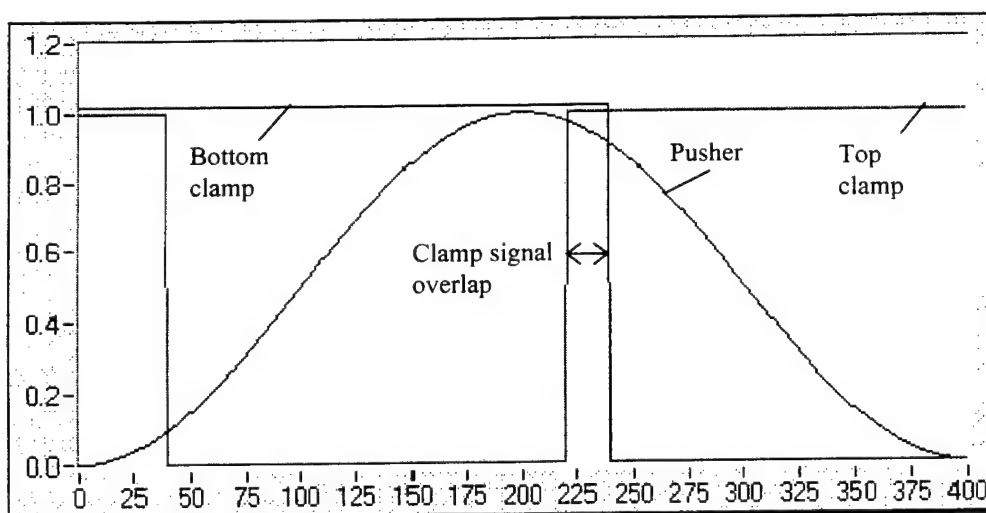
Figure 5 Typical drive signals generated with LABVIEW

A special-purpose calibration fixture is used for characterization of the inchworm, as shown in Figure 6. Its main feature is a stiff beam pivoted on one end in a precision bearing. The fixture is able to selectively drive loads that are primarily inertial in nature, primarily stiffness in nature, or a combination of both. The beam can be driven against a compression spring for a stiffness load, or a mass can be attached to the beam to increase the inertial load. A high-sensitivity strain gauge load cell and an LVDT position transducer are used to measure performance. Further, an analog to digital input board is used to record the output force and velocity in LABVIEW, a feature of the experimental setup that will eventually enable closed-loop operation of the inchworm.

Figure 6 Schematic of the inchworm actuator performance characterization experiment

Three initial experiments were devised to characterize the actuator's speed, holding force and dynamic force. First, the actuator was driven against no load and the velocity was measured as a function of drive frequency. As seen in Figure 7, the behavior was fairly linear up to about 150 Hz, increasing to 1.2 mm/s. Above 150 Hz however, the square clamping signals began to cause problems, and the performance degraded.
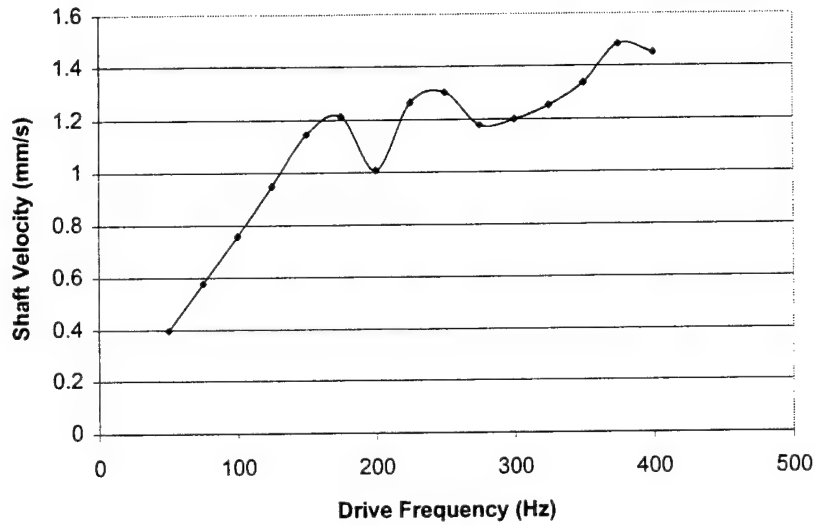
Figure 7 Free velocity of the actuator as a function of drive frequency

Next, the static holding force of the clamps was determined by applying a DC voltage to one clamping stack and measuring the load at which the shaft slips backward. As seen in Figure 8, the voltage was increased up to 100 V and a corresponding increase in holding force was observed. The two clamps were tested independently and displayed similar but not identical performance, probably because of variations in machining tolerance. This indicates that even tiny imperfections in machining can result in a significant loss of performance. The static holding force of the top and bottom clamps are shown to be 275 N and 375 N, respectively.

Figure 8 Static holding force of the clamps

Next, the dynamic drive signals were used to actuate the shaft against a spring load to measure the maximum dynamic force, or stall load. The maximum force was measured as a function of the input voltage to both the clamping and pushing stacks, which was increased up to 124 V. As shown in Figure 9, the stall force increased linearly with the voltage input to a maximum value of about 130 N. The power amplifiers were unable to generate square waves at more than 124 V, but for the voltage limitation of the piezoceramics (150 V) the maximum dynamic pushing force can be extrapolated to about 155 N. Although this force is high, it is disappointing in that it is more than 100 N lower than the measured static holding force. The loss in dynamic force is probably a result of unwanted oscillations of the piezoceramics, caused by the square wave excitation.
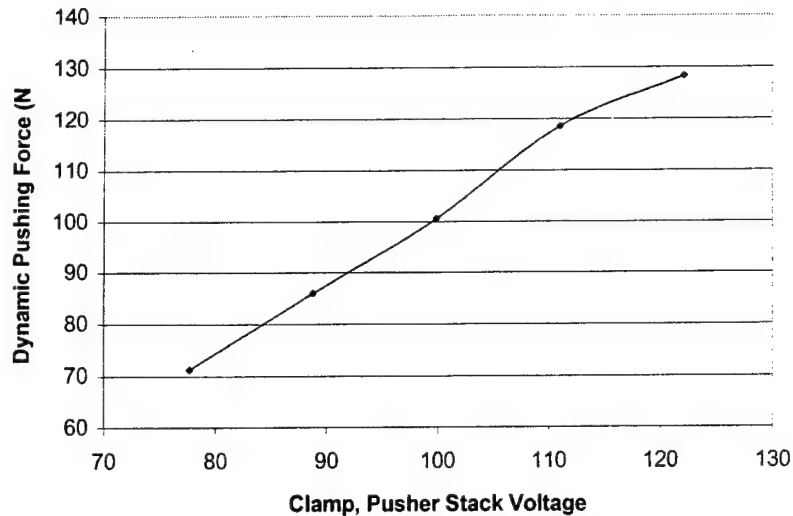
Figure 9 Maximum dynamic pushing force (stall load) as a function of input voltage

With evidence that the square waves were causing limitations in dynamic holding force, we tried alternative signal shapes in order to improve performance. First, sine waves were used to drive both the pushing and the clamping stacks. As expected, the motion was quieter than with square waves, since the clamps were gradually clamping onto the shaft. However, the driving force was limited to less than 60 N (see Figure 10) because of the lack of overlap in the clamp signals. For applications where high speed but low force is required, sinusoidal signals could be used, since the smoother clamping mechanism allows the actuator to be driven at much higher frequencies. In the next part of the experiment, ramped square waves were used to drive the clamps in order to remove the high frequency problems caused by the square waves. The ramped square signals were really square waves with sine waves spliced in between. The hope was that the ramped waves could provide the necessary overlap between the clamp signals but eliminate the problems caused by the discontinuous square wave. As seen in Figure 10, the ramped waves achieved better stall loads than the sinusoidal signals, but did not perform as well as square waves. From this experiment it was determined that although the square waves reduce the dynamic force capability of the actuator, they are needed to cause the necessary overlap between the clamping signals.
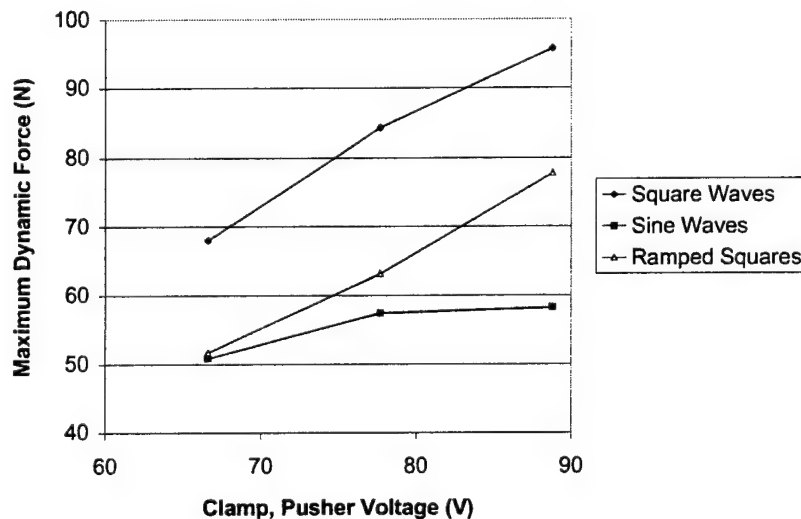

Figure 10 Dynamic force tests for alternative clamping signals

4. CONCLUSIONS

A linear inchworm motor was developed for structural shape control applications. Features of the subject device include small size (82 x 57 x 13 mm), unlimited stroke, speeds of about 1 mm/s, dynamic forces approaching 150 N, and static holding force capability greater than 275 N. The device is machined as one continuous structure with monolithic flexures, and actuates a steel shaft through its center. Large displacements are achieved by repetitively advancing and clamping the shaft. The dynamic actuation force, although high, is limited by the use of square waves in the driving signals. Other types of signals were tried, but did not improve the stall load.

ACKNOWLEDGEMENTS

REFERENCES

1. R. Stibitz, "Incremental Feed Mechanisms", *U.S. Patent: 3,138,749*, 1964.
2. J.T. McNancy, "Piezoelectric transducer force to motion converter", *U.S. Patent: 2,154,700* 1964.
3. K. Hsu, and A. Biatter, "Transducer", *U.S. Patent: 3,292,019*, 1966.
4. G.L. Locher, "Micrometric linear actuator", *U.S. Patent:* 3,296,467, 1967.
5. A.D. Brisbane, "Position control device", *U.S. Patent: 3,377,489,* 1968.
6. G.V. Galutva, "Device for precision displacement of a solid body", *U.S. Patent: 3,684,904* 1972.
7. R.A. Bizzigotti, "Electromechanical translational apparatus", *U.S. Patent: 3,902,085,* 1975.
8. Y. Sakitani, "Stepwise fine adjustment", *U.S. Patent: 3,952,215,* 1976.
9. Ishikawa, and Y. Sakitani, "Two-directional piezoelectric driven fine adjustment device", *U.S. Patent: 4,163,168,* 1979.
10. G. O'Neill, "Electromotive actuator", *U.S. Patent: 4,219,755,* 1980.
11. T. Taniguchi, "Piezoelectric driving apparatus", *U.S. Patent: 4,454,441*, 1984.
12. A. Hara, H. Takao, Y. Kunio, T. Sadayuki, and N. Keiji, "Electromechanical translation device comprising an electrostrictive drive of a stacked ceramic capacitor type", *U.S. Patent: 4,570,096,* 1986.
13. C.W. Staufenberg, Jr., and R.J. Hubbell, "Piezoelectric electromechanical translation apparatus", *U.S. Patent: 4,622,483,* 1986.
14. T. Fujimoto, "Piezo-electric actuator and stepping device using same", *U.S. Patent: 4,714,855* 1987.
15. T. Murata, "Drive apparatus and motor unit using the same", *U.S. Patent: 4,974,077,* 1990.
16. G. Rennex, "Inchworm actuator", *U.S. Patent: 5,3323,942*, 1994.
17. J.E. Meisner and J.P. Teter, "Piezoelectric/magnetostrictive resonant inchworm motor". *SPIE,* Vol. 2190, pp. 520-527, 1994.
18. S.K. Lee and M. Esachi, "Design of the electrostatic linear microactuator based on the inchworm motion", *Mechatronics.* Vol. 5, No. 8, pp. 9653-972, 1995.
19. T. Funakubo, T. Tsubata, Y. Tanigughi, and K. Kumei, "Ultrasonic linear motor using multilayer piezoelectric actuators", *Japanese Journal of Applied Physics*, Vol. 34, Part 1, No. 5B, pp. 2756-2759, May 1995.
20. T. Pandell and E. Garcia, "Design of a piezoelectric caterpillar motor", *Proceedings of the ASME aerospace division.* AD-Vol. 52, pp. 627-648, 1996.
21. T. Galante, "Design and fabrication of a high-force linear piezoceramic actuator", M.S. thesis, Penn State University, August 1997.
22. D. Newton, E. Garcia, and G. C. Horner, "A linear piezoelectric motor", *Smart Materials and Structures*, Vol. 7, No. 3, pp. 295-304, June 1998.
23. W. Martin, Daimler-Benz, Private communication, January 1998.

APPENDIX 59

DESIGN AND PERFORMANCE OF A LINEAR PIEZOELECTRIC WEDGEWORM ACTUATOR

GARY H. KOOPMANN, GEORGE A. LESIEUTRE, JEREMY
FRANK, AND WEICHENG CHEN
Center for Acoustics and Vibration
157 Hammond Building,
Penn State University, University Park, PA 16802

Abstract

A new concept in linear piezoelectric actuators is developed for applications in adaptive, conformable structures for flow control. Motivated by a desire for high actuation force (>1kN) and simplified drive signals, the design takes advantage of self-locking wedges to lock the clamping elements. The concept relies heavily on knowledge and manipulation of the friction coefficients between several surfaces, so the choice of coatings and lubricants are a major part of the investigation. Since the wedges are self-locking in one direction, the actuation force is limited only by the size of the piezoceramic and the strength of the actuator structure. The device contains a single piezoceramic stack (8x8x42 mm, PZT 5H), so the drive signals and amplifiers are drastically simplified from previous designs. A prototype of the concept is developed and experimentally tested. At a drive frequency of 200 Hz, the free velocity is 8 mm/s with a travel of 25 mm. An actuation force of 250 N is achieved with the prototype. The wedge concept also reduces the amount of precision necessary in machining and assembling the device.

1. Introduction

The possible applications of a high force, high displacement linear actuator are numerous, and the development of such a device has received considerable attention in recent years, as evidenced by the patents disclosed.[1-16.] The clamping mechanism in most of the designs consists of a piezoceramic element clamping directly (more or less) onto a moving part. Since the displacements of the piezoceramics are usually on the order of 10-20 microns, this means that the machining accuracy must be within a few microns to ensure a high clamping force (Figure 1a). Such tight tolerances can be very expensive, and any inaccuracy quickly leads to a loss of actuation force. The new
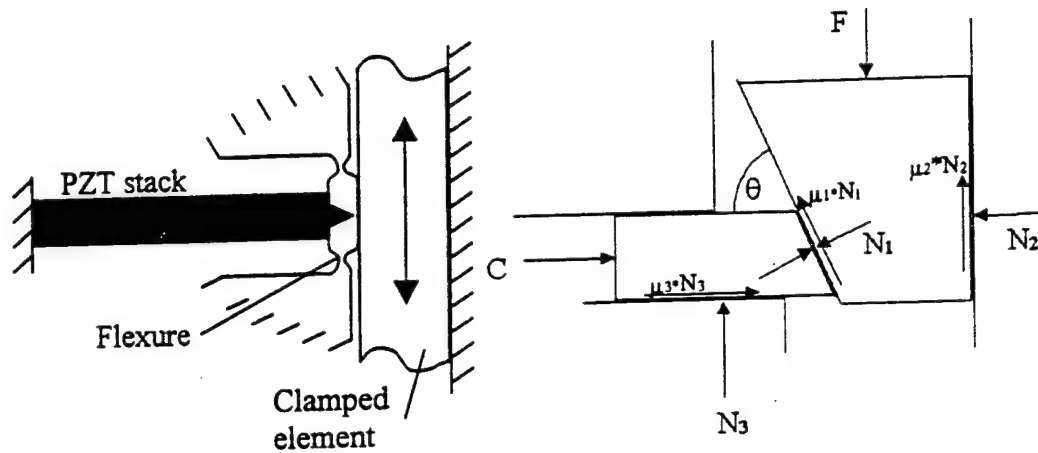
384

Figure 1 a) Direct clamping method   b) Passive wedge clamping method

wedge concept employs a passive mechanism for clamping, relaxing the need for low surface tolerances and eliminating the piezoelectric clamping stacks (Figure 1b). For certain values of the parameters shown the wedge will lock, preventing the upper block from sliding down.

2.   Design of the Wedgeworm Actuator

The motion of a wedgeworm actuator is quite similar to that of previously designed inchworm-type linear actuators[17-23.] (Figure 2). A central pusher element consisting of two halves is separated by the piezoelectric stack and held together by flexures cut from the structure. The flexures are used to apply a pre-compressive force to the stack, necessary to keep the stack from going into tension. As seen in Figure 1b), the left wedges are constrained to move horizontally and are in contact with the pusher surface such that the surfaces are self-locking and the pusher cannot slide down. For this schematic, the right wedges are not in contact with the pusher. The right and left wedges are rigidly attached and pulled left or right such that only one set or the other is in contact with the pusher at any time. Here, the left wedges are pulled to the right by a spring force, keeping them in constant contact with the pusher. Motion of the device is as follows: 1) The piezoceramic stack is de-energized and the pusher is locked in place by the left wedges. 2) The stack is energized with voltage. The bottom of the pusher is locked by the clamp and cannot move down, but the top is able to extend up. As the pusher moves up, the top left wedge moves to the right so that contact is maintained. 3) The stack is de-energized. Now, the top is locked in the extended position, so the flexures pull the bottom of the pusher up, completing one step. This time, the bottom left wedge moves to the right to maintain contact with the pusher. The process is repeated at a high driving frequency (~200 Hz) to give a high actuation rate and smooth motion.
In order to use the wedge concept as an actuator clamping mechanism, it is necessary to understand the physics that make the wedges self-locking. The equilibrium equations
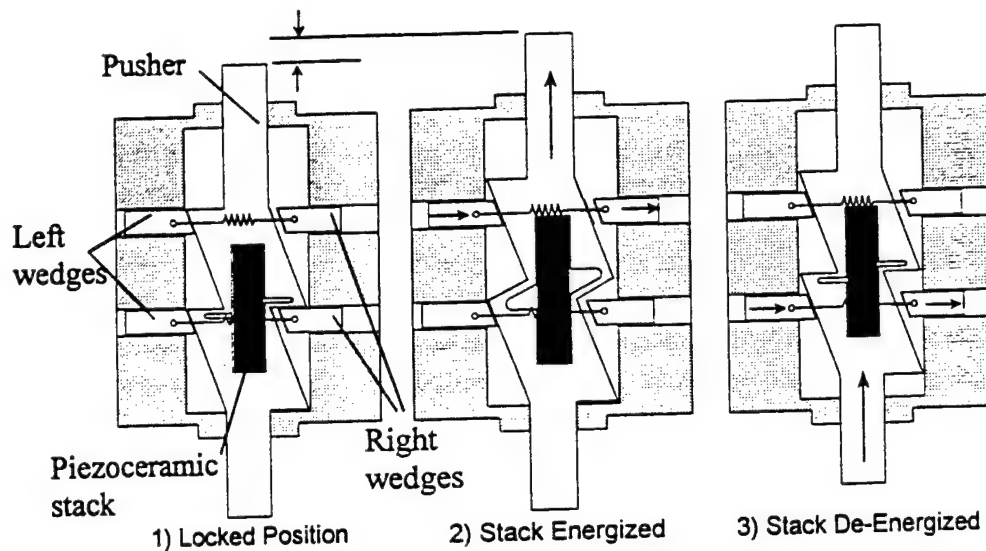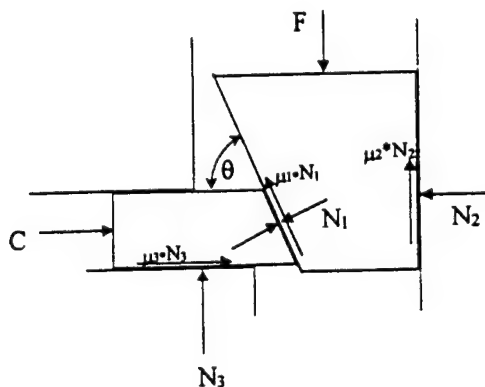
Figure 2 Operational mechanism of the wedgeworm concept

for a static system consisting of two wedges can be simplified to a single equation relating two applied forces on the wedges, C and F (Figure 3). If the ratio is negative the wedges are self-locking. If C/F is positive, then a downward force F must be supported by a horizontal force C, so the wedges are not self-locking. In Figure 3, the self-locking equation is a function of the coefficient of friction at three contacting surfaces and the wedge angle. As a possibility for unlocking the wedge for two-way motion, a change in the coefficient of friction at the wedge interface is assumed. This could be accomplished by extending a teflon (low friction) pad from the wedge surface with a piezoceramic stack. For the actuator to have the maximum amount of travel, the wedge angle θ should be as high as possible. The problem is subject to two constraints, however. First, the self-locking equation must be negative (locked) using the original friction parameters. With the teflon pad extended, the equation should be positive (not locked), which gives the second constraint on the parameters. A non-linear simulated annealing optimization routine is used to maximize the wedge angle subject to the self-locking and non-self-locking constraints. A summary of the optimization problem is shown in Figure 4. The objective function is to maximize

$$\frac{C}{F} = \frac{(1 - \mu_1 \mu_3) \cdot \sin\theta - (\mu_1 + \mu_3) \cdot \cos\theta}{(\mu_1 + \mu_2) \cdot \sin\theta + (1 - \mu_1 \mu_2) \cdot \cos\theta}$$

Where

- F = axial load
- C = applied force on the wedge
- μ = coefficient of friction
- θ = wedge angle

Figure 3 Self-locking wedge equilibrium equation

Note that in the equation, this means that μ_1 is replaced with μ_S, the friction coefficient for teflon. There are five variables in the problem: the wedge angle and four friction coefficients (three original contacting surfaces and one for teflon). Shown in Figure 4, the permissible range for the wedge angle is from 0 to 90 degrees. The chosen range for the friction coefficients is 0.002 to 0.78, selected as maximum and minimum realistic friction values from handbooks. This range has since been shown to be difficult to realize in practice for machined and/or coated surfaces, particularly the upper limit on friction. The program uses a non-linear optimization technique to maximize the wedge angle by varying the four friction coefficient values. The solution always indicated that the coefficients μ_1 and μ_3 should be as high as possible, while the teflon (slipping) coefficient μ_S should be as low as possible (Figure 5a). Interestingly, μ_2, the vertical friction surface, also went to the lower bound, indicating that the vertical sliding surface should be lubricated. With a reasonably high safety factor, the maximized wedge angle was just over 65 degrees (Figure 5b), so this was chosen as the actuator wedge angle. To ensure a smooth horizontal sliding surface for the wedges, hardened steel rods were integrated into the wedgeworm frame (Figure 6). The device is 12 cm in length, but could be made smaller with a structurally optimized structure.

$$\max(\theta) \qquad \min(-\theta)$$

$$g_1(x) = \frac{(1 - \mu 1 \cdot \mu 3)\cdot\sin\theta - (\mu 1 + \mu 3)\cdot\cos\theta}{(\mu 1 - \mu 2)\cdot\sin\theta + (1 - \mu 1 \cdot \mu 2)\cdot\cos\theta} \quad < SF$$

$$g_2(x) = \frac{(1 - \mu S\cdot\mu 3)\cdot\sin\theta - (\mu S + \mu 3)\cdot\cos\theta}{(\mu S - \mu 2)\cdot\sin\theta + (1 - \mu S\cdot\mu 2)\cdot\cos\theta} \quad > SF$$

$$0.0 < \theta < 90.0$$
$$0.002 \; < \mu 3 < 0.78$$
$$0.002 \; < \mu S < 0.78$$
$$0.002 \; < \mu 1 < 0.78$$
$$0.002 \; < \mu 2 < 0.78$$

Figure 4 Optimization problem statement

3. Testing the Prototype Actuator

The prototype wedgeworm actuator was tested to characterize its performance. Since the wedgeworm clamping mechanism is passive, the drive signal is a single frequency sinusoid that could be generated with a simple circuit. This is one of the this is that the only values to vary in experimental characterization experiments are
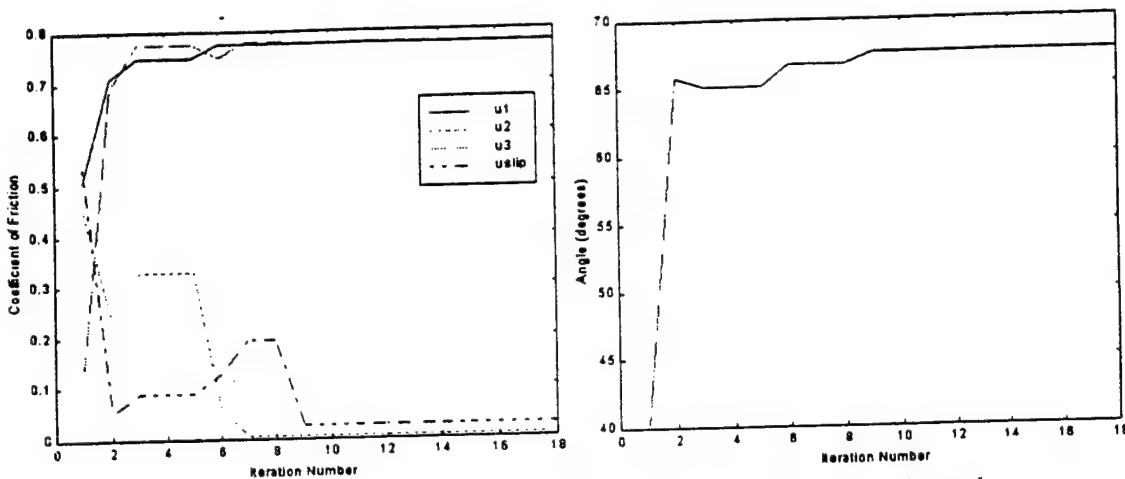
Figure 5 Optimization results showing a) friction coefficients, and b) wedge angle
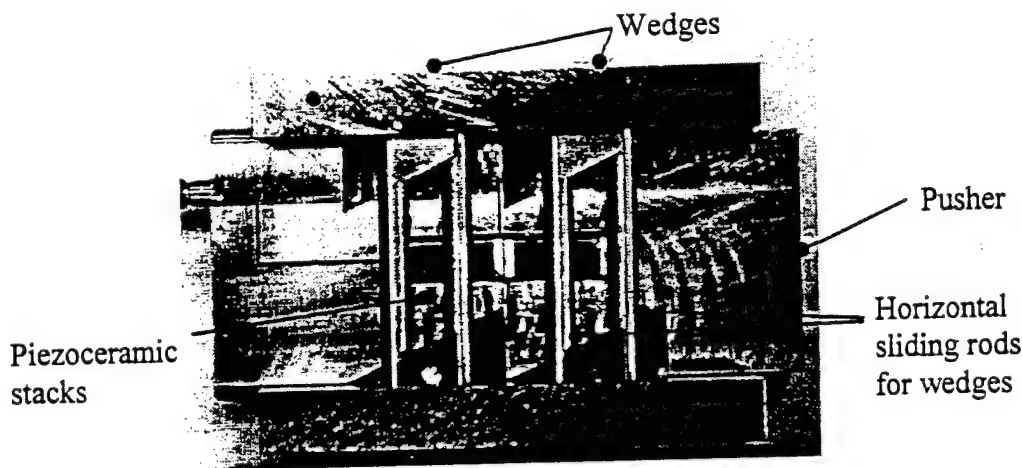

Figure 6 The prototype wedgeworm actuator

the signal voltage and frequency. To characterize the wedgeworm prototype, the free velocity (driving against no load) is first measured as a function of the drive signal frequency. The drive voltage (peak-to-peak, positively biased) is held constant at 144 V. This corresponds to an electric field of 11.5 kV/cm. As seen in Figure 7, the actuator velocity increases linearly with drive frequency. This is expected since the step size should remain constant with frequency, while more steps per second are taken as the drive frequency is increased. At a drive frequency of 200 Hz, the measured free velocity is 8.1 mm/s. It seems that higher speeds would be possible if the frequency were increased further, but the amplifier power limit was reached at 200 Hz. A velocity of 8.1 mm/s at 200 Hz corresponds to a step size of 40.5 microns, which approaches the theoretical free displacement of the stack, 42 microns. Thus, it seems that the backlash under no load is almost zero for the wedgeworm prototype. Next the maximum actuation force, or stall load, was measured as a function of drive voltage. The actuator was driven with a 100 Hz signal with a positively biased peak-to-peak voltage varying from 65 V to 150.
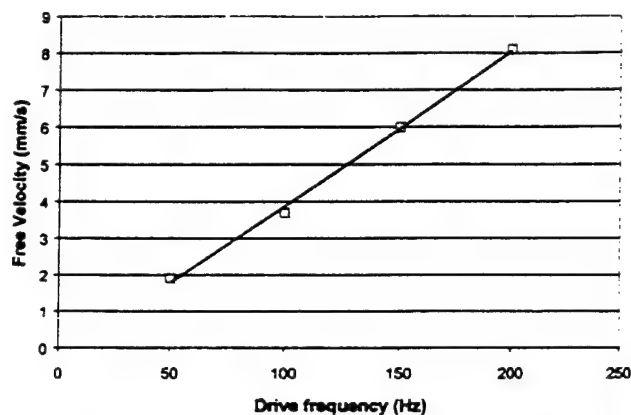
388

Figure 7 Free velocity of the wedgeworm vs. drive frequency

V (the maximum drive voltage for the stacks). The actuator pushed against a compression spring, and was allowed to push until a stall condition occurred Using the original wedge surfaces (stainless steel on stainless steel with $\mu = 0.3$), the maximum actuation force was 240 N for a 150 V drive signal. In an attempt to increase the stall load, a thin, hard coating of aluminum oxide was applied to the wedge surfaces. The intent was to increase the coefficient of friction at the wedge interface, thereby increasing the actuation force. As seen in Figure 8, the maximum actuation force increased with drive voltage to 246 N at 150 V, so the actuation force was not increased significantly with the aluminum oxide coating. The relationship between stall load and drive voltage is not quite linear, and seems in fact to be approaching a limit around 275 N. This indicates that as the actuation force becomes very high there may be some slip in the wedge clamps, limiting the stall load.
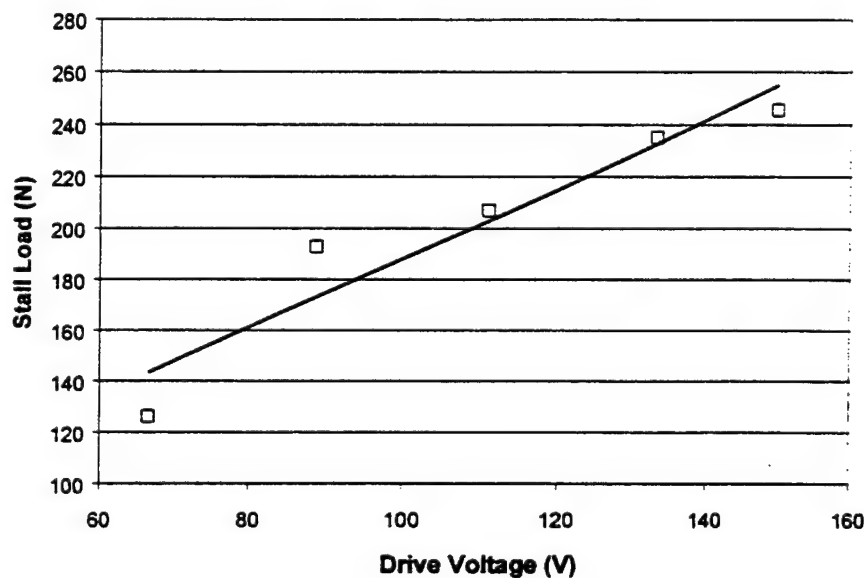

Figure 8 Maximum actuation force vs. drive signal voltage

4. Conclusions

A linear wedgeworm actuator was developed for structural shape control applications. Features of the subject device include very simple drive signals, high actuation force, high speed, and relaxed machining tolerances. An optimization procedure is used to determine the optimal friction surfaces and wedge angle to use in the design. A prototype actuator was built and shown to have a maximum actuation force of 250 N and a free velocity of 8 mm/s at a drive frequency of 200 Hz.

5. Acknowledgements

6. References

1. Stibitz, R. (1964) Incremental Feed Mechanisms, *U.S. Patent:* 3,138,749.
2. McNancy, J.T. (1964) Piezoelectric transducer force to motion converter, *U.S. Patent:* 2,154,700.
3. Hsu, K. and Biatter, A. (1966) Transducer, *U.S. Patent:* 3,292,019.
4. Locher, G.L. (1967) Micrometric linear actuator, *U.S. Patent:* 3,296,467.
5. Brisbane, .A.D (1968) Position control device, *U.S. Patent:* 3,377,489.
6. Galutva, G.V. (1972) Device for precision displacement of a solid body, *U.S. Patent:* 3,684,904.
7. Bizzigotti, R.A. (1975) Electromechanical translational apparatus, *U.S. Patent:* 3,902,085.
8. Sakitani, Y. (1976) Stepwise fine adjustment, *U.S. Patent:* 3,952,215.
9. Ishikawa, and Sakitani, Y. (1979) Two-directional piezoelectric driven fine adjustment device", *U.S. Patent:* 4,163,168.
10. O'Neill, G. (1980) Electromotive actuator, *U.S. Patent:* 4,219,755.
11. Taniguchi, T. (1984) Piezoelectric driving apparatus, *U.S. Patent:* 4,454,441.
12. Hara, A. Takao, H. Kunio, Y. Sadayuki, T. and Keiji, N. (1986), Electromechanical translation device comprising an electrostrictive drive of a stacked ceramic capacitor type, *U.S. Patent:* 4,570,096.
13. Staufenberg, C.W. Jr., and Hubbell, R.J. (1986) Piezoelectric electromechanical translation apparatus, *U.S. Patent:* 4,622,483.
14. Fujimoto, T. (1987), Piezo-electric actuator and stepping device using same, *U.S. Patent:* 4,714,855.
15. Murata, T. (1990), Drive apparatus and motor unit using the same, *U.S. Patent:* 4,974,077.
16. Rennex, G. (1994), Inchworm actuator, *U.S. Patent:* 5,3323,942.
17. Meisner J.E. and Teter, J.P. (1994) Piezoelectric/magnetostrictive resonant inchworm motor. *SPIE*, Vol. 2190, pp. 520-527.
18. Lee S.K. and Esachi, M. (1995) Design of the electrostatic linear microactuator based on the inchworm motion, *Mechatronics.* Vol. 5, No. 8, pp. 9653-972.
19. Funakubo, T. Tsubata, T. Tanigughi, Y. and Kumei, K. (1995), "Ultrasonic linear motor using multilayer piezoelectric actuators", *J. J. of Appl. Phys.*, Vol. 34, Part 1, No. 5B, pp. 2756-2759.
20. Pandell T. and Garcia, E. (1996), Design of a piezoelectric caterpillar motor, *Proceedings of the ASME aerospace division.* AD-Vol. 52, pp. 627-648.

390

21. Galante, T. (1997), Design and fabrication of a high-force linear piezoceramic actuator, M.S. thesis, Penn State University..

22. Newton, D., Garcia, E., Horner, G.C. (1998) A linear piezoelectric motor *Smart Materials and Structures* 7, 3, 295-304.

23. J. Frank, G.H. Koopmann, G.A. Lesieutre, and W. Chen, (1999), "Design and performance of a high force piezoelectric inchworm-type actuator", Proceedings of SPIE's 6th Annual International Symposium on Smart Structures and Materials, Vol. 3668.

APPENDIX 60

ROLLER-WEDGEWORM: A PIEZOELECTRICALLY-DRIVEN ROTARY MOTOR

Jeremy Frank
Eric M. Mockensturm
Weiching Chen
Gary H. Koopmann
George A. Lesieutre[+]

Penn State University, Center for Acoustics and Vibration

Abstract

A new rotary motor that uses a piezoelectric ceramic drive element is described. The main principle underlying its operation is rectification of a small cyclic displacement of the active piezoelectric element using a mechanical diode. The specific device described, about the size of an audio cassette tape, consists of an active stack, a mechanism by which to convert linear motion of the stack to rotary motion of a shaft, and two over-running roller clutches. To obtain rotary motion, the stack is driven with an oscillatory signal. On the driving half of each cycle, the forward motion of the working end of the stack is converted to rotation of the shaft when the stack torque exceeds that of the load. On the recovery (over-running) half of each cycle, a second, fixed, roller clutch prevents the load from back-driving the shaft. Experiments to date have demonstrated steady torques of about 0.5 N-m and speeds of about 450 RPM.

Introduction

Considerable research has addressed the use of smart (or active) materials such as piezoelectric ceramics for solid-state induced-strain actuation [Crawley and de Luis, 1987]. The actuation *energy density* of an active material, approximately proportional to the product of blocked stress and free strain, is a suitable figure-of-merit for comparing the relative performance of alternate drive materials [Giurgiutiu and Rogers, 1996]. The *specific energy density*, the volumetric energy density divided by the material density, may be a more appropriate metric for applications in which weight is more critical than volume. Corresponding effective material *power densities* may be defined by multiplying by a drive frequency.

When used in a device, some kind of generalized *lever* ("motion amplification") system is often required to maximize energy transfer ("stiffness-match") to a deformable elastic load [Giurgiutiu and Rogers, 1997]. Additional parasitic volume and weight is associated with this lever system, making the energy density of a device smaller than that of the active material used in it.

In many realistic applications having volume or weight constraints, the actuation energy density available from solid-state induced-strain materials or devices is inadequate [Lesieutre and Koopmann, 1998]. In these cases, it is sensible to consider the use of smart materials as the active drive elements in non-solid state, large-stroke devices such as motors. Examples of such generalized motors include inchworms [Chen *et al.* 1997; Duong and Garcia, 1996; Frank *et al.* 1999; Teter *et al.*, 1998; Zhang, 1999], ultrasonic wave motors [Glenn and Hagood, 1997; Uchino, 1998], and pumps [Mauck and Lynch, 1999]. In all of these devices, the active elements

[+] 233 Hammond, University Park, PA 16802, USA; 1-814-863-0103; g-lesieutre@psu.edu

are driven in an oscillatory manner (sometimes at high frequency, sometimes at resonance), and some means of <u>rectification</u> is provided to develop one-sided motion. Often, this rectification method involves some kind of generalized diode: pumps use check valves, while inchworms and wave motors use friction-based clamps. *Power density* and *specific power density* are more appropriate figures-of-merit for such motors than energy density, as their performance is usually rate-, not stroke-, limited.

In a motor-type device, some kind of generalized *gearing* system may also be used to maximize power transfer ("impedance-match") to a load. Additional parasitic volume and weight is associated with such a gearing system, as well as with the method used to rectify oscillatory motion, making the power density of a device smaller than that of the active material used in it.

Finally, the development of smart materials-based motors invites comparisons to competing approaches such as hydraulics and electric motors. Consulting a catalog of commercial motors under 100 hp (75 kW) leads to a rough power density of 100 W/kg for typical electric motors. Electric motors and piezoelectric material-based motors have an advantage over hydraulic systems in that power may be transferred over long distances with relatively light wires. Piezoelectric material-based motors have advantages over typical electric motors in that they offer better potential to conform with geometric requirements associated with tightly-integrated adaptive structures, and in the potential for reduced electromagnetic field generation.

Background: Piezoelectric Inchworm Motors

Figure 1 shows a canonical piezoelectric linear stepping motor ("inchworm"), comprising two clamping elements (considered to be in fixed locations) along with a central "pusher" element capable of length changes and of sliding relative to the clamps.
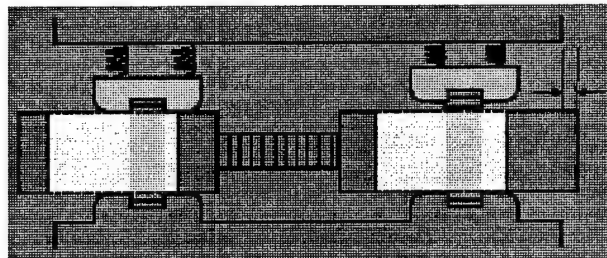

Figure 1. A piezoelectric inchworm motor

One cycle of motion proceeds as follows:

      (1) The right clamp is released;
      (2) The pusher element, held in place on the left, is extended;
      (3) The right clamp is engaged, holding the pusher element in place on the right;
      (4) The left clamp is released;
      (5) The pusher element, held in place on the right, is contracted; and
      (6) The left clamp is engaged.

With typical piezoelectric stack lengths on the order of 2 cm, typical (quasi-static) maximum step sizes are on the order of 20 μm. Large strokes may be obtained by taking repetitive steps.

2

If the steps are taken at high rates, substantial stroke rates are possible. For example, a step rate of 1000 Hz combined with a step size of 20 μm yields a rate of 2 cm/sec. Note that fixed-frequency operation offers some potential for optimizing and miniaturizing the necessary drive electronics.

In order to compete effectively with alternative technology, the output power density of piezoelectric motors must be increased. The keys to high power density in such motors are high-frequency operation, along with rectification of small solid-state oscillatory motion.

Output power is the product of force and stroke rate. In piezoelectric inchworm stepping motors, the maximum output force is the lower of the pushing or holding force capability. The pushing force is proportional to the cross-sectional area of the driving piezoelectric element. The holding force capability of the clamping mechanism has typically been the limiting factor for such devices, and has motivated considerable continuing research.

The maximum stroke rate, however, being the product of the maximum step size (proportional to length) and maximum quasi-static step rate (limited by the resonance frequency, inversely proportional to length), is roughly independent of length scale. Ignoring parasitic mass, the maximum quasi-static stroke rate is given roughly by

$$\text{maximum velocity} \propto \frac{1}{4} c \, \varepsilon_{max} \tag{1}$$

where c is the speed of a longitudinal wave in the active material, and ε_{max} is the maximum free strain. For typical piezoelectric ceramic materials, this quantity is on the order of 1.2 m/s. Due to parasitic mass and other non-idealities, such rates are not approached in practice by quasi-static stepping devices.

Thus, increased power density is obtained by using short piezoelectric elements for maximum drive frequency. An approximate expression for specific power density, ignoring parasitic effects, is given by

$$\text{specific power density} \propto \frac{1}{8} \left(\frac{Y}{\rho} \right)^{3/2} \varepsilon_{max}^2 L^{-1} \approx \frac{1}{8} c^3 \, \varepsilon_{max}^2 L^{-1} \tag{2}$$

In addition, in real devices, the holding element is critical. Ideally, the clamping system behaves as a mechanical diode, permitting selective motion in one direction. Real holding mechanisms exhibit backlash and/or low stiffness over some small (seating) range of motion. Because the step size must be somewhat larger than the backlash in the clamping system, a piezoelectric drive element cannot be so small that its free displacement is smaller than the backlash.

Maximum power density is therefore more realistically obtained by using a piezoelectric drive element that is as short as practical, as limited by the backlash, and running it at as high a frequency as possible. Figure 2 illustrates this concept, with numerical results based on the following assumptions: 0.05 deg (3 arcmin) backlash; a stack blocked force of 3500 N; a moment arm of 1.5 cm; quasi-static driving at half the stack resonance frequency (about 5 kHz

3

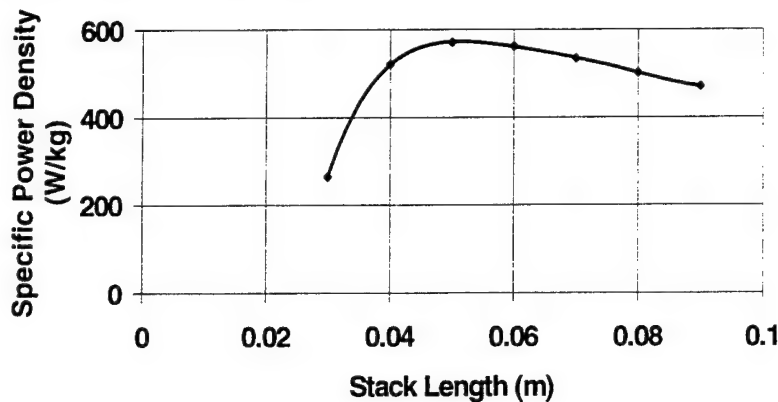for 0.05 m); and a total mass equal to three times that of the stack.

Figure 2. Specific Power Density is limited by backlash for short stacks
and by low frequency operation for long stacks

Note that very high frequency operation associated with very small devices could also result in substantial heating, the effects of which have not been considered. Furthermore, in applications requiring the coordinated efforts of many small devices to deliver substantial total power to a macroscopic load, there is likely to be some additional parasitic mass and volume involved.

Performance of Some Piezoelectric Stepping Motors

Continuing research at the Penn State Center for Acoustics and Vibration (CAV) has pursued the development of high force piezoelectric stepping motors [Frank, Chen, Lesieutre, and Koopmann, 1999]. These motors have evolved considerably over time, primarily in the approach used to perform the clamping function. Holding mechanisms initially relied entirely on Coulomb friction ("inchworm"), then on a combination of friction and mechanical advantage ("wedgeworm"), and currently on mechanical interference ("roller-wedgeworm").

This section summarizes the performance of several of these previous piezoelectric stepping motors.

Figure 3 shows the "H3C inchworm." It functions very much like the canonical inchworm shown in Figure 1 and described in the preceding section. It uses a direct frictional clamp that is initially pre-loaded, so the device is locked with power off. At a peak drive level of 120 Vpp, and a step rate of about 500 Hz, it delivers a maximum 45 N of dynamic force, with a maximum (no load) velocity of about 6 mm/sec. The static holding force is substantially higher.

Three stacks are required, each with appropriate control signals. Typically, the clamps are driven with near-square waves to maximize clamping force, while the pusher is driven with a harmonic signal. Performance of the device is somewhat sensitive to the phase of the pusher signal relative to that of the clamp signals, and the optimum phase angle is load-dependent. The design of the device limits its stroke to about 10 mm.
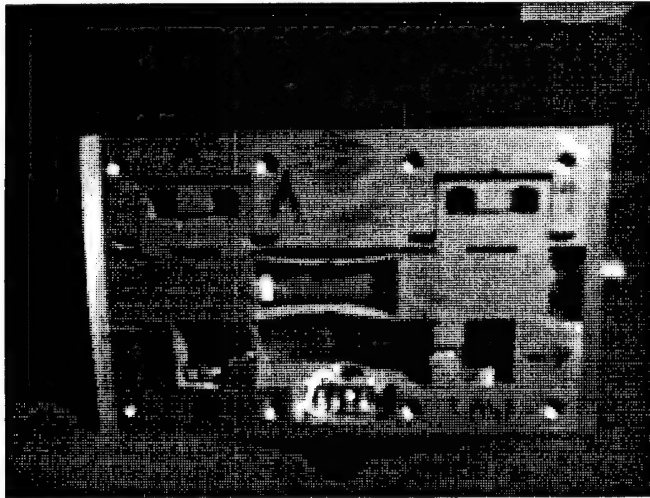
4

Figure 3. The H3C Inchworm

Figure 4 shows the "H3DB" inchworm. It differs from the H3C in several ways. It consists of a single block of material machined so that an inner platform is suspended from an outer base by a set of flexures.
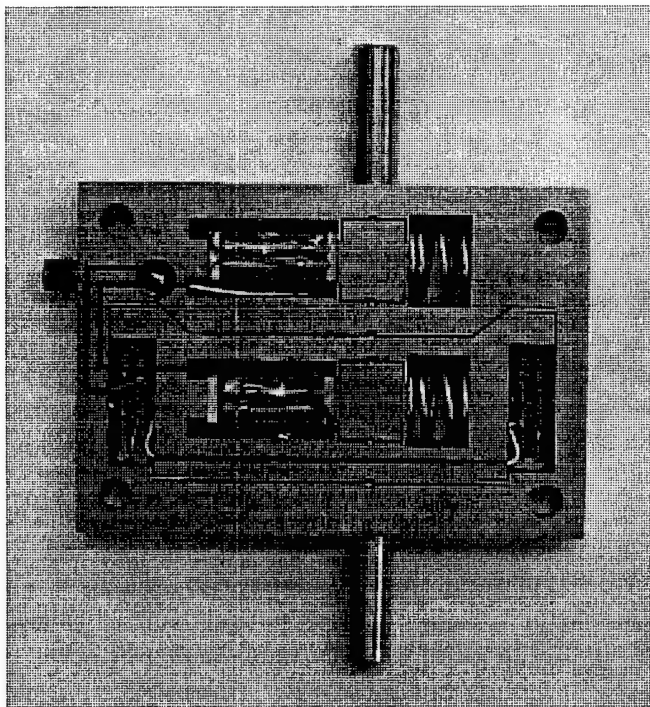

Figure 4. The H3DB Inchworm

The device operates to move a shaft through the block, with very large total stroke. Single stacks on the floating platform and on the outer base activate direct frictional clamps onto the shaft. There is a small tight-tolerance clearance between the clamp face and the shaft. Two stacks move the floating platform relative to the outer base.

At a near-peak drive level of 120 V_{pp}, and a step rate of about 100 Hz, the H3DB delivers a maximum 130 N of dynamic force, with a maximum (no load) velocity of about 1.5 mm/sec, along with very accurate position control. Asymmetry in the pusher drive system is probably the cause of this relatively low speed. Static holding force is on the order of 450 N. Tight tolerance machining makes this device relatively expensive, and the effects of wear on long-term performance is an issue.

The next device in the succession of piezoelectric stepping motors was built to explore an alternative clamping mechanism. As shown in Figure 5, it aims to exploit the concept of a "self-locking taper." For some combinations of wedge geometry (θ) and interface coefficients of friction (μ), no force (C) is required at the clamp to resist the load (F). Devices built using this principle were termed "wedgeworms."
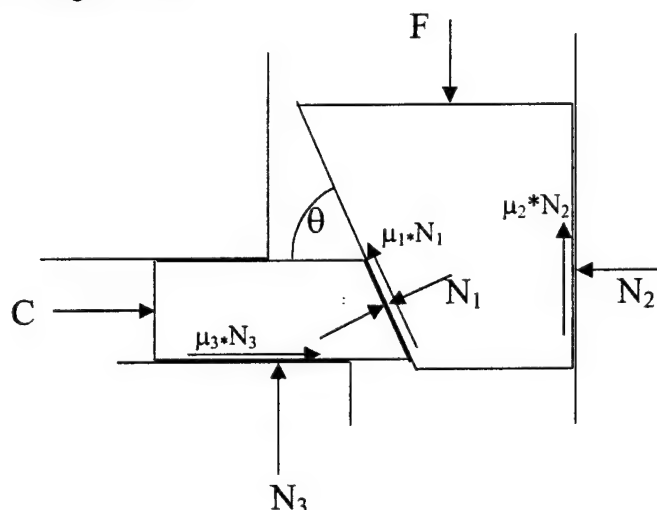

Figure 5. A Self-Locking Taper

Figure 6 shows the "Wedgeworm I." The wedge clamping mechanism is intended to function essentially as a mechanical diode, that is, it cannot be back-driven. Because of uncertainties in wedge angles and coefficients of friction, the wedging mechanism did not work perfectly.

At a drive level of 150 V_{pp}, and a step rate of about 200 Hz, it delivers a maximum 250 N of dynamic force, with a maximum (no load) velocity of about 10 mm/sec. The static holding force is substantially higher. Because of the wedge geometry, the stroke is limited to about 25 mm. One of the main advantages of this design is that only a single stack is required for forward motion. It can be effectively driven using a single fixed-frequency harmonic signal. By switching the active wedges from one side to the other, reversible motion may be obtained.
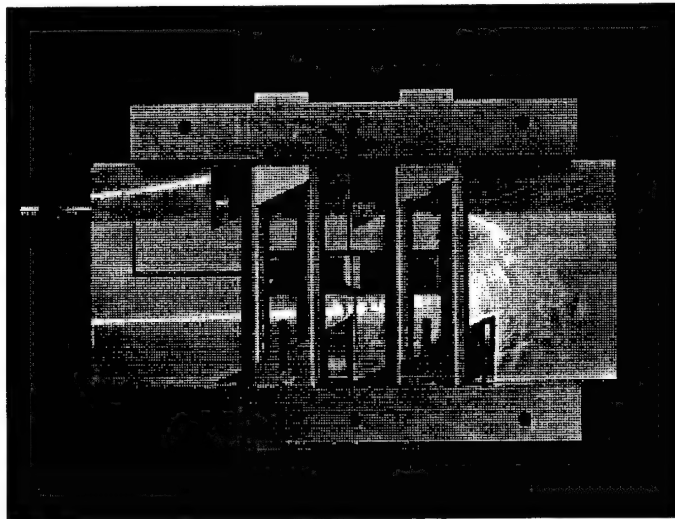
Figure 6. The Wedgeworm I

Figure 7 shows a concept for the "Wedgeworm II." The primary difference from the Wedgeworm I is that the wedging clamps now move along with the central pusher assembly, instead of moving perpendicular to the side wall. These wedges are held in place by preloaded springs. The pusher of the Wedgeworm II essentially moves along a rigid channel that reacts the wedging loads.
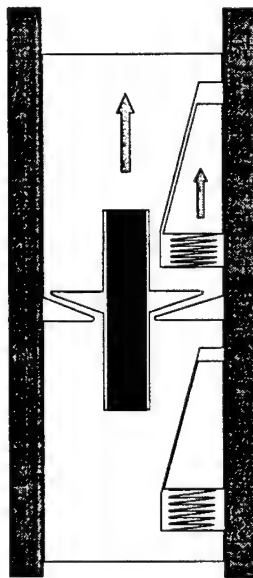

Figure 7. The Wedgeworm II

The next stage in device evolution involved recognizing that the wedge, which still relies to some extent on friction to operate, could be replaced by a rolling element. In this situation, mechanical interference, not friction, provides the primary clamping force. Figure 8 illustrates this concept.
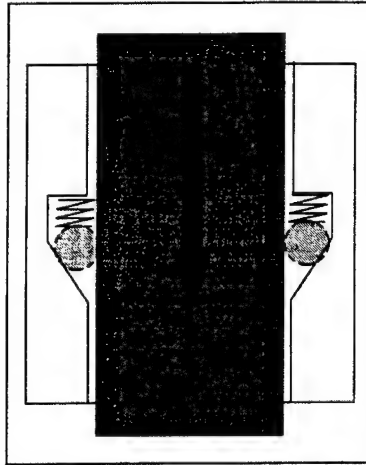
7

Figure 8. A Linear Roller-Wedge

Figure 9 shows a device built to exploit this concept. This wedging mechanism provides an effective mechanical diode, especially in an axisymmetric configuration in which the interfercial wedging loads can be carried as hoop stresses in an outer retaining ring.
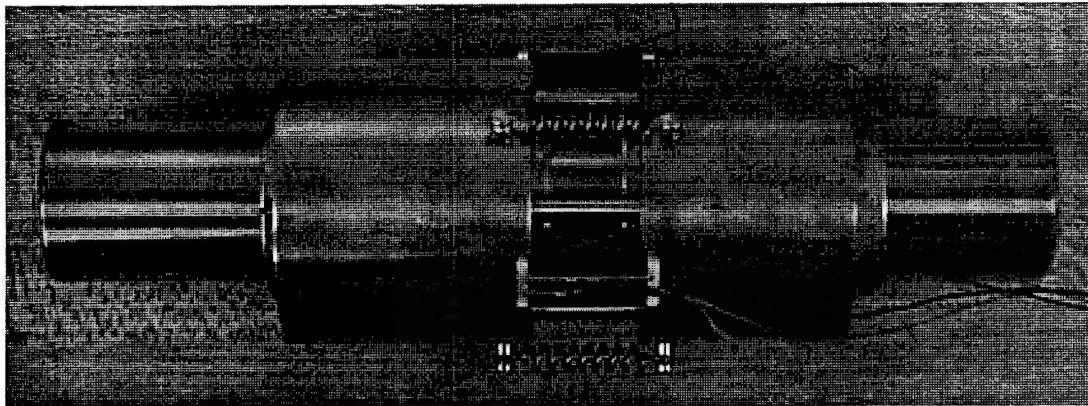

Figure 9. A Linear Roller-Wedgeworm

A Rotary Roller-Wedgeworm

A recent evolutionary design is a rotary roller-wedgeworm. This device is built around a commercial over-running roller clutch, a rotary version of the linear roller-wedge shown in Figure 8. Figure 10 shows a schematic of a roller clutch. Initial experimental measurements of roller clutch performance indicate a typical angular backlash of about 0.3 deg.

Figure 11 shows a rotary roller-wedgeworm device. It consists of an active stack, a mechanism to convert linear motion of the stack to rotary motion of a shaft, and two roller clutches. To obtain rotary motion, the stack is driven with an oscillatory signal. On the driving half of each cycle, the forward motion of the working end of the stack is converted to rotation of the shaft when the stack torque exceeds that of the load. On the recovery (over-running) half of each cycle, a second roller clutch prevents the load from backdriving the shaft.
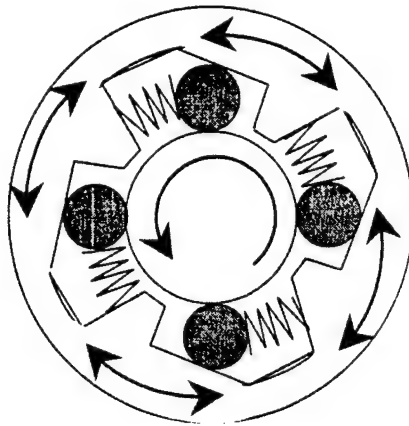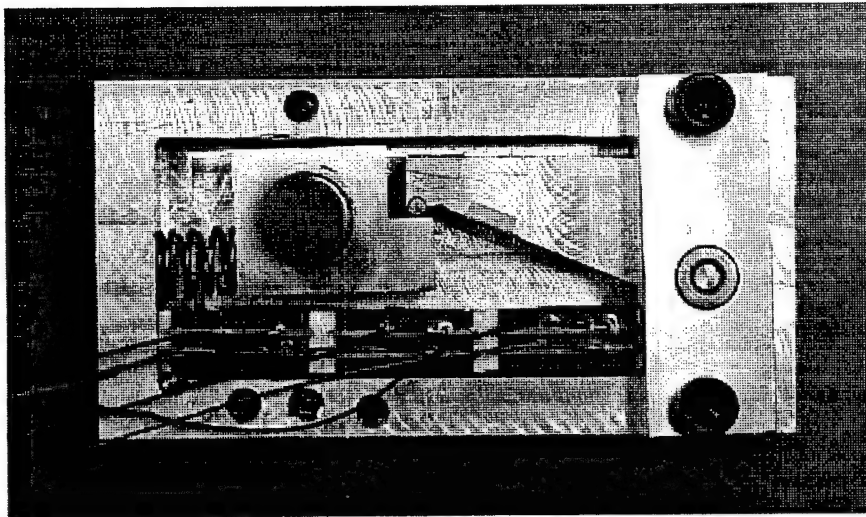
8

Figure 10. A Roller Clutch

Figure 11. A Rotary Roller-Wedgeworm

The device shown in Figure 11, driven between 0 and 265 V (corresponding to an electric field of about 10 kV/cm), and at 450 Hz, developed a free angular velocity of 300 RPM, and a maximum torque of about 0.32 N-m. Figure 12 shows the measured dependence of angular velocity on step rate. Other researchers have also recently begun to investigate similar approaches [Zhang, 1999].

Recent experiments on other similar devices have measured steady torques of about 0.5 N-m and speeds of about 400 RPM.
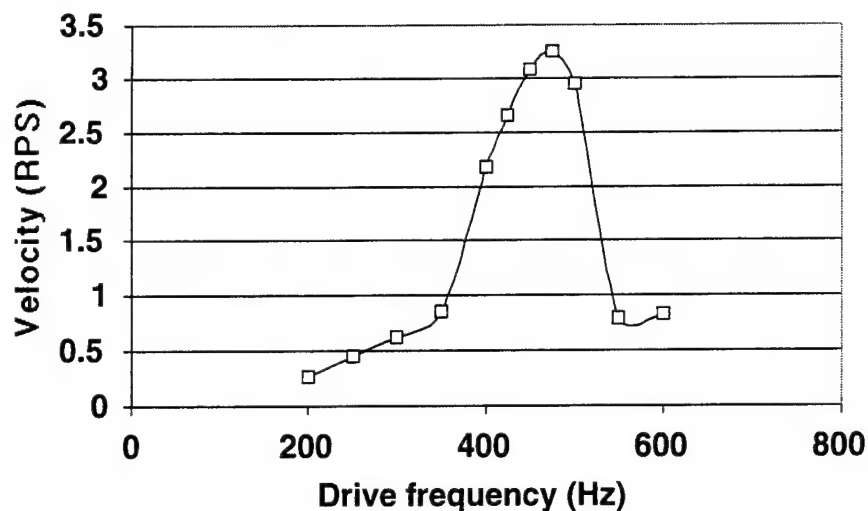
Figure 12. Angular Velocity vs. Step Rate for a Rotary Roller-Wedgeworm (Torque = 0.05 N-m)

Summary

In many realistic applications, the actuation energy density available from solid-state induced-strain materials is inadequate. In such cases, it is sensible to consider the use of such materials as the active drive elements in non-solid state, large-stroke devices such as motors. Furthermore, the development of such devices invites comparisons to competing approaches such as hydraulics and electric motors.

In order to compete with alternative technology, the output power density of piezoelectric motors must be increased. The key to high power density in such motors is rectification of small solid state, high-frequency oscillatory motion. Maximum power density is obtained by using a piezoelectric drive element that is as short as practical, as limited by the backlash, and running it at as high a frequency as possible.

The evolution of a number of piezoelectric stepping motors was described. These motors differ primarily in the approach used to perform the clamping function. Holding mechanisms initially relied entirely on Coulomb friction ("inchworm"), then on a combination of friction and mechanical advantage ("wedgeworm"), and currently on mechanical interference ("roller-wedgeworm").

A new rotary motor ("Rotary Roller-Wedgeworm") was described, and consists of an active stack, a mechanism to convert linear motion of the stack to rotary motion of a shaft, and two roller clutches. To obtain rotary motion, the stack is driven with an oscillatory signal. On the driving half of each cycle, the forward motion of the working end of the stack is converted to rotation of the shaft when the stack torque exceeds that of the load. On the recovery half of each cycle, a second roller clutch acts effectively as a mechanical diode, and prevents the load from backdriving the shaft. Experiments to date have demonstrated steady torques of about 0.5 N-m and speeds of about 400 RPM.

Acknowledgments

References

Chen, Quanfang, Da-Jeng Yao, Chang-Jin Kim, Greg P. Carman, "Development of mesoscale actuator device with micro interlocking mechanism," Journal of Intelligent Material Systems and Structures, v 9, n 6, 1997, pp. 449-457.

Crawley, Edward F., Javier de Luis, "Use of piezoelectric actuators as elements of intelligent structures," AIAA Journal, v 25, n 10, October, 1987.

Duong, Khanh, Ephrahim Garcia, "Design and performance of a rotary motor driven by piezoelectric stack actuators," Japanese Journal of Applied Physics, Part 1, v 35, n 12A, December 1996, pp. 6334-634

Frank, Jeremy, Gary H. Koopmann, Weiching Chen, George A. Lesieutre, "Design and performance of a high force piezoelectric inchworm motor," Proceedings of SPIE Smart Structures Conference, v 3668 n II, March 1-March 4, 1999, pp. 717-723.

Giurgiutiu, V., C.A. Rogers, Z. Chaudhry, "Design of displacement-amplified induced-strain actuators for maximum energy output," Journal of Mechanical Design, v 119 n 4, December, 1997, pp. 511-517

Giurgiutiu, Victor, Craig A. Rogers, "Comparison of solid state actuators based on power and energy criteria, Proceedings of SPIE Smart Structures Conference, v 2717, February 26-29, 1996, pp. 287-300.

Glenn, Timothy S., Nesbitt W. Hagood, "Development of a two-sided piezoelectric rotary ultrasonic motor for high torque," Proceedings of SPIE Smart Structures Conference, v 3041, March 3-6, 1997, pp. 326-338.

Lesieutre, G.A., "SAMPSON Core Technology: Electroceramic Actuation," at the DARPA Smart Structures Technology Interchange Meeting, NASA Langley Research Center, Hampton, VA, USA, June 6, 1998.

Mauck, Lisa, Christopher S. Lynch, "Piezoelectric hydraulic pump," Proceedings of SPIE Smart Structures Conference, v 3668, n II, March 1-4, 1999, pp. 844-852.

Teter, J.P., Musoke H. Sendaula, John Vranish, E.J. Crawford, "Magnetostrictive linear motor development," IEEE Transactions on Magnetics, v 34, n 4, pt 1, July, 1998, pp. 2081-2083.

Uchino, Kenji, "Piezoelectric ultrasonic motors: Overview," Smart Materials and Structures, v 7, n 3, June, 1998, pp. 273-285.

Zhang, Q.M., "A d15-based rotary motor," at the DARPA Smart Structures Technology Interchange Meeting, NASA Langley Research Center, Hampton, VA, USA, June 17, 1999.

ACTUATOR STUDIES

Piezoelectric Mini Motors

APPENDIX 61

High-efficiency piezoelectric motor combining continuous rotation with precise control over angular positioning

A. E. Glazounov,[a] S. Wang, and Q. M. Zhang
Materials Research Laboratory, The Pennsylvania State University, University Park, Pennsylvania 16802

C. Kim
Naval Research Laboratory, Washington, DC 20375

The letter describes a piezoelectric motor that combines the merits of piezoelectric materials, such as high power density generated at electromechanical resonance, and a precise control of displacement. The motor utilizes a direct coupling mechanism between the stator and rotor, where a clutch drives the rotor via locking it. The direct coupling makes it possible to transmit the whole power generated in the piezoelectric element to the rotor, and thus achieve the high efficiency of the motor. It also allows the combining of two regimes of operation: continuous rotation and a stepwise motion within a 360° interval with a high resolution of angular displacement. © 1999 American Institute of Physics. [S0003-6951(99)03232-5]

Among actuator materials, piezoelectrics such as lead zirconate titanate (PZT) are distinguished by the possibility of the precise control of produced displacement and by a high power density which enables operation at high driving frequencies.[1] The applications that make use of these features include for example, robotics,[1] vibration and noise cancellation, and translational stages for optical systems and scanning tunneling microscopes.[2,3] At the same time, the major demerit of PZT is that the piezoelectric strain is very small. Therefore, in order to convert a small strain into a large displacement, possible solutions include either a built-in amplification mechanism such as a "moonie"[4] or a tubular torsional actuator,[5] or an accumulation of the displacement over many periods of the alternating current (ac) driving voltage such as with "inchworm" actuators[6] or ultrasonic motors.[6]

Ultrasonic motors also take advantage of the high power density of PZT, and operate at the electromechanical resonance of the piezoelectric element, which is built into the stator. The displacement is accumulated by converting the high frequency mechanical vibrations excited at the resonance into the motion of the rotor by using the frictional contact between the stator and the rotor.[6] However, the frictional contact limits the performance of the motor: (i) the energy dissipation due to the friction reduces its efficiency, (ii) the torque that can be transmitted from the piezoelectric element is limited by the frictional force, and (iii) sliding of the rotor due to its inertia does not enable an instantaneous start and stop operation, and hence, it is difficult to achieve precise control over the displacement of the rotor.

The concept of the motor proposed in this work, it so employ the high power density of PZT, by driving the motor at resonance, and to accumulate the produced displacement by using a direct coupling mechanism between the stator and rotor, which drives the rotor via locking it. In this way, all the power generated in PZT at the resonance can be trans-

mitted to the rotor because now there is no energy loss in the frictional contract, and the friction force does not limit the torque. Also, the locking mechanism allows smooth motion either in a continuous or stepwise fashion within a 360° interval with precise control over angular positioning. Thus, in this motor one fully employs the merits of piezoelectric materials.

In the proposed motor, Fig. 1, piezoelectric ceramic tube, Fig. 1(a), generates high frequency torsional vibrations
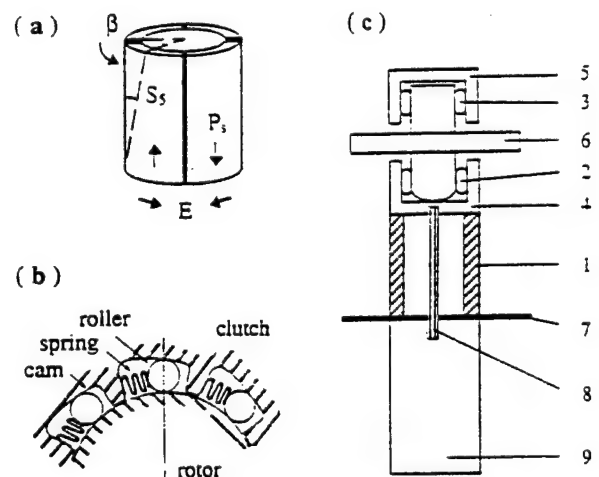

FIG. 1. (a) Piezoelectric ceramic segments are bonded together to form a tube using a conductive adhesive, which also acts as electrodes to apply the driving electric field. E. Since the direction of the polarization, P_s, alternates between the adjacent segments, they exhibit a coherent shear piezoelectric strain $S_5 = d_{15}E$, and that results in a torsional deformation of the tube on an angle β. (b) Roller clutch transmits the displacement to the rotor only if it moves in the counterclockwise direction, when the rollers are wedged between the tilted slope of the cam and the surface of the rotor. In the clockwise direction, the rollers disengage and do not transmit the displacement. (c) The proposed piezoelectric motor consists of piezoelectric tube shown in (a), "1", two clutches, shown in (b), "2" and "3", housing for clutches "4" and "5", metal shim, "7", and the rotor, "6". Bolt "8" tightens together piezoelectric tube and a metal cylinder "9", which is required in order to have zero angular displacement in the shim, "7", at resonance.

[a]Electronic mail: axg28@psu.edu

in the stator using the shear piezoelectric response, as was described in earlier works.[5,7] A one-way clutch, Fig. 1(b) and "2" in Fig. 1(c), is connected to the piezoelectric tube. "1," via housing, "4," so that it can move together with the tube, and is used to accumulate the angular displacement in one direction. When the tube with the clutch twists counterclockwise, Figs. 1(b) and 1(c), the clutch locks the rotor with the rollers [because the rollers are wedged between the tilted slope of the cam and the surface of the rotor, Fig. 1(b)], and transmits the displacement. On the contrary, if the tube twists clockwise, the clutch releases the rollers and they do not transmit the displacement to the rotor in this direction. Thus, the clutch provides an accumulation of angular displacement in one direction. An identical second clutch, "3" in Fig. 1(c), is mounted to the external support, and is used to prevent motion in the opposite direction [clockwise in Fig. 1(b)] when the external torque load is applied to the rotor.

To build the prototype, Fig. 1(c), the piezoelectric ceramic tube 1 was tightly clamped between two metal parts, 4 and "9," using "8." The dimensions of these components were evaluated using an equivalent circuit analysis of piezoelectric vibrations.[8] They must be such that at resonant frequency, the lengths of the part above a metal shim, "7," and below it are each equal to $\lambda/4$; where λ is the wavelength of standing shear wave excited by the piezoelectric tube. At this condition, the maximum angular displacement occurs at the free ends of the stator:

$$\beta = \frac{L}{R_{out}} \times (d_{15}E) \times Q_L. \qquad (1)$$

where d_{15} is the shear piezoelectric coefficient, E is the electric driving field, L is the length of the part above the shim. R_{out} is the outer radius of the tube and/or stator, and Q_L is the mechanical quality factor of the stator.[3] At the same time, $\beta = 0$ at the shim, and therefore, the shim can be used for the attachment of the stator to the external support. The piezoelectric tube was made of hard PZT ceramics (APC-841 from American Piezoceramics), and metal parts were made of hard aluminum in order to have a higher mechanical quality factor Q_L. The approximate dimensions of the stator were equal to: $2 \times L = 80$ mm (total length) and $R_{out} \approx 8$ mm. The resonant frequency, f_r, corresponding to these dimensions is approximately equal to 10 kHz. Both clutches, 2 and 3, are commercially available products from Torrington.

Figure 2 demonstrates proof of the concept of the proposed motor. When an ac voltage was applied to the piezoelectric tube, the rotor was moving with the revolution speed Ω, which increased toward saturation with increasing voltage (open circles). This behavior of Ω correlates with the voltage dependence of the amplitude of the torsional vibrations β (closed circles). The latter was measured at the free end of the stator by attaching a small mirror on top of the housing, 4, and by measuring the distance change between the mirror and the optical probe of a MTI-2000 fotonic sensor.[5]

Two more features should be noticed in Fig. 2. The first feature is that from Eq. (1), one would expect that β, and therefore, Ω, should increase linearly with the voltage (or electric field). The deviation from the linear function, seen in Fig. 2, is due to the strong frequency and field dependence of the piezoelectric response around the resonance,[9] which is
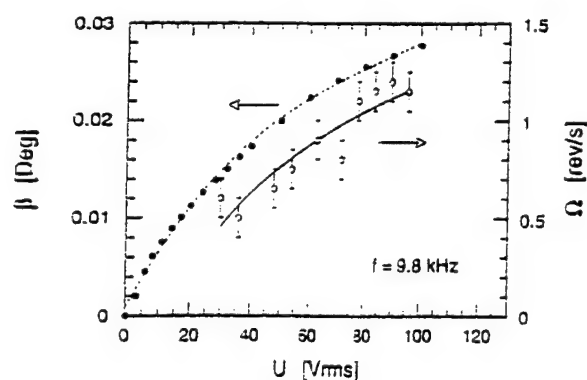

FIG. 2. Amplitude of torsional vibrations of the stator, β, and the revolution speed of the rotor, Ω, as a function of the ac driving voltage (the frequency is constant, 9.8 kHz).

illustrated in Fig. 3. When the amplitude of the driving voltage (electric field) is increased, the position of the resonance peak in $\beta(f)$ shifts toward lower frequencies, Fig. 3(a), due to the softening of the piezoelectric material under the high stress developed in it at the resonance.[3,9] As a result, this shift in the resonance peak will lead to the saturation in the field dependence of the displacement measured at a fixed frequency (for example, $f = 9.9$ kHz; as is clear from a comparison of the plots in Figs. 3(a) and 3(b). At the same time, the displacement at the peak, $f = f_r$, still follows a linear dependence predicted by Eq. (1), as shown with open circles in Fig. 3(b).

The second feature is that the rotation had some threshold and in the studied prototype the rotor did not move when the driving voltage was below 30 V rms; Fig. 2. This threshold is due to the backlash, or lost displacement, $\Delta\beta$, which is a common feature of clutches available on the market. One can evaluate $\Delta\beta$ from the data shown in Fig. 2. Without backlash, the amplitude of the torsional vibrations and the revolution speed should be related by: $\Omega \cdot 360° = 2 \times \beta \times f$, where f is the frequency of the ac voltage and the factor 2 appears because the clutch drives the rotor during half of a period of the ac voltage, when the displacement changes from $-\beta$ to $+\beta$. With the lost displacement $\Omega \times 360° \times f^{-1} = 2\beta - \Delta\beta$, and therefore, we obtain: $\Delta\beta \approx 0.01°$.

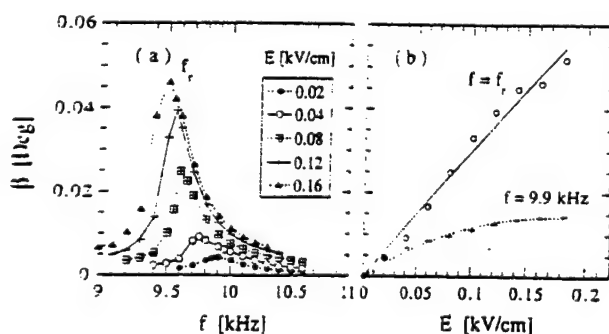Even though the backlash is fairly small, it sets some limits on the performance of the prototype motor. Still, it is

FIG. 3. Amplitude of torsional vibrations of the stator, β, around the resonance. (a) Frequency dependence of β measured at different levels of the ac driving field, E, showing the peaks at the resonant frequency, f_r. (b) Field dependence of β measured at a fixed frequency, 9.9 kHz (plus signs), and at the resonance, f_r (open circles).
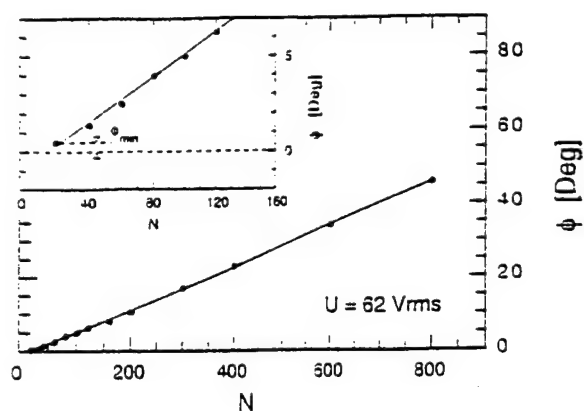
FIG. 4. The angular displacement of the rotor, ϕ, measured in the stepwise motion as a function of the number of the cycles, N, in the burst and the fit to the linear law. The magnified part of the plot is shown in the inset, in order to demonstrate that there exists a minimum value of N required to move the rotor, and the minimum achievable displacement, ϕ_{min}. The frequency of the ac voltage is 9.6 kHz.

surprising that the motor could operate even using commercially available roller clutches which in principle are not designed for operation with such small angular oscillations, of the order of 0.01° (Fig. 2). With improved clutch, the lost displacement can be completely eliminated, as it is done for example in watch mechanisms. This would allow better control over the motion, and would improve the torque transmitted to the rotor, which is also affected by the backlash.

Hence, the experiment summarized in Fig. 2 proves the proposed concept, that is, to use the clutch as a coupling mechanism to accumulate the angular displacement generated by the piezoelectric tube and produce unidirectional motion of the rotor. Moreover, because the clutch drives the rotor by locking it, this allows achieving not only a continuous rotation, but also a controlled stepwise motion of the rotor over a finite angle.

In order to produce the stepwise motion, the driving voltage can be applied in the form of the tone burst, using a given number, N, of ac cycles at a frequency f. The angular displacement, ϕ, of the rotor accumulated over N cycles can be written as: $\phi=[2\beta-\Delta\beta]\times N$, where β is the amplitude of the vibrations of the stator corresponding to the same frequency of the driving voltage, and we took into account the backlash, $\Delta\beta$. Figure 4 shows the example of the angular displacement as a function of N, measured using the ac voltage with frequency 9.6 kHz and amplitude 62 V rms. The fit of the linear relationship, $\phi \times N$, to the data yields the slope equal to 0.058 ± 0.002 [deg], which has a meaning of the displacement of the rotor per cycle of driving voltage. Using the obtained value of the slope, ϕ/N, and $\beta=0.04°$ measured at 9.6 kHz, we can calculate $\Delta\beta\approx0.02°$, which is in a reasonable agreement with the value $\Delta\beta\approx0.01°$ estimated from the data shown in Fig. 2.

The resolution limit for the stepwise motion can be determined by reducing the number of cycles, N, and measuring the smallest achievable displacement of the rotor, ϕ_{min}. At 62 V rms and 9.6 kHz we found that this prototype motor could be easily controlled down to $\phi_{min}=0.5°$, as shown in the inset to Fig. 4. By changing the driving voltage to 25 V rms, we could achieve even better control, $\phi_{min}=0.2°$, because of the increase in the number of cycles required to move the rotor ($N=50$ compared to $N=20$ in Fig. 4). Hence, this experiment demonstrated that even, with the available clutch, the motor can produce a stepwise motion with a precise control over angular positioning.

In previous works,[5,7] it was shown that at low frequencies the torque developed by the piezoelectric tube is described by

$$T = \frac{\pi(R_{out}^4 - R_{in}^4)}{2 s_{44}^E R_{out}} \times d_{15} E. \tag{2}$$

where R_{in} and R_{out} are inner and outer radii of the tube, respectively, and s_{44}^E is the shear elastic compliance of PZT. The analysis of the resonance vibrations using the equivalent circuit approach[3] predicts that the same formula should be also valid around the resonance, which makes it possible to evaluate the torque generated by the stator from the dimensions of the tube, and materials properties, s_{44}^E and d_{15}. One can expect that after elimination of the backlash, the clutch will transmit the torque to the rotor completely because the motor utilizes the direct coupling mechanism, via locking the rotor. Thus, the performance of the motor will be fully determined by the piezoelectric element, since now the frictional force[6] does not limit the torque.

In conclusion, a design of a piezoelectric motor was proposed, which takes advantage of the torsional motion generated at the resonance in the stator, and of the direct coupling between the rotor and the stator to accumulate the displacement and produce a large torque. It was shown that the direct coupling allows for smooth motion either in the continuous or in the stepwise fashion within a 360° interval with a precise control over angular positioning.

[1] K. Uchino. Piezoelectric Devices and Ultrasonic Motors (Kluwer Academic. Boston. MA. 1997).
[2] Ph. Niedermann, R. Emch, and P. Descouts. Rev. Sci. Instrum. 59, 368 (1988).
[3] C. J. Chen. Appl. Phys. Lett. 60, 132 (1992).
[4] Y. Sugawara, S. Yoshikawa, Q. Xu, R. E. Newnham, and K. Uchino. J. Am. Ceram. Soc. 75, 996 (1992).
[5] A. E. Glazounov, Q. M. Zhang, and C. Kim. Appl. Phys. Lett. 72, 2526 (1998).
[6] S. Ueha and Y. Tomikawa. Ultrasonic Motors: Theory and Applications (Oxford University Press. Oxford, 1993).
[7] A. E. Glazounov, Q. M. Zhang, and C. Kim. Proc. SPIE 3324, 82 (1998).
[8] D. Berlincourt, D. Curran, and H. Jaffe, in Physical Acoustics, edited by W. Mason (Academic. New York. 1969). Vol. 1, pt. A, pp. 169–269.
[9] H. Beige and G. Schmidt. Ferroelectrics 41, 39 (1982).

APPENDIX 62

Compact Piezoelectric Ultrasonic Motors

KENJI UCHINO and BURHANETTIN KOC

*International Center for Actuators and Transducers, Materials Research
Laboratory, The Pennsylvania State University, University Park, PA 16802, USA*

This paper reviews recent developments of compact ultrasonic motors using piezoelectric resonant vibrations. Following the historical background, ultrasonic motors using the standing and traveling waves are introduced. Driving principles and motor characteristics are explained in comparison with the conventional electromagnetic motors.

Keywords: ultrasonic motor; piezoelectric actuator; standing wave motor

INTRODUCTION

In office equipment such as printers and floppy disk drives, market research indicates that tiny motors smaller than 1 cm^3 would be in large demand over the next ten years. However, using the conventional electromagnetic motor structure, it is rather difficult to produce a motor with sufficient energy efficiency. Piezoelectric ultrasonic motors, whose efficiency is insensitive to size, are superior in the mm-size motor area.

In general, piezoelectric and electrostrictive actuators are classified into two categories, based on the type of driving voltage applied to the device and the nature of the strain induced by the voltage: (1) rigid displacement devices for which the strain is induced unidirectionally along an applied dc field (servo displacement transducers and pulse drive motors), and (2) resonating displacement devices for which the alternating strain is excited by an ac field at the mechanical resonance frequency (ultrasonic motors). The AC resonant displacement is not directly proportional to the applied voltage, but is, instead, dependent on adjustment of the drive frequency. Although the positioning

accuracy is not as high as that of the rigid displacement devices, very high speed motion due to the high frequency is an attractive feature of the ultrasonic motors.

The materials requirements for these classes of devices are somewhat different, and certain compounds will be better suited for particular applications. The servo-displacement transducer suffers most from strain hysteresis and, therefore, a PMN electrostrictor is preferred for this application. The pulse-drive motor requires a low permittivity material aiming at quick response with a limited power supply rather than a small hysteresis, so that soft PZT piezoelectrics are preferred to the high-permittivity PMN for this application. On the contrary, the ultrasonic motor requires a very hard piezoelectric with a high mechanical quality factor Q_m, in order to minimize heat generation and maximize displacement. Note that the resonance displacement is equal to $\alpha \cdot dEL$, where d is a piezoelectric constant, E, applied electric field, L, sample length and α is an amplification factor proportional to the mechanical Q.

This paper deals with ultrasonic motors using resonant vibrations, putting a particular focus on miniaturized motors. Following the historical background, various ultrasonic motors are introduced. Driving principles and motor characteristics are explained in comparison with the conventional electromagnetic motors.

CLASSIFICATION OF ULTRASONIC MOTORS

Historical Background

Electromagnetic motors were invented more than a hundred years ago. While these motors still dominate the industry, a drastic improvement cannot be expected except through new discoveries in magnetic or superconducting materials. Regarding conventional electromagnetic motors, tiny motors smaller than 1cm long are rather difficult to produce with sufficient energy efficiency. Therefore, a new class of motors using high power ultrasonic energy -- ultrasonic motor, is gaining wide spread attention. Ultrasonic motors made with piezoceramics whose efficiency is insensitive to size are superior in the mini-motor area. Figure 1 shows the basic construction of an ultrasonic motor,

which consists of a high-frequency power supply, a vibrator and a slider. Further, the vibrator is composed of a piezoelectric driving component and an elastic vibratory part, and the slider is composed of an elastic moving part and a friction coat.
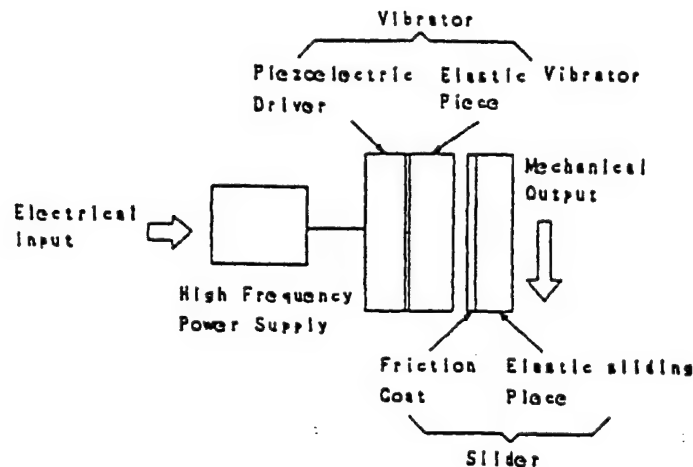

Fig. 1   Fundamental construction of ultrasonic motors.

Though there had been some earlier attempts, the practical ultrasonic motor was proposed firstly by H. V. Barth of IBM in 1973.[1]   A rotor was pressed against two horns placed at different locations. By exciting one of the horns, the rotor was driven in one direction, and by exciting the other horn, the rotation direction was reversed. Various mechanisms based on virtually the same principle were proposed by V. V. Lavrinenko[2] and P. E. Vasiliev[3] in the former USSR. Because of difficulty in maintaining a constant vibration amplitude with temperature rise, wear and tear, the motors were not of much practical use at that time.

In 1980's, with increasing chip pattern density, the semiconductor industry began to request much more precise and sophisticated positioners which do not generate magnetic field noise. This urgent request has accelerated the developments in ultrasonic motors. Another advantage of ultrasonic motors over the conventional electromagnetic motors with expensive copper coils, is the improved availability of piezoelectric ceramics at reasonable cost. Japanese manufacturers are producing piezoelectric buzzers around 30 - 40 cent price range at the moment.

Let us summarize the merits and demerits of the ultrasonic motors:

___

Merits

1. Low speed and high torque   -- Direct drive
2. Quick response, wide velocity range, hard brake and no backlash
                                    -- Excellent controllability
                                    -- Fine position resolution
3. High power / weight ratio and high efficiency
4. Quiet drive
5. Compact size and light weight
6. Simple structure and easy production process
7. Negligible effect from external magnetic or radioactive fields, and also no generation of these fields

Demerits

8. Necessity for a high frequency power supply
9. Less durability due to frictional drive
10. Drooping torque vs. speed characteristics

___

Classification and Principles of Ultrasonic Motors

From a customer's point of view, there are rotary and linear type motors. If we categorize them from the vibrator shape, there are rod type, π-shaped, ring (square) and cylinder types. Two categories are being investigated for ultrasonic motors from a vibration characteristic viewpoint: a standing-wave type and a propagating-wave type. The standing wave is expressed by

$$u_S(x,t) = A \cos kx \cdot \cos \omega t, \tag{1}$$

while the propagating wave is expressed as

$$u_p(x,t) = A \cos (kx - \omega t). \tag{2}$$

Using a trigonometric relation, Eq. (2) can be transformed as

$$u_p(x,t) = A \cos kx \cdot \cos \omega t + A \cos (kx - \pi/2) \cdot \cos (\omega t - \pi/2). \tag{3}$$

This leads to an important result, i. e. a propagating wave can be generated by superimposing two standing waves whose phases differ by 90 degree to each other both in time and in space. This principle is necessary to generate a propagating wave on a limited volume/size substance, because only standing waves can be excited stably in a finite size.

The standing-wave type is sometimes referred to as a vibratory-coupler type or a "woodpecker" type, where a vibratory piece is connected to a piezoelectric driver and the tip portion generates flat-elliptical movement. Figure 2 shows a simple model proposed by T. Sashida.[4] A vibratory piece is connected to a piezoelectric driver and the tip portion generates flat-elliptical movement. Attached to a rotor or a slider, the vibratory piece provides intermittent rotational torque or thrust. The standing-wave type has, in general, high efficiency, but lack of control in both clockwise and counterclockwise directions is a problem.

By comparison, the propagating-wave type (a surface-wave or "surfing" type) combines two standing waves with a 90 degree phase difference both in time and in space. The principle is shown in Fig. 3. A surface particle of the elastic body draws an elliptical locus due to the coupling of longitudinal and transverse waves. This type requires, in general, two vibration sources to generate one propagating wave, leading to low efficiency (not more than 50 %), but it is controllable in both the rotational directions.
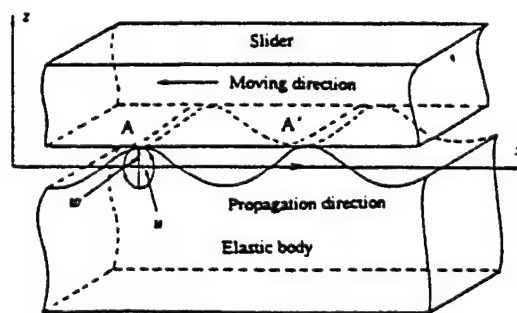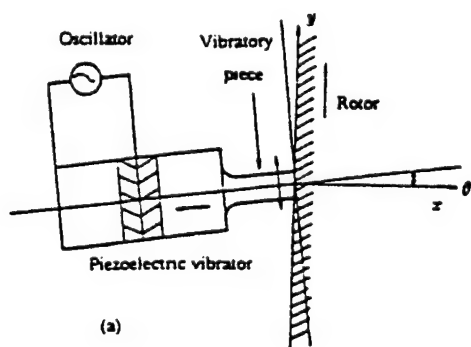

Fig. 2 Vibratory coupler type motor.   Fig. 3 Principle of the propagating wave type motor.

CONVENTIONAL MOTOR DESIGNS

Sashida Motor

Figure 4 shows the famous Sashida motor.[5] By means of the traveling elastic wave induced by a thin piezoelectric ring, a ring-type slider in contact with the "rippled" surface of the elastic body bonded onto the piezoelectric is driven in both directions by exchanging the sine and cosine voltage inputs. Another advantage is its thin design, which makes it suitable for installation in cameras as an automatic focusing device. Eighty percent of the exchange lenses in Canon's "EOS" camera series have already been replaced by the ultrasonic motor mechanism. Most of the studies on ultrasonic motors done in the US and Japan have been modifications of Sashida's type.

The PZT piezoelectric ring is divided into 16 positively and negatively poled regions and two asymmetric electrode gap regions so as to generate a 9th mode propagating wave at 44 kHz. A proto-type was composed of a brass ring of 60 mm in outer diameter, 45 mm in inner diameter and 2.5 mm in thickness, bonded onto a PZT ceramic ring of 0.5 mm in thickness with divided electrodes on the back-side. The rotor was made of polymer coated with hard rubber or polyurethane. Figure 5 shows Sashida's motor characteristics.

Canon utilized the "surfing" motor for a camera automatic focusing mechanism, installing the ring motor compactly in the lens frame. It is noteworthy that the stator elastic ring has many teeth, which can magnify the transverse elliptical displacement and improve the speed. The lens position can be shifted back and forth through a screw mechanism. The advantages of this motor over the conventional electromagnetic motor are:

1. Silent drive due to the ultrasonic frequency drive and no gear mechanism (i. e. more suitable to video cameras with microphones).
2. Thin motor design and no speed reduction mechanism such as gears, leading to space saving.
3. Energy saving.

A general problem encountered in these traveling wave type motors is the support of the stator. In the case of a standing wave motor, the nodal points or lines are generally supported; this causes minimum effects on the resonance vibration. To the contrary, a traveling wave does not have such steady nodal

points or lines. Thus, special considerations are necessary. In Fig. 4, the stator is basically fixed very gently along the axial direction through felt so as not to suppress the bending vibration. It is important to note that the stop pins which latch onto the stator teeth only provide high rigidity against the rotation.
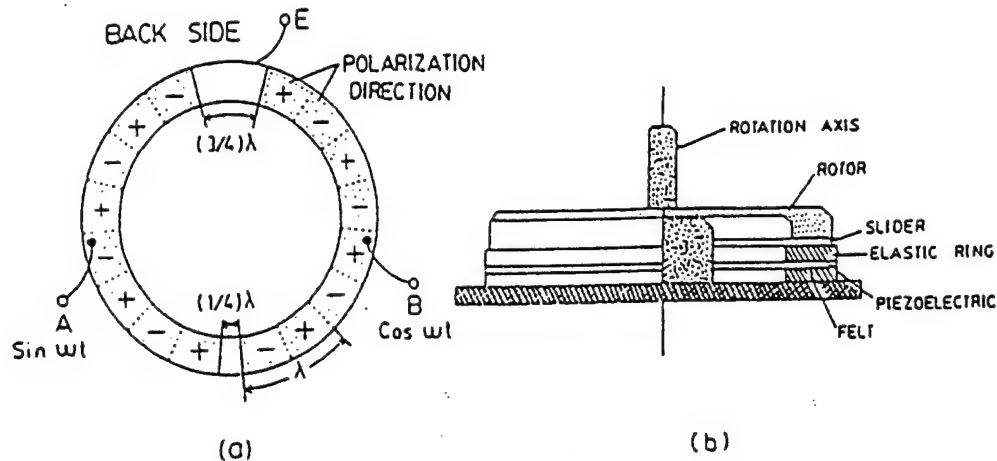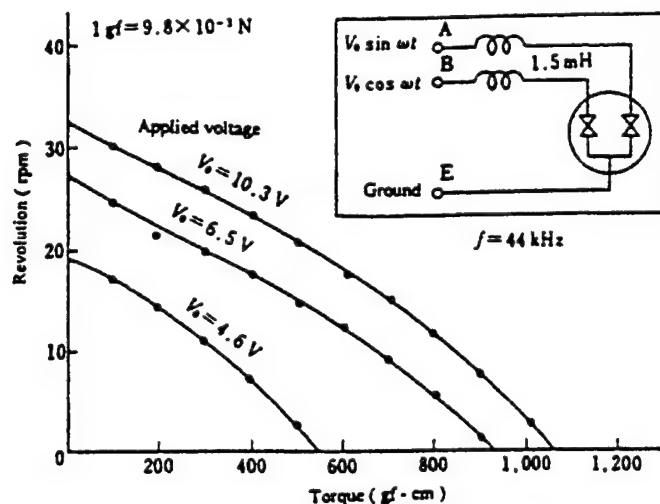
Fig. 4   Stator structure of Sashida's motor.

Fig. 5   Motor characteristics of Sashida's motor.

Inchworm Devices

Although the motion principle is different, inchworm devices move fast in apparent similarity to ultrasonic motors. The inchworm is driven by a rectangular wave below the resonance frequency, and moves intermittently and discretely.
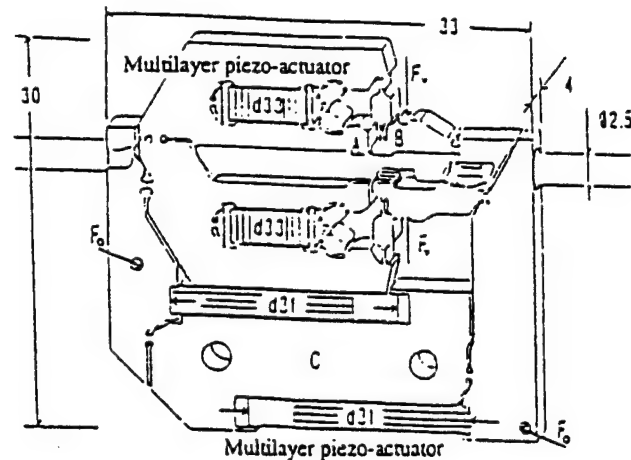
Fig. 6   Philips' inchworm.

Sophisticated linear walking machines have been developed by two German companies. Philips fabricated a linear drive inchworm using two d_{33} (longitudinal mode) and two d_{31} (transverse mode) multilayer actuators (Fig. 6).[6] Very precise positioning of less than 1 nm was reported. The problems with this type of device are: (1) audible noise, and (2) heat generation, when driven at high frequency. Physik Instrumente manufactured a two-leg inchworm.[7] A pair of inchworm units consisting of two multilayer actuators, are coupled with 90° phase difference in time so as to produce a smooth motion instead of a discrete step motion.

COMPACT MOTOR DESIGNS

Traveling Wave Types

Using basically the same principle as Sashida's, Seiko Instruments miniaturized the ultrasonic motor to as tiny as 10 mm in diameter.[8] Figure 7 shows the construcion of this small motor with 10 mm diameter and 4.5 mm thickness. A driving voltage of 3 V and a current 60 mA provides 6000 rev/min (no-load) with torque of 0.1 mN·m. Seiko installed this tiny motor into a wrist watch as a silent alarm. Rotating an imbalanced mass provides enough hand shake to a human without generating audible noise. AlliedSignal developed ultrasonic

motors similar to Shinsei's, which would be utilized as mechanical switches for launching missiles.[9]

A significant problem in miniaturizing this sort of traveling wave motor can be found in the ceramic manufacturing process; without providing a sufficient buffer gap between the adjacent electrodes, the electrical poling process (upward and downward) easily initiates the crack on the electrode gap due to the residual stress concentration. This may restrict the further miniaturization of the traveling wave type motros. To the contrary, standing wave type motors, the structure of which is less complicated, are more suitable for miniaturization as we discuss in the following. They require only one uniformly poled piezo-element, less electric lead wires and one power supply.
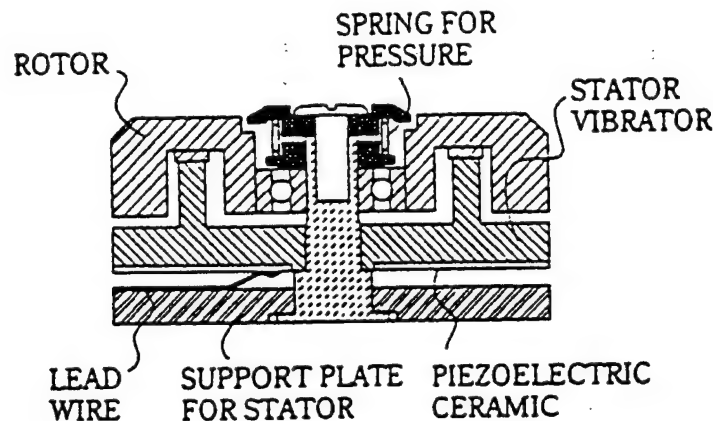

Fig. 7 Construction of Seiko's motor.

Standing Wave Types

Linear motors

Uchino et al. invented a π-shaped linear motor.[10] This linear motor is equipped with a multilayer piezoelectric actuator and fork-shaped metallic legs as shown in Fig. 8. Since there is a slight difference in the mechanical resonance frequency between the two legs, the phase difference between the bending vibrations of both legs can be controlled by changing the drive frequency. The walking slider moves in a way similar to a horse using its fore and hind legs when trotting. A test motor 20 x 20 x 5 mm^3 in dimension exhibited a maximum speed of 30 cm/s and a maximum thrust of 0.9 kgf with a maximum

efficiency of 20%, when driven at 98kHz at 6V (actual power = 0.7 W). This motor has been employed in a precision X-Y stage.
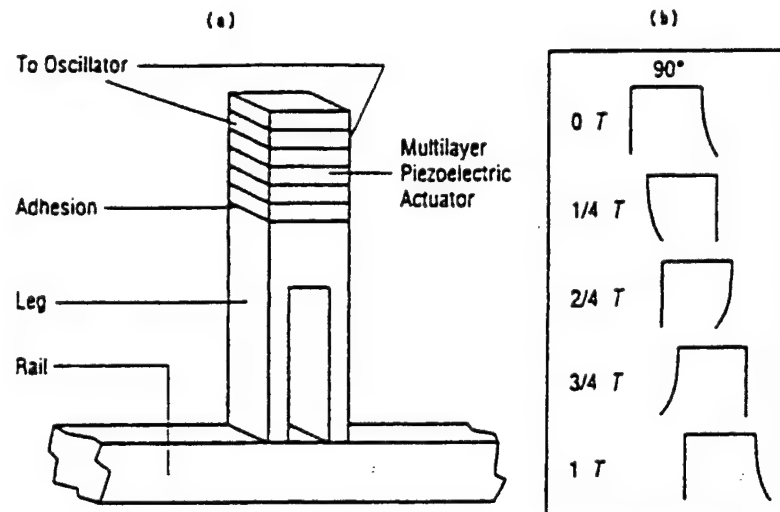

Fig. 8   π-shaped linear ultrasonic motor. (a) construction and (b) walking principle. Note the 90 degree phase difference like human walk.
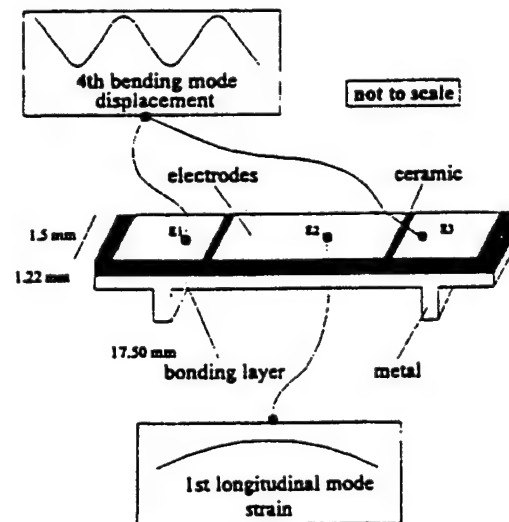

Fig. 9   Miniature ultrasonic linear motor.

We further miniaturized this "Shepherd" shape by 1/10 into a "Dachshund" shape by reducing the leg length (Fig. 9).[11] According to this miniaturization, we utilized a unimorph type drive mechanism in conjunction with a coupling mode between 1st longitudinal and 4th bending modes. Under

100 V_{p-p} applied (0.6 W), this linear motor exhibited the maximum speed of 160 mm/sec and the thrust of 0.25 - 1.00 N.

One ceramic multilayer component actuator was proposed by Mitsui Chemical.[12] Figure 10 shows the electrode pattern. Only by the external connection, a combined vibration of the longitudinal L_1 and bending B_2 modes could be excited.
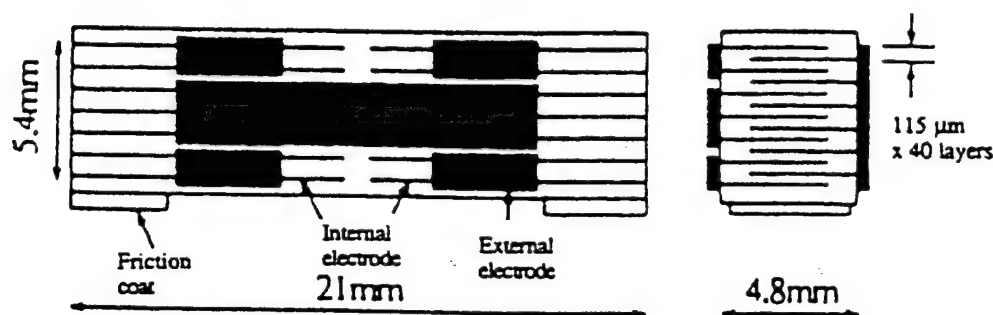

Fig. 10   Multilayer ceramic simple linear motor (Mitsui Chemical).

Rotary motors

Hitachi Maxel significantly improved the torque and efficiency by using a torsional coupler, and by the increasing pressing force with a bolt.[13] The torsional coupler looks like an old fashioned TV channel knob, consisting of two legs which transform longitudinal vibration generated by the Langevin vibrator to a bending mode of the knob disk, and a vibratory extruder. Notice that this extruder is aligned with a certain cant angle to the legs, which transforms the bending to a torsion vibration. This transverse moment coupled with the bending up-down motion leads to an elliptical rotation on the tip portion. A motor with 30mm x 60mm in size and 20 - 30° in cant angle between a leg and a vibratory piece provided the torque as high as 1.3 N·m and the efficiency of 80%. However, this type provides only unidirectional rotation.

The Penn State University has developed a compact ultrasonic rotory motor as tiny as 3 mm in diameter. As shown in Fig. 11, the stator consists basically of a piezoelectric ring and two concave/convex metal endcaps with "windmill" shaped slots bonded together, so as to generate a coupled vibration

of up-down and torsional type.[14)   Since the component number and the fabrication process were minimized, the fabrication price would be decreased remarkably, and it would be adaptive to the disposable usage. When driven at 160 kHz, the maximum revolution 2000rpm and the maximum torque 0.8mN·m were obtained for a 5 mmϕ motor. Notice that even the drive of the motor is intermittent, the output rotation becomes very smooth because of the inertia of the rotor. Figure 12 shows motor characteristics plotted as a function of motor size for modified "windmill" motors.[15)
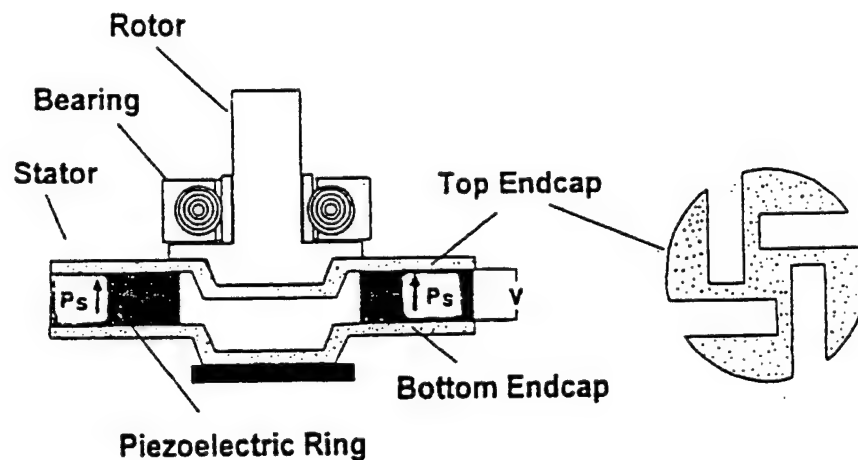
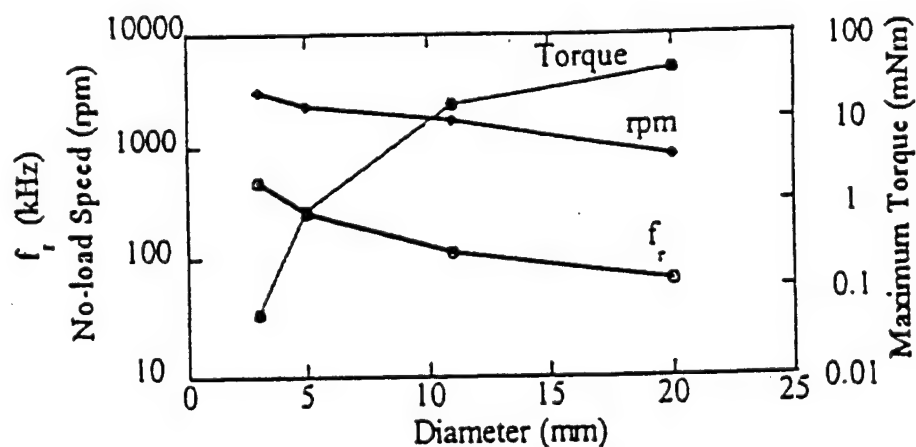Fig. 11   "Windmill" motor with a disk-shaped torsional coupler.

Fig. 12   Radial mode resonance frequency, no-load speed and starting torque vs. diameter of the stator. Speed and torque were measured at 15.7 V.

INTEGRATED MOTOR DESIGNS

We will introduce an ultrasonic motor fabricated on a Si substrate, jointly developed by MIT and Penn State.[16] After coating a PZT thin film on a Si membrane (2.2mm x 2.2mm), an 8-pole stator (1.2mm and 2.0mm inner and outer diameters) was patterned on the surface electrode. The 8 segmented electrode pads were driven in a four phase sequence repeated twice. A small contact glass lens was used as a rotor. This simple structure provided already 10^3 time higher torque than the conventional electrostactic MEMS motors.

Another intriguing surface acoustic wave motor has been proposed by Kurosawa and Higuchi.[17] Rayleigh waves were excited in two crossed directions on a 127.8°-rotation Y-LiNbO$_3$ plate with two pairs of interdigital electrode patterns. A slider was composed of three balls as legs. The driving vibration amplitude and the wave velocity of the Rayleigh waves were adjusted to 6.1 nm and 22 cm/sec for both x and y directions. It is important to note that even though the up-down vibrational amplitude is much smaller (< 1/10) than the surface roughness of the LiNbO$_3$, the slider was transferred smoothly. The mechanism has not been clarified yet, it might be due to the locally enhanced friction force through a ball-point contact.

SUMMARY

Ultrasonic motors are characterized by "low speed and high torque," which are contrasted with "high speed and low torque" of the conventional electromagnetic motors. Thus, the ultrasonic motors do not require gear mechanisms, leading to very quiet operation and space saving. Negligible effects from external magnetic or radioactive fields, and no generation of these fields are suitable for the application to electron beam lithography etc. relevant to the semiconductor technology. Moreover, high power / weight ratio, high efficiency, compact size and light weight are very promising for the future micro actuators adopted to catheter or tele-surgery.

For the further applications of the ultrasonic motors, systematic investigations on the following issues will be required:

(1) development of low loss & high vibration velocity piezo-ceramics,
(2) piezo-actuator component designs with high resistance to fracture and good heat dissipation,
(3) ultrasonic motor designs;
    a. motor types (standing-wave type, traveling-wave type, hybrid type, integrated type),
    b. simple displacement magnification mechanisms of vibratory piece (horn, hinge-lever),
    c. frictional contact part,
(4) inexpensive and efficient high frequency/high power supplies.

Acknowledgement

References

[1] H.V. Barth: IBM Technical Disclosure Bull. **16**, 2263 (1973).

[2] V.V. Lavrinenko, S.S. Vishnevski and I.K. Kartashev: Izvestiya Vysshikh Uchebnykh Zavedenii, Radioelektronica **13**, 57 (1976).

[3] P.E. Vasiliev et al.: UK Patent Application GB 2020857 A (1979).

[4] T. Sashida: Oyo Butsuri **51**, 713 (1982).

[5] T. Sashida: Mech. Automation of Jpn., **15** (2), 31 (1983).

[6] M.P. Coster: Proc.4th Int'l Conf.on New Actuators, 2.6, p.144, Germany (1994).

[7] R. Gloess: Proc. 4th Int'l Conf. on New Actuators, P26, p.190, Germany (1994).

[8] M. Kasuga, T. Satoh, N. Tsukada, T. Yamazaki, F. Ogawa, M. Suzuki, I. Horikoshi and T. Itoh: J. Soc. Precision Eng., **57**, 63 (1991).

[9] J. Cummings and D. Stutts: Amer. Ceram. Soc. Trans. "Design for Manufacturability of Ceramic Components", p.147 (1994).

[10] K. Uchino, K. Kato and M. Tohda: Ferroelectrics **87**, 331 (1988).

[11] T. Bein, E.J. Breitbach and K. Uchino: Smart Mater. Struct. **6**, 619 (1997).

[12] H. Saigo: 15th Symp. Ultrasonic Electronics (USE 94), No. PB-46, p.253 (Nov. 1994).

[13] A. Kumada: Jpn. J. Appl. Phys., 24, Suppl. 24–2, 739 (1985).

[14] B. Koc, A. Dogan, Y. Xu, R.E. Newnham and K. Uchino: Jpn. J. Appl. Phys. **37**, 5659 (1998).

[15] B. Koc, Y. Xu and K. Uchino: Proc. IEEE Int'l Ultrasonic Symp., Sendai, Japan (1998) [in press].

[16] A.M. Flyn, L.S. Tavrow, S.F. Bart, R.A. Brooks, D.J. Ehrlich, K.R. Udayakumar and L. E. Cross: J. Microelectro-mechanical Systems, **1**, 44 (1992).

[17] M. Takahashi, M. Kurosawa and T. Higuchi: Proc. 6th Symp. Electro-Magnetic Dynamics '94, No. 940–26 II, D718, p.349 (July, 1994).

For further reading:

[18] K. Uchino: "Piezoelectric ultrasonic motors: overview" Smart Mater. Struct. **7**, 273 (1998).

[19] K. Uchino: *"Piezoelectric Actuators and Ultrasonic Motors,"* Kluwer Academic Publishers. MA (1996).

APPENDIX 63

Composite Ultrasonic Motors using a Piezoelectric Disc and an Elastic Body of "Windmill" Type

JIN-SOO KIM[a], MAN-JU PARK[a] and KENJI UCHINO[b]

[a]*Department of Technology Education, Korea National University of Education, Chungbuk, 363–791, KOREA and* [b]*International Center for Actuators and Transducers, Materials Research Laboratory, The Pennsylvania State University, University Park, PA 16802, USA*

This paper deals with a new piezoelectric ultrasonic motor operated by single-phase AC. The ultrasonic motor of windmill type using a piezoelectric ceramic and a metal elastic body was fabricated. To prepare the piezoelectric ceramics vibrator, 0.05PMN-0.95PZT composition was mixed with $0.7wt\%$ MnO_2. Dielectric loss, the electromechanical coupling factor of radial mode and mechanical quality factor were 0.2%, 62.8% and 820, respectively. The slotted metal elastic bodies made from brass sheet were machined at various thickness of 0.15, 0.20, 0.25, 0.30mm, and slots of the elastic body were 2, 3, 4, 6, respectively. No-load revolution speed increases with increasing applied voltage, and it increases with decreasing the thickness of the elastic body. The revolution speed of the ultrasonic motor is 510rpm under an applied voltage of 100 V_{max}.

Keywords: Ultrasonic motor; piezoelectric ceramics; windmill type; single-phase AC; vibration velocity; revolution speed

INTRODUCTION

It is generally known that the first practical ultrasonic motor was invented by T. Sashida in 1982, and then further study and development of the ultrasonic motor were performed[1]. Most ultrasonic motors[2,3] are operated by two-phase AC differing by 90°.

but in this paper only single-phase AC is needed to operate the ultrasonic motor of windmill type. We have studied the ultrasonic motor considering the use of a combination of radial and torsional vibration modes[4,5]. The aims of the study are to develop a new type of ultrasonic motor of windmill type operated by single-phase AC, and to study the revolution speed characteristics of the ultrasonic motor. But the torque characteristics and three-dimensional vibration mode of real-time animation will be presented next time.

EXPERIMENTAL

Composition of the piezoelectric ceramics is $Pb[(Mg_{1/3}Nb_{2/3})_{0.05}Zr_{0.475}Ti_{0.475}]O_3 + 0.7wt\%$ MnO_2 and the elastic body is 70Cu-30Zn brass. The powder was calcined at 850℃ for 2hrs, followed by sintering at 1200℃ for 2hrs. The samples were polished to 0.99mm thickness, and silver paste was attached to both sides at 700℃. Poling conditions were DC 1.5 kV/mm, 10 minute and 115℃ in the silicone oil bath. Piezoelectric and dielectric properties were measured using an impedance gain-phase analyzer after 48 hrs. For making the ultrasonic motor, the sample dimensions were 11.25mm in diameter and 0.99mm in thickness.
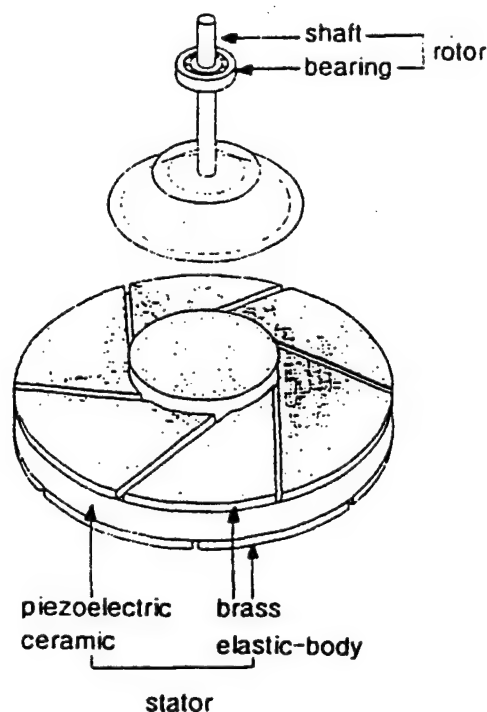

FIGURE 1. Structure of the ultrasonic motor of windmill type.

The structure of the ultrasonic motor is shown in Fig.1, where the stator made by piezoelectric ceramics and slotted elastic body vibrates the radial resonant mode. The radial vibration mode driven by

single-phase sinusoidal AC is transformed into the torsional mode. To make a stator, a piezoelectric ceramic vibrator was bonded with two pieces of metal elastic body using conductive epoxy, as shown in Fig.1. The elastic bodies with 0.15, 0.20, 0.25, 0.30mm in thickness and with 2,3,4,6 in slot of windmill type were fabricated using a saw machine, respectively. The contact surface of the rotor was also made of brass. The characteristics of the ultrasonic motor were measured using the system shown in Fig.2. To operate the ultrasonic motor, we used a high speed .power amplifier(NF4015, Japan) and function waveform generator(HP33120A, USA). The resonance frequency and vibration velocity of the stator were measured with vibrometer(Polytec OFV3000, Germany) inclusive sensor head(Polytec OFV302, Germany) and digital storage oscilloscope(HC5802, Korea). The revolution speed of the ultrasonic motor was measured with analog tachometer(Ametek C-809, USA).

FIGURE 2. Block diagram for measuring system of vibration velocity and revolution speed.

RESULTS AND DISCUSSION

Table 1 shows the optimal specifications of the ultrasonic motor of windmill type which has 6 slots and 0.15mm in thickness of elastic body. The revolution speed characteristics of the ultrasonic motor are basically dependent on the driving voltage and frequency. Here. the resonance frequency of the stator measured by vibrometer was observed at 73.6 kHz.

TABLE 1. Specifications of fabricated ultrasonic motor
of windmill type.

	Unit	Constant
Driving frequency	kHz	73.6
Driving voltage	V_{max}	100
Rated speed	rpm	510
Stator weight	gm	1.33
Rotor weight	gm	0.18
Resistance of stator	Ω	2.53

Fig.3 shows the relation between vibration velocity of the elastic body
and the applied voltage at various thickness of the elastic body with 6
slots. From this result, it was found that the vibration velocity of the
elastic body increases with increasing applied voltage, and it increases
with decreasing the thickness of the elastic body. The reason for this
behavior is that the flexibility of the elastic body increases as
thickness decreases. The stator of the ultrasonic motor with 0.15mm in
thickness of the elastic body exhibits a vibration velocity of 2.0 m/s
under an applied voltage of $100V_{max}$.
Fig.4 shows the effect of applied voltage on no-load revolution speed

FIGURE 3. Effect of applied voltage on vibration velocity of
elastic body at various thickness of elastic body with
6 slots

of the ultrasonic motor at various thickness of elastic body with 6 slots. In this experiment, the elastic body of brass and the rotor of brass were used. Single-phase AC voltage was applied to the ultrasonic motor using an high speed power amplifier whose voltage can be varied in the range of $30V_{max}$ to $100V_{max}$.
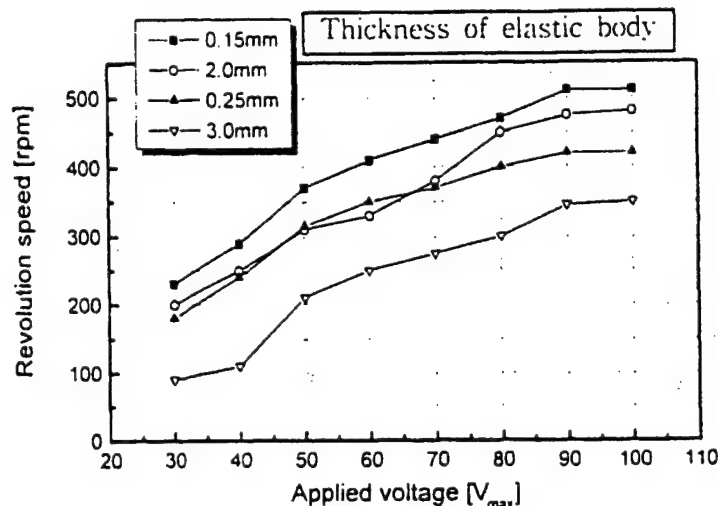

FIGURE 4. Effect of applied voltage on revolution speed of the ultrasonic motor at various thickness of elastic body with 6 slots.
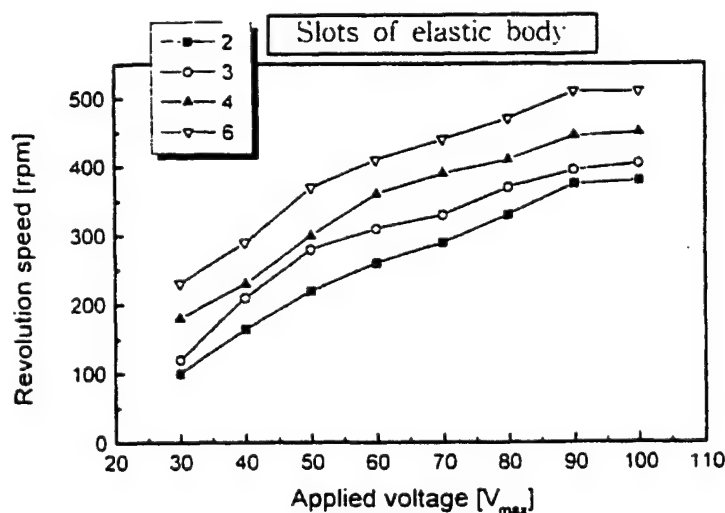

FIGURE 5. Effect of applied voltage on revolution speed of the ultrasonic motor at various slots of elastic body for 0.15mm in thickness.

The ultrasonic motor was not operated below an applied voltage of $30V_{max}$. No-load revolution speed increases with increasing applied voltage, and it increases with decreasing the thickness of elastic body. The revolution speed of the ultrasonic motor is 510rpm under an applied voltage of $100V_{max}$. Above $90V_{max}$, the revolution speed of the ultrasonic motor was almost constant.

Fig.5 indicates the effect of applied voltage on no-load revolution speed of the ultrasonic motor at various slots of elastic body for 0.15mm in thickness. When the applied voltage is 100 V_{max}, the maximum revolution speed of the ultrasonic motor is 510rpm. The revolution speed increases with increasing applied voltage, and it increases with increasing the slots of the elastic body, which is due to the generation of torsional mode at the elastic body.

CONCLUSIONS

The ultrasonic motor of windmill type operated by single-phase AC could simply be fabricated using a piezoelectric ceramic vibrator and two metal elastic body. When the applied voltage to the ultrasonic motor is $100V_{max}$ at a resonance frequency of 73.6kHz, the maximum revolution speed of the ultrasonic motor is 510rpm. In order to improve the reproducibility in terms of housing technique, torque characteristics, efficiency and 3-dimensional vibration mode of real-time of the elastic body using scanning vibrometer and FEA method are now under investigation.

References

[1] T. Sashida. *Applied Physics,* **51,** 713 (1982)
[2] Y. Tomikawa, T. Ogasawara and T. Takano, *Ferroelectrics,* **91,** 163 (1989)
[3] M. Tohda, S. Ichikawa, K. Uchino and K. Kato, *Ferroelectrics,* **93,** 287 (1989)
[4] B. Koc and K. Uchino, *Proc. of 19th ICAT Symp.,* Pennsylvania State Univ., USA (Oct. 1996)
[5] M.J. Park and J.S. Kim, *Proc. of KIEE,* Inha Univ., Korea (1998)

APPENDIX 64

PIEZOELECTRIC MICROMOTOR

USING A METAL-CERAMIC COMPOSITE STRUCTURE

Burhanettin KOC, *Student Member, IEEE*, Philippe BOUCHILLOUX

and Kenji UCHINO, *Member, IEEE*

Abstract- This paper presents a new piezoelectric micromotor design, where a uniformly-electroded piezoelectric ring bonded to a metal ring is used as the stator. Four inward arms at the inner circumference of the metal ring transfer radial displacements into tangential displacements. The rotor ends in a truncated cone shape and touches the tips of the arms. A rotation takes place by exciting coupled modes of the stator element, such as a radial mode and a second bending mode of the arms. The behavior of the free stator was analyzed using the ATILA finite element software. Torque vs. speed relationship was measured from the transient speed change with a motor load. A starting torque of 17 μNm was obtained at 20 Vrms. The main features of this motor are low cost and easy assembly owing to a simple structure and small number of components.

1

I. INTRODUCTION

Ultrasonic motors are generally categorized as travelling-wave or standing-wave types according to the type of vibration wave used on the stator. Currently, most miniaturized motors utilize a travelling elastic wave [1], [2] and present two major drawbacks. First, the piezoelectric element of a travelling wave motor, typically an annular ring, must be divided in sectors poled in alternately opposite directions. This makes the poling process complicated and damages many samples. Second, to produce a travelling wave on a vibrating piezoelectric element, at least two ac power sources with a 90-degree phase difference both in time and space are required. This results in a more complex drive and wiring.

Another important factor in the miniaturization of piezoelectric ultrasonic motors comes from the maximum level of vibrations that can be obtained from a piezoelectric element. The maximum vibration velocity of the piezoceramic limits the vibration amplitude [3]. As the size of a piezoelectric ultrasonic motor decreases, the resonance frequency of its stator increases. The vibration level, however, cannot be increased beyond a certain vibration velocity due to the limitation of the piezoelectric material. Therefore, a vibration magnification and transformation mechanism (vibration concentrator) is necessary on a stator element to amplify vibration amplitude on the piezoceramic material similar to projection teeth on the stator elements of traveling wave motors.

An alternative design to miniature piezoelectric motors consists of PZT thin films [4], [5], even though their properties are inferior to those of bulk piezoelectric ceramics.

2

However, the performance of thin-film motors is on the way of improvement in parallel with quality of thin films [6], [7].

In order to miniaturize piezoelectric motors we used a bulk piezoelectric material, and took the following approaches: i) the structure of the active piezoelectric element, including its poling configuration should be simple so as to be manufactured in small size; ii) the number of components used in the motor should be as few as possible to decrease the production cost. We proposed such an ultrasonic motor design using a metal-ceramic composite structure [8]. The stator in that motor consisted of a piezoelectric ring, poled uniformly in its thickness direction, bonded to two metal endcaps. Due to the multi-mode excitation (radial mode of the piezoelectric ring and bending mode of the metal endcaps), an elliptical motion was generated at the center of the top endcap where the rotor was placed.

The operating principle and structure of the motor presented in this work is similar to our previous design. However, in this new design, only one metal endcap was used. It was bonded to the piezoelectric ring and its center part was removed. Finally, the size of the stator vibrator was decreased to a diameter of 3.0 mm.

The structure and operating principle of the motor are provided first, then the finite element analysis of the stator vibrator is presented. The motor characteristics obtained with the transient response method are described last.

II. STRUCTURE AND OPERATING PRINCIPLE OF THE MOTOR

The motor is composed of four components: stator, rotor, ball-bearing and housing unit (Fig. 1). The key element to this motor is a multifunctional stator, which has a metal-piezoelectric composite structure. The piezoelectric part has a simple structure of

3

a ring electroded on its top and bottom surfaces (ϕ 3.0mm) poled uniformly in the thickness direction (Table I). The metal ring, whose dimensions are shown in Fig. 2, is machined using Electric Discharge Machining (EDM). It has four inward arms placed 90° apart on its inner circumference. The metal and piezoelectric rings are bonded together, but the arms remain free; they thus behave like cantilever beams. The length and cross-sectional area of each arm were selected such that the resonance frequency of the second bending mode of the arms is close to the resonance frequency of the radial mode of the stator. The rotor is placed at the center of the stator and rotates when an electric field is applied at a frequency between the radial and bending resonance modes. The truncated cone shape at the end of the rotor guarantees a permanent contact with the tips of the arms.

The operating principle of this motor is as follows: in the contraction cycle of the stator, the four arms at the center of the metal endcap clamp the rotor and push it in the tangential direction. Since the radial mode frequency of the stator is close to the second bending mode frequency of the arms, the respective deformations are added and the tips of the arms bend down. In the expansion cycle, the arms release the rotor from a different path such that their tips describe an elliptical trajectory on the surface of the rotor.

A. Design of the arms at the inner circumference of metal ring

The length of the inward arms was chosen such that the resonance frequency of the second bending mode of each individual arm neighbors the resonance frequency of the first radial mode of the stator. Using this strategy, it becomes possible to produce

4

multi-mode excitations with only a single electrical source [12], [13]. If we assume that each arm behaves like a simply cantilevered elastic beam, then their bending frequencies can be estimated according to the following expression [9]:

$$\omega_{b1} = \frac{X_n^2}{L^2} \sqrt{\frac{E t_m^2}{12\rho}} \tag{1}$$

where, L, t_m, ρ and E represent the length, thickness, density and Young Modulus of the beam, respectively. The frequency constants X_n's are determined from the following equation:

$$CosX_n CoshX_n = -1 \tag{2}$$

The first three values of the X_n^2's are 3.516, 22.03 and 61.7. Using these values and, the dimensions, and mechanical properties of the arms, the first three bending mode frequencies of the arms are estimated at 90.2, 494.1 and 1380 kHz. The second bending mode frequency of the arms is close to the stator's radial mode resonance frequency which is 461 kHz.

B. Force Transformation Mechanism

The force in the radial direction generated by the stator is transferred to the tangential direction at the periphery of the rotor via a mechanism, which is analogous to a slider-crank mechanism; assuming that the inward arms and the rotor are rigid (Fig. 2). When the stator is electrically excited to generate ultrasonic vibrations at its radial mode resonance frequency, the piezoelectric and metal rings expand and contract in the radial direction. The stator force due to the piezoelectric effect in the radial direction is

5

transferred to the rotor via the inward arms. Because of the angular orientation of the arms (angle φ with respect to the radial direction), there are normal and tangential force components at the periphery of the rotor. The normal (N_2) and tangential (T_2) force components at the rotor surface are calculated as a function of the angles θ (the angle between the origin of an arm and the contact point with the rotor), φ and the radial force F_A.

$$T_2 = F_A \cos(\varphi)\sin(\theta + \varphi) \tag{3a}$$

$$N_2 = F_A \cos(\varphi)\cos(\theta + \varphi) \tag{3b}$$

Finally, the normal force on the rotor surface is:

$$N_3 = F_A \cos(\varphi)\cos(\theta + \varphi)\cos(\alpha) \tag{4}$$

Since the length, width and thickness of the arms as well as the radius of the rotor, which touches tangentially to the arms, are fixed to match the bending frequency of the arms to the radial mode resonance frequency of the stator, the angles θ and φ were decided automatically. Small φ and large θ values are desirable to increase tangential force T_2, because the normal force between stator and rotor can be controlled by static pressing force F_N.

The maximum torque that the motor can generate is limited by the static pressing force, and is provided by $F_N/\sin\alpha$, where α is the taper angle at the tips of the arms ranging from 10 to 30 degree (17 degree for this experiment). The stator and the rotor contact surfaces are two mating cones that are kept in contact by the normal force. They thus constitute a conical clutch mechanism. The relation between the normal force F_N and torque capacity T is known by the following equation [11].

$$T = \mu \frac{F_N}{\sin\alpha} \frac{r_0 + r_i}{2} \tag{5}$$

6

where, μ, r_o, and r_i are friction coefficient, outer and inner radii of the rotor contact surface, respectively. The above torque, which is also called blocking torque, is the maximum torque that this motor can generate.

Since the normal force and the geometrical parameters used in the above expressions are all known, the friction constant can be estimated after measuring the stopping time of the motor, that is, after measuring the blocking torque of the motor.

III. FINITE ELEMENT ANALYSIS

In order to verify the conceptual operation principle described in the previous section, the ATILA finite element code was used extensively to analyze the behavior of the stator and the vibration transformation mechanism at the tips of the arms. Because of the asymmetrical behavior of the structure and the angular orientation of the inward arms, we modeled the entire stator. Figure 3 shows the 3D mesh of the free stator. The total number of nodes and second order brick elements used in the model were 2036 and 256, respectively, which caused computation times to be long (20 min per frequency, approximately). The dimensions and material properties used for modeling are given in Table I and Table II. The epoxy layer between the metal and piezoelectric ring was not included in the model.

A. Admittance Spectrum

The computed and experimental admittance spectra of the stator are compared in Figures 4a and 4b, respectively. This figure shows that the three-dimensional finite element model estimates all modes generated by the stator. It also makes it possible to identify some of these resonance modes (Fig. 4a). For instance, the highest peak at

7

477 kHz is the radial mode of the stator, whose mode shape is shown in Fig. 5a. Since only one side of the piezoelectric ring is mechanically loaded (the metal ring was bonded to one side of the piezoelectric ring), the displacement is not purely in plane. The stator takes a convex/concave shape as it contracts and expands in the radial direction. Also, a flexure mode is generated on the ring because the arms are located in four discrete locations (Fig. 5b). This mode, which is very close to the radial mode of the stator, is excited at 489 kHz and is the second peak in Fig. 4a. The third peak on the admittance spectrum corresponds to the second bending mode of the arms, which is shown in Fig. 5c. A (4,1)-like flexure mode is also excited in the ring at the bending mode frequency of the arms which bend in the width direction.

Although the fundamental radial resonance mode was estimated within less than 5 % error, magnitudes of the motional admittance values are not so good. Since the epoxy layer between the piezoelectric ring and the metal ring, as well as the damping caused by the cable connections, were not included in the finite element model, the losses in the FEA are less than in the experimental structure. As a result, the calculated motional admittance values are larger than the measured ones. Nevertheless, the magnitude of calculated off-resonance admittance matches very closely to the measured admittance.

B. Displacement Transformation Mechanism

In order to better understand the mechanism of transformation of the displacements that takes place at the stator/rotor interface (from the radial to the tangential direction), displacements versus frequency were also calculated using harmonic analyses of the ATILA code. The calculated displacement spectrum at nodes 101 and 854 are shown in Figures 6a and 6b. The node numbers 101and 854 are nodes

on the inner circumference of the metal ring, where the inward arms are connected, and on the tip of one arm, respectively (Fig 3). Figures 6a and 6b illustrate the displacement magnitudes of the arms as a function of frequency. For instance, the displacements in the z-axis are amplified for the second and third peaks of Figures 6a and 6b. This is due to the flexural mode of the stator and the bending modes of the metal arms. Finally, elliptical trajectories at nodes 101 and 854 were calculated for three different frequencies (477, 490 and 500 kHz) and plotted in Fig. 7. This figure also demonstrates that the magnitudes of the elliptical trajectories are amplified at the tips of the arms.

IV. MOTOR CHARACTERISTICS

When a motor size is decreased, characterizing the motor becomes more difficult. A non-contact characterization method, which was initially proposed by Nakamura [10], was used to characterize the motor. The principle of this method consists of mounting a load (usually a disk whose moment of inertia is known) onto the motor, running the motor, and, finally, analyzing the transient speed obtained as a function of time. More explicitly, the angular acceleration of the motor can be calculated by taking derivative of the measured speed. The transient torque is then calculated by multiplying the angular acceleration by the moment of inertia of the load, which is known. Using this method, the starting transient response of the motor gives the speed-torque relation. Similarly, the friction coefficient between the rotor and the stator is estimated from the transient response for stopping the motor.

Instantaneous output mechanical power (P_{out}) can also be calculated by multiplying torque (Γ) with angular speed (Ω). Input electrical power (P_{in}) is calculated from measured input voltage, current and phase angle between them. From

9

input and output powers the efficiency can be calculated by dividing output mechanical power to input electrical power.

A. Estimation of Load Characteristics

The load consists of a metal disk (10g) with a high moment of inertia (0.2 kg*mm^2) compared to that of the rotor. It is mounted onto the stator (0.25g) and guided by two ball bearings. The motor, whose frequency spectrum is shown in Fig. 4b (thick line), was driven with an AC voltage of 20 V at 468 kHz.

The position of the loaded motor is detected in a form of square pulses through an optical sensor (OMRON EE-SPZ401Y) that utilizes a photocell pair. The frequency of the square wave, which is proportional to the position, was converted into voltage using a frequency-to-voltage converter. Since the output voltage of the converter is proportional to the input frequency, the transient speed of the motor was obtained with a simple gain factor. Second derivative of the recorded data gives the angular acceleration. Finally, the product of the angular acceleration and the moment of inertia of the rotating disk (I) give the motor transient torque.

A typical transient response of the motor under loaded condition is shown in Fig. 8. An exponential curve fits the transient speed of the rotor:

$$\Omega = \Omega_0(1 - \exp(t/\tau_r)) \tag{6}$$

where, Ω_0 is the steady-state speed and τ_r is the time constant, which can be found by trial and error. The initial value of τ_r can be chosen as a quarter of the rise time. Then, it can be adjusted to obtain the best fit. For this particular measurement, Ω_0 and τ_r were found as 62 rad/sec and 0.74 sec, respectively.

A blocking torque of 25 μNm was obtained from the stopping time of the motor. Substituting 25 μNm in the torque capacity equation (5), gives an estimate of the friction constant as 0.15. This number is almost half of the expected friction constant between brass (stator) and steel (rotor). Finally, the load characteristics obtained from the transient speed are shown in Fig. 9. A starting torque of 17 μNm is one order of magnitude higher than that of a thin film motor with a similar size [7].

The difference between blocking torque (25 μNm) and starting torque (17 μNm) states that the arms, which were chosen thin enough to match their bending mode frequency to the stator radial mode frequency, are not strong enough to push the rotor, but they deform. On the other hand, an efficiency of more than 10 % is sufficient for real application with an output power of around 150 μWatts.

V. CONCLUSION

This paper presented a small piezoelectric ultrasonic motor whose active element is a bulk piezoelectric ring 3.0 mm in diameter and 0.5 mm in thickness. The stator produces a displacement transformation such that multi-mode resonance frequencies can be excited with only one ac source. The stator was analyzed with a three-dimensional model of the ATILA finite element analysis code, and its dynamic behavior was predicted. In particular, the FEA illustrated the bending and asymmetrical flexure modes that are generated close to the fundamental radial resonance frequency of the stator.

The rotation in this motor occurs by exciting the stator with a combination of two modes: the fundamental radial mode of the stator and the second bending mode of the arms.

11

The major applications of this motor will be micromechanical devices for the medical and microrobotic areas.

ACKNOWLEDGMENT

References

[1] M. Kasuga, T. Satoh, J. Hirotomi and M. Kawata, "Development of ultrasonic motor and application to silent alarm analog quartz watch", 4th Congress Eur. De Chronometrie, pp 53-56, Lausanne, 1992

[2] A. M. Flynn, "Performance of ultrasonic mini-motors using design of experiment", Smart Mater. Struct. 7, pp.286-294, Jan. 1998.

[3] S. Takahasi, Y. Sasaki and S. Hirose, "Driving Electric Field Effects on Piezoelectric Transducers", Jpn. J. Appl. Phys. Vol. 36, pp. 3010-3015, May 1997.

[4] A. M. Flynn, L. Tavrow, S. Bart, R. Brooks, D. Ehrlich, K. R. Udayakumar and L.E. Cross, "Piezoelectric micromotors for microrobots" IEEE J. Microelectromech. Syst. 1 pp. 44-51, Jan. 1992.

[5] P. Muralt, M. Kohli, T. Maeder, A. Kholkin, K. Brooks, N. Setter and R. Luthier, "Fabrication and characterization of PZT thin-film vibrators for micromotors", Sensors and Actuators, A 48 pp.157-165, 1995.

[6] T. Morita, M. Kurosawa and T. Higuchi, "Design of cylindrical ultrasonic micromotor to obtain Mechanical output", Jpn. J. Appl. Phys. Vol. 35 Part1, No. 5B, pp. 3251-3254, May 1996.

[7] G. A. Racine, P. Muralt and M. A. Dudois, "Flexural-standing-wave elastic force motor uzing ZnO and PZT thin film on micromachined silicon membranes for wristwatch applications", Smart Mater. Struct. 7, pp.404-416, Jan. 1998.

[8] B. Koc, A. Dogan, Y. Xu, R.E. Newnham and K. Uchino, "An ultrasonic motor using a metal-ceramic composite actuator generating torsional displacement", Jpn. J. Appl. Phys. Vol. 37 Part 1, No. 10, pp. 5659-5662, Oct. 1998.

[9] I. H. Shames, *Energy and Finite Element Methods in Structure Mechanics*, New York, Hemisphere,1995, p. 333.

[10] K. Nakamura, M. Kurosawa, H. Kurebayashi, and S Ueha, " An Estimation of load characteristics of an ultrasonic motor by measuring transient response", IEEE Trans. Ultrason., Ferroelect., Freq. Contr., vol. 38, pp. 481-485, September 1991.

[11] H. A. Rothbart, *Mechanical Design and System Handbook*, New York, McGraw Hill, 1964, 28.

[12] M. Fleischer, D. Stein, and H. Meixner, "New Type of Piezoelectric Ultrasonic Motor", IEEE Trans. Ultrason., Ferroelect., Freq. Contr., vol. 36, pp.614-619, November 1989.

[13] Le Letty, R. F. Claeyssen, F.Barillot. M.F. Six, P.Bouchilloux, "New linear piezomotors for high force/precise positioning application", SPIE Conference on Smart Structures and Integrated Systems, San Diego, CA, March 1998, pp 784-755.

TABLE I
Dimensions of the stator

Outer Diameter of Piezoelectric ring	R_{OP}	3.0 mm
Inner Diameter of Piezoelectric ring	R_{IP}	1.5 mm
Thickness of Piezoelectric ring	t_P	0.5 mm
Outer Diameter of Metal (Brass) ring	R_{OM}	3.0 mm
Inner Diameter of Metal ring	R_{IM}	2.4 mm
Thickness of Metal ring	t_m	0.15 mm
Length of the arm	L	1.02 mm
Radius of circular part at the tip of the arms	r	0.5 mm
Width of the arm	w_m	0.4 mm
Angle between arm and radial force direction	φ	25°
Angle between tips of the arm and radial force direction	θ	28.7^o
Tapering angle at the tips of the arms	α	17°

TABLE II.
Physical and piezoelectric properties of ceramic material
(APC International Ltd.)

Parameter	Symbol	Units	APC 841
Relative Permittivity	$\varepsilon^T_{33}/\varepsilon_0$	1	1380
	$\varepsilon^T_{11}/\varepsilon_0$	1	1490
Dielectric Loss	Tan δ	%	.35
Coupling Factors	k_p	I	.56
	k_{31}	I	.32
	k_{33}	I	.65
	k_{15}	I	.65
	k_L	I	.48
Piezoelectric Strain Constants	$-d_{31}$	10^{-12}C/N	109
	d_{33}		323
Stiffness	S^E_{11}	10^{-12}m^2/N	11.7
Constants	S^E_{33}		17.3
Mechanical Quality Factor	Q_m	I	1400
Density	ρ	G/cc	7.9

Figure Captions

Fig. 1(a). Encapsulated motor next to a 0.5 mm metallic pencil (Steel housing was coated with an epoxy insulator). (b) Structure of the motor showing the number of components.

Fig. 2. Top and cross-sectional view of the stator vibrator. The metal ring is bonded to piezoelectric ring from its outer circumference. Interface between inwardly directed arms and piezoelectric ring needs to be empty. Force is transferred from radial to tangential direction through the arms.

Fig. 3. ATILA 3D mesh of the stator vibrator (256 brick elements were used in the model with 2036 nodes)

Fig. 4. (a) calculated admittance spectrums of the free stator , b) measured admittance spectrums of the free stator and the motor (thick line).

Fig. 5 Top view of calculated mode shapes of the free stator. (a) Mode shapes at fundamental radial resonance frequency at 477kHz. Non-symmetric structure of the metal ring distorts radial mode shape and causes the stator to take a convex/concave shape. (b) A flexure mode close to radial mode resonance at 490kHz. (c) Mode shape corresponds to bending mode resonance frequency of the arms at 504kHz. (d) Another flexural mode at 569 kHz of the stator in lateral direction corresponding to the bending mode of the arms in the width direction.
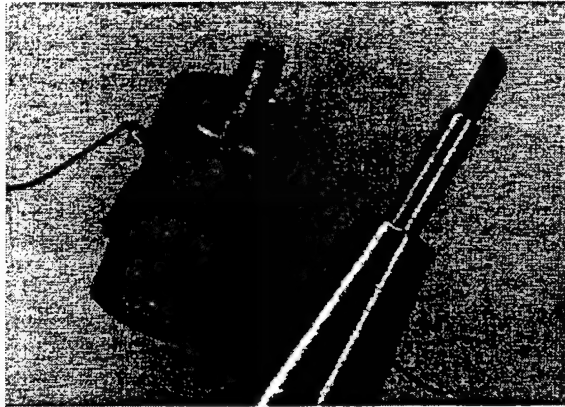
17

Fig. 6. Magnitude of calculated displacement spectrums. (a) at node 101, and (b) at node 854 (for location of nodes 101 and 854 see Fig. 3.)

Fig 7 Transformation and amplification of elliptical trajectories from circumference of the stator (node # 101) to the tips of the arms (node # 854) at frequencies: 477, 490 and 500 kHz. (for location of node 101 and 854 see Fig. 3.).
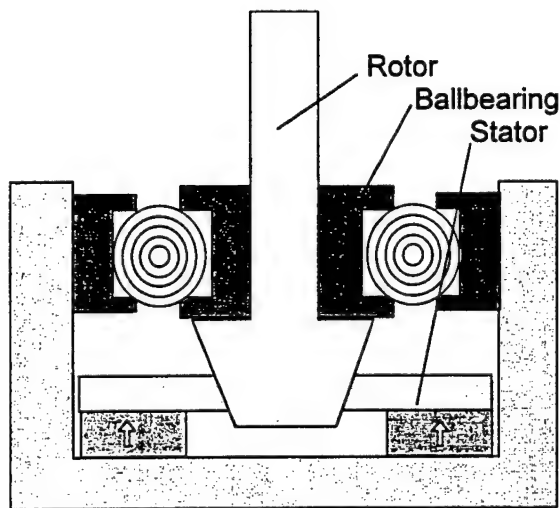
Fig. 8. Experiment setup to characterize small size motor using transient response method

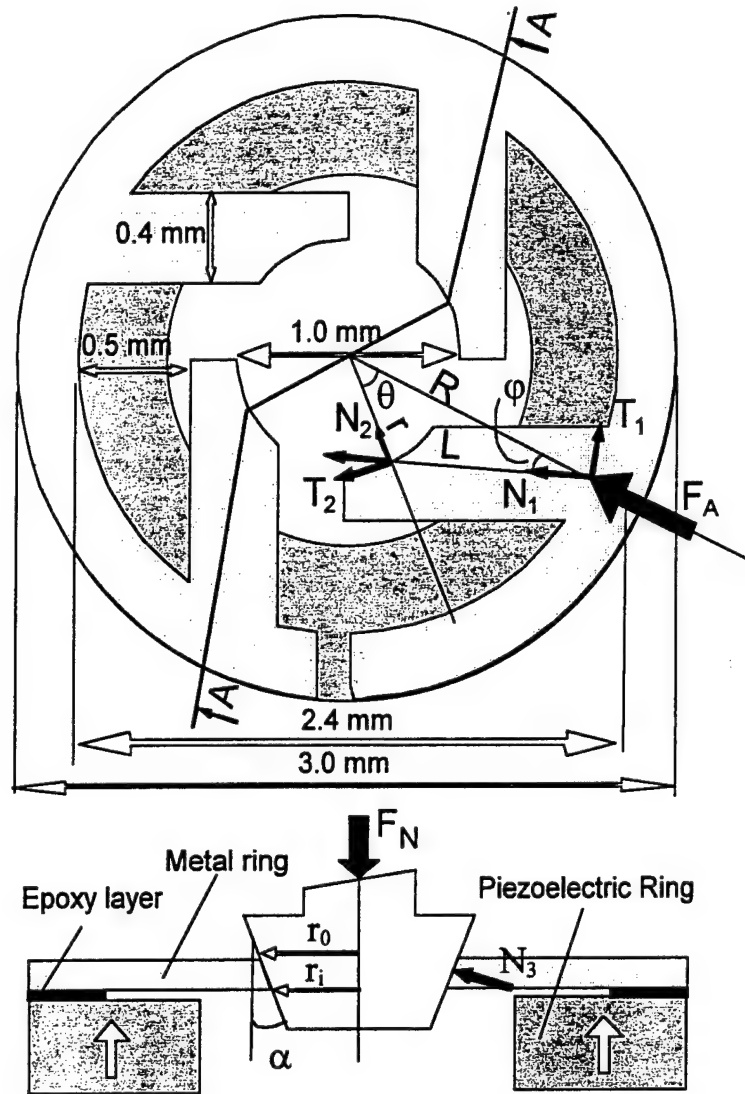Fig. 9. Transient response of the motor at 20V. Transient speed was curve fitted to an exponential function.

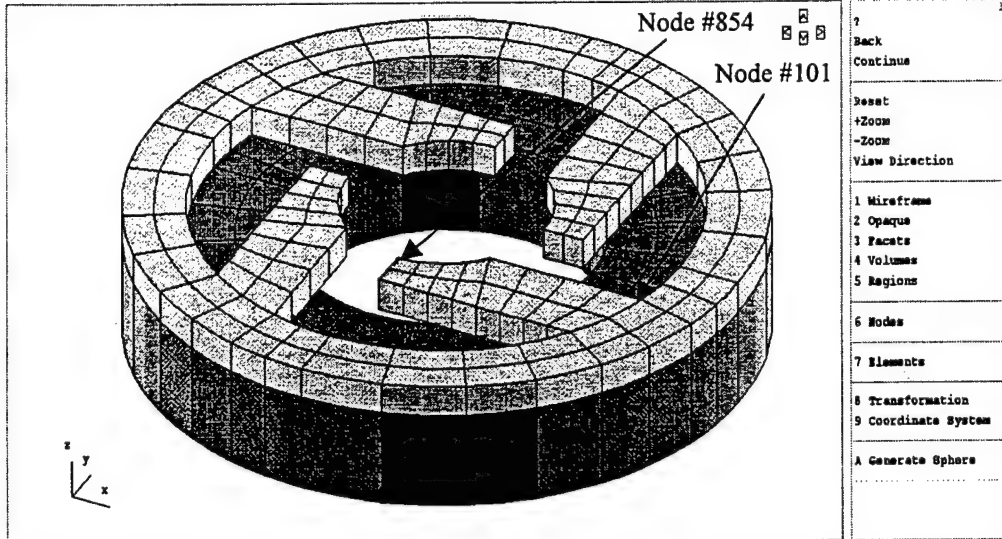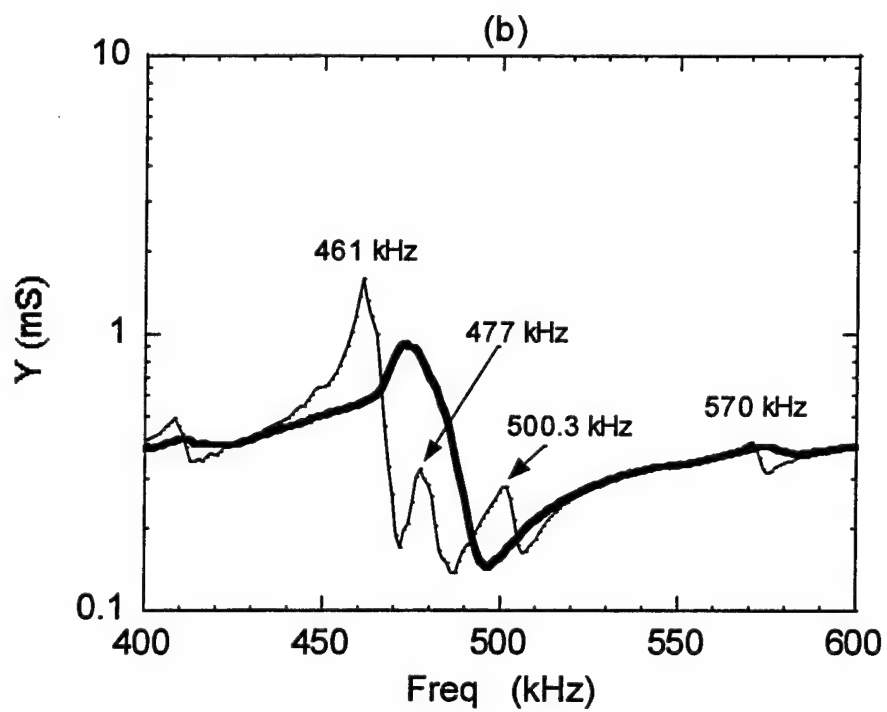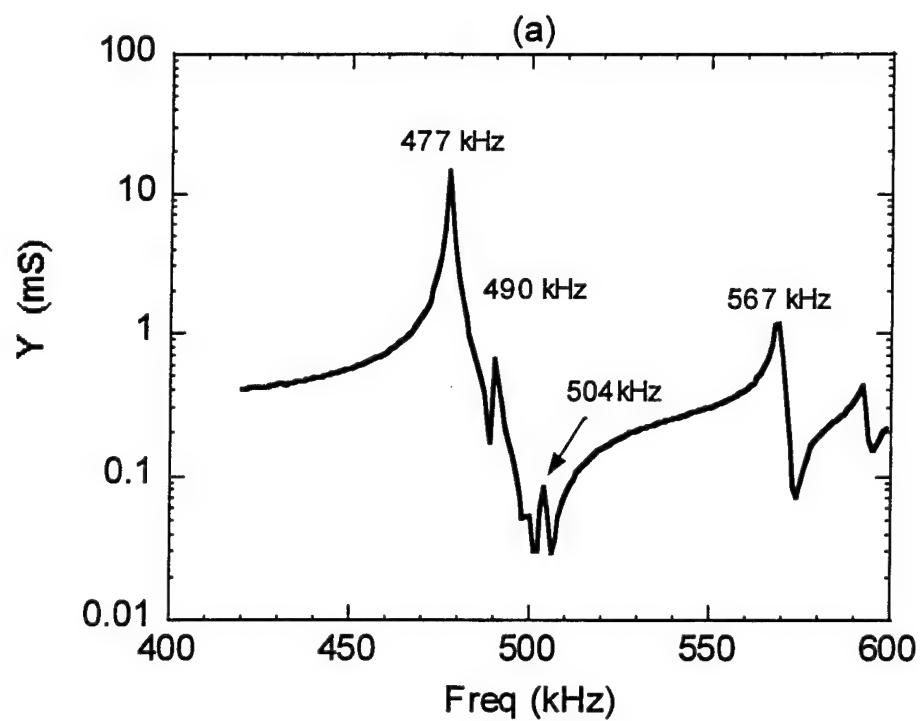Fig. 10. Load characteristics of the motor.

(a)

Rotor
Ballbearing
Stator

(b)

1

---

[1] Fig. 1a and b. Koc et al.

[1] Fig. 2. Koc et al.

02/12/99 10:02 ATILA PREPROCESSOR V5.11 - Mesh Modeling -

Node #854
Node #101

?
Back
Continue

Reset
+Zoom
-Zoom
View Direction

1 Wireframe
2 Opaque
3 Facets
4 Volumes
5 Regions

6 Nodes

7 Elements

8 Transformation
9 Coordinate System

A Generate Sphere

[1]

---

[1] Fig. 3. Koc et al.

(a)

(b)

[1] Fig. 4a and b. Koc et al.

(a) 477 kHz

(b) 490 kHz

(c) 504 kHz

(d) 567 kHz

(Re)

1

---

[1] Fig. 5. Koc et al.

THIS PAGE IS MISSING IN ORIGINAL DOCUMENT

FIG 6

Node #854
477kHz
490 kHz
500 kHz

Node #101
477kHz
490 kHz
500 kHz

x 10⁻⁸

5

z (m)

0

-5
1
0.5
x 10⁷
0
-0.5
-1
y (m)

1
0.5
0
-0.5
-1
x (m)
x 10⁷

[1]

---

[1] Fig. 7. Koc et al.

Rotary Encoder
and F-to-V Converter

PC

Metal Disk

Digital Storage
Oscilloscope

Signal Generator and
Power Amplifier Unit

Metal Disk

Ballbearing

Rotor

Stator

1

---

[1] Fig. 8. Koc et al.

¹ Fig. 9. Koc. et al.

[1] Fig. 10. Koc. et al.

Biographies

Burhanettin Koc was born in Kars, Turkey in 1968. He earned his B.S. and M.S degree from Hacettepe University, Ankara, Turkey in 1989 and 1992, respectively, both in Electrical and Electronics Engineering. He was a teaching and research assistant in the Electrical and Electronic Engineering Department at Hacettepe University from 1989 to 1993. He enrolled as a candidate for Ph.D. in 1994 in Electrical Engineering Department at the Pennsylvania State University. His research interests include high power piezoelectric devices: ultrasonic motors, piezoelectric transformers and microrobotics. He is a member of IEEE.

Philippe Bouchilloux is currently working on his Ph.D. in the Active Materials and Smart Structures Laboratory, headed by Dr. Kevin Craig, in the Department of Mechanical Engineering, Aeronautical Engineering and Mechanics at Rensselaer Polytechnic Institute. He received his Master degree from the same department in May 1997. Mr. Bouchilloux currently conducts his research on the design and applications of piezoelectric motors in the International Center for Actuators and Transducers at the Materials Research Laboratory of the Pennsylvania State University under the direction of Dr. Kenji Uchino.

Kenji Uchino, one of the pioneers in piezoelectric actuators, is the Director of International Center for Actuators and Transducers and Professor of Electrical Engineering at The Pennsylvania State University.

After being awarded his Ph. D. degree from Tokyo Institute of Technology, Japan, Uchino became Research Associate in physical electronics department at this university. Then, he joined the Sophia University, Japan as an Associate Professor in physics in 1985. He then moved to Penn State in 1991. He was also involved with Space Shuttle Utilizing Committee in NASDA, Japan during 1986-88, and was the Vice President of NF Electronic Instruments, USA, during 1992-94. He is the Chairman of Smart Actuator/Sensor Study Committee partly sponsored by the Japanese Government, MITI. He is also the executive associate editor for Journal of Advanced Performance Materials, and the associate editor of J. Intelligent Materials Systems and Structures.

His research interests are in solid state physics- especially dielectrics, ferroelectrics and piezoelectrics, including basic research on materials, device designing and fabrication processes, as well as development of solid state actuators for precision positioners, ultrasonic motors, etc. He has authored 300 papers, 30 books and 19 patents in the ceramic actuator area.

He is a Fellow of American Ceramic Society from 1997, and also is a recipient of the Outstanding Research Award from Penn State Engineering Society (1996), Best Movie Memorial Award at Japan Scientific Movie Festival (1989), and the Best Paper Award from Japanese Society of Oil/Air Pressure Control (1987).

1. Uchino, K and B. Koc: "Micro Air/Underwater Vehicle Powered by Piezoelectric Motor or Motor Array", US Patent Application, PSU Invention Disclosure No: 99-2090, (1999).

2. Koc, B., P. Bouchilloux and K. Uchino, "Piezoelectric Micromotor Using A Metal-Ceramic Composite Structure, " IEEE Transactions on Ultrasonic, Ferroelectrics, and Frequency Control. (Accepted for publication).

3. Koc, B, S. Alkoy and K. Uchino, "A Circular Piezoelectric Transformer with Crescent Shape Input Electrodes", IEEE Ultrasonic Symposium, Lake Thaon, NV, (1999)

4. Koc, B. and K. Uchino, "Disk Type Piezoelectric Transformer with Crescent Shape Input Electrodes", NATO-Advanced Research Workshop: Piezoelectric Materials, Advance in Science, Technology and Applications, Predeal, Romania, May 24-27, (1999).

1 Koc, B., Y. Gao and K. Uchino, "disk type piezoelectric transformer design employing high power piezoelectric ceramic material", MRS Fall Meeting, Boston, MA, (1999).

2 Koc, B, A. Amin, P. Bouchilloux, and K. Uchino, "Design of Circular Type Piezoelectric Transformer with off-Centered Input Electrodes ",Amer. Ceram. Soc. Annual Mtg., Indianapolis, Indiana, April 25-28, (1999).

3 Koc, B, P. Bouchilloux and K. Uchino, "Tiny Piezoelectric Ultrasonic Motor" 27th ICAT Smart Actuator Symposium, State Collage, April (1999).

4 Koc, B., P. Bouchilloux and K. Uchino, "Piezoelectric Motor Array For Micro Air Vehicles" US NAVY Workshop on Acoustic Transduction Materials and Devices, State Collage, April (1999).

MODELING and CHARACTERIZATION

Simulation

APPENDIX 65

Simulation of boundary condition influence in a second-order ferroelectric phase transition

Wenwu Cao[a]
Department of Mathematics and Materials Research Laboratory, The Pennsylvania State University, University Park, Pennsylvania 16802

Simon Tavener
Department of Mathematics, The Pennsylvania State University, University Park, Pennsylvania 16802

Shumao Xie
Materials Research Laboratory, The Pennsylvania State University, University Park, Pennsylvania 16802

Using a two-dimensional Ginzburg–Landau model and the finite-element computational method, we have calculated stable domain configurations resulting from a second-order ferroelectric phase transition for a finite-sized system. The boundary conditions applied here correspond to fully charge compensated situations, either by surface electrodes or by the injection of charges (or defects) near the sample surface. The domain wall thickness of a finite system without surface electrodes was found to become thinner as it approaches sample surfaces. This is distinctively different from that of an infinite system for which a planar wall assumption can be used. The orientation of the macroscopic polarization of a finite system without surface electrodes was found to be determined by its aspect ratio. A size effect was observed when all the dimensions were reduced simultaneously. The relaxation process in the formation of domains and the switching process have also been simulated for charge neutral boundary conditions using a time dependent Ginzburg–Landau model. The simulation results verified that the surfaces are the favored nucleation sites for domain switching. © *1999 American Institute of Physics.* [S0021-8979(99)02522-0]

I. INTRODUCTION

Many physical properties of technologically important materials are determined by mesoscopic structures, such as domains and domain walls. For example, it has been determined experimentally that 70% of the dielectric and piezoelectric contribution in ferroelectric materials can be attributed to domain related activities.[1,2] An understanding of the formation processes of such mesoscopic structures is therefore crucial for designing and engineering better active materials. A great deal of effort has already been invested in this area, including first principle calculations, analytical approaches, and computer simulations,[3–7] and some notable successes have been achieved. However, analytical solutions are generally limited to quasi-one dimensional (1D) solutions, and most simulations have used periodic boundary conditions for reasons of computational efficiency. While these procedures may be appropriate when dealing with very large systems, the growing trend towards making smaller and smaller particles and thin films provides new challenges. In particular, size effects have attracted more and more attention in the past few years due to the fast growing field of thin films and microelectromechanical devices. Static analyses using an isotropic surface layer for particles and a one-dimensional model for thin films have been carried out by several authors for ferroelectrics.[8–11]

An established way of treating finite sized materials in simulation studies is to use layered vacuum–material–vacuum composites and periodic boundary conditions. The periodic boundary conditions allow the use of computational efficient fast Fourier transform techniques. While this approach may be appropriate to approximate free boundary conditions if the volume of the vacuum region is sufficiently large, it cannot describe practical situations in which external boundary conditions are prescribed. For this reason, it is necessary to explore models that allow the direct application of external boundary conditions and numerical methods that make the computation size manageable. In this article we have used scale normalization and the finite-element method in an effort to simulate domain formation in a finite ferroelectric system with high computational efficiency. We focus on the effects of surfaces in a finite system under prescribed boundary conditions. In order for the problem to be well posed, full electric charge compensation is assumed, which can be achieved either through surface electrodes or by injection of charges (or the distribution of charged defects) to neutralize the polarization gradient near the sample surfaces.

The time evolution of the domain pattern under specified boundary conditions was also investigated using a time-dependent Ginzburg–Landau (TDGL) theory.[12] A variable time-step integration technique was used that allows the energy minima to be obtained efficiently. In this technique, the time step was increased by several orders of magnitude as the system approached equilibrium. Without prescribed polarization at the surfaces, a single domain state was found to be the global energy minimum, as expected, since domain walls contain positive energy and will be driven out of the

[a]Electronic mail: caomath.psu.edu

system without surface pinning. Because there is no depolarization energy for the neutralized system, multidomain states can exist only with prescribed polarization at the boundaries. For the case of charge injection near the surface region, polarization became geometry dependent and the aspect ratio was found to break the orientational degeneracy of the system due to the gradient energy. Our model does not involve the introduction of a surface layer; the surface effect is intrinsic and anisotropic.

In this preliminary exploration, we did not include the strain coupling in order to isolate the effects of electrical boundary conditions. The model system has a square to rectangular phase transition [which may also be used to describe the tetragonal to orthorhombic phase transition in a three-dimensional (3D) system with the tetragonal dimension fixed], and a square to rhombic transition.

An outline of this article is as follows. In Sec. II we introduce the model, in Sec. III we discuss the effects of boundary conditions on the formation of domains in equilibrium states, and in Sec. IV we discuss the time evolution of domain processes.

II. GINZBURG–LANDAU MODEL FOR SQUARE–RECTANGULAR AND SQUARE–RHOMBIC FERROELECTRIC PHASE TRANSITIONS

The model system we investigated is a two-dimensional (2D) analog of the perovskite structure with the positive and negative ions sitting at the center and corner of a square unit cell, respectively. The symmetry of the high temperature paraelectric phase is square. We assume that the system undergoes a proper second-order ferroelectric phase transition so that the system can be described by a fourth-order Ginzburg–Landau theory. Using the polarization as the order parameter, the free energy density for a second-order phase transition can be written as

$$
\begin{aligned}
f = {} & \alpha_1(P_1^2 + P_2^2) + \alpha_{11}(P_1^2 + P_2^2)^2 + \alpha_{12}P_1^2 P_2^2 \\
& + d_1\left[\left(\frac{\partial P_1}{\partial x_1}\right)^2 + \left(\frac{\partial P_2}{\partial x_2}\right)^2\right] + d_2\left(\frac{\partial P_1}{\partial x_1}\right)\left(\frac{\partial P_2}{\partial x_2}\right) \\
& + d_3\left[\left(\frac{\partial P_1}{\partial x_2}\right)^2 + \left(\frac{\partial P_2}{\partial x_1}\right)^2\right],
\end{aligned} \tag{1}
$$

where only the first coefficient $\alpha_1 = \alpha_0(T - T_c)(\alpha_0 > 0)$ is temperature dependent; all the other coefficients are assumed to be independent of the temperature. Unlike previously proposed models, the gradient energy in Eq. (1) is anisotropic.

Minimizing the free energy density described by Eq. (1) gives three types of stable homogeneous solutions as listed below.

A. Solution 1

For temperature $T > T_c$, $(\alpha_1 > 0)$ a paraelectric solution exists for which

$$
P_1 = P_2 = 0. \tag{2}
$$

The symmetry of this paraelectric state is square.

B. Solution 2

For temperature $T < T_c(\alpha_1 < 0)$, if $\alpha_{11} > 0$ and $\alpha_{12} > 0$, a rectangular ferroelectric phase is stable, and has four variants: $(\pm P_R, 0)$ and $(0, \pm P_R)$, where the spontaneous polarization P_R is given by

$$
P_R = \sqrt{\frac{-\alpha_1}{2\alpha_{11}}}. \tag{3}
$$

The symmetry of this low-temperature state is rectangular.

C. Solution 3

For temperature $T < T_c(\alpha_1 < 0)$, if $\alpha_{11} > 0$ and $-4\alpha_{11} < \alpha_{12} < 0$, a rhombic ferroelectric phase is stable. It also has four variants: $(\pm P_{Rh}, \pm P_{Rh})$, with the spontaneous polarization component, P_{Rh}, given by

$$
P_{Rh} = \sqrt{\frac{-\alpha_1}{4\alpha_{11} + \alpha_{12}}}. \tag{4}
$$

In order to compute an inhomogeneous static solution below T_c, one needs to solve the Euler equations,[2,3,13] that in this case are two coupled second-order nonlinear partial differential equations of the following form:

$$
\begin{aligned}
2d_1 P_{1,11} + d_2 P_{2,21} + 2d_3 P_{1,22} \\
= 2\alpha_1 P_1 + 4\alpha_{11}(P_1^2 + P_2^2)P_1 + 2\alpha_{12}P_1 P_2^2,
\end{aligned} \tag{5a}
$$

$$
\begin{aligned}
2d_1 P_{2,22} + d_2 P_{1,12} + 2d_3 P_{2,11} \\
= 2\alpha_1 P_2 + 4\alpha_{11}(P_1^2 + P_2^2)P_2 + 2\alpha_{12}P_2 P_1^2.
\end{aligned} \tag{5b}
$$

Under a quasi-1D approximation, these equations can be reduced to two coupled ordinary differential equations which could be addressed by the method given in Refs. 4 and 14. In this article, however, we will directly solve this set of partial differential equations using the finite-element method (see the Appendix) with several prescribed boundary conditions.

For demonstration purposes we only study the case of $\alpha_{12} > 0$, for which the rectangular phase is stable. The case of $\alpha_{12} < 0$ has a very similar physical appearance if one rotates the coordinate system 45°. For generality, Eq. (5) is converted into dimensionless form by making the following substitutions:

$$
\binom{P_1}{P_2} = P_R\binom{u}{v}, \tag{6}
$$

$$
\binom{x_1}{x_2} = \sqrt{\frac{d_1}{-a\alpha_1}}\binom{\xi}{\eta}, \tag{7}
$$

where $a(>0)$ is a dimensionless scaling factor included here to give the flexibility to adjust the strength of the gradient energy with respect to that of the Landau energy. In addition, we define three new dimensionless coefficients specifying the anisotropy of the gradient energy and the coupling strength between different polarization components,

$$
b = a\frac{d_2}{2d_1}, \tag{8a}
$$

$$c = a \frac{d_3}{d_1}, \tag{8b}$$

and

$$d = \frac{\alpha_{12}}{2\alpha_{11}}. \tag{8c}$$

The final dimensionless form of Eq. (5) is

$$a u_{\xi\xi} + b \nu_{\xi\eta} + c u_{\eta\eta} = -u + u^3 + (1+d)u\nu^2, \tag{9a}$$

$$a \nu_{\eta\eta} + b u_{\xi\eta} + c \nu_{\eta\eta} = -\nu + \nu^3 + (1+d)\nu u^2. \tag{9b}$$

For a given system, the gradient coefficients a, b, and c may be determined by inelastic neutron scattering experiments,[14,15] while the nonlinearity coefficient, d, can be obtained from measurements of the nonlinear dielectric constant.[16] In the current 2D model system, we will investigate a particular set of normalized constants to provide the general trend of the solutions. For any specific material one could apply the procedure described in this article to obtain the inhomogeneous solutions after determining these parameters from experiments.

The coupled partial differential equations, Eqs. (9a) and (9b), were solved using the finite-element method described in the Appendix. Nine node quadrilateral elements were used in our calculations and the density of the elements in any given direction reflects the real dimension in that direction. The dimensions of the system were normalized to 1 so that the computational procedure could be applied to any size through a scaling factor. The scaling factor was also used to convert the simulation results back to the original dimensions after the problem was solved in the normalized system.

III. EFFECTS OF BOUNDARY CONDITIONS ON THE FORMATION OF DOMAIN STATES

A. Surface electrodes versus charge injection

The natural boundary conditions arising in the finite-element solution technique correspond to a system with surface electrodes that is short circuited during the phase transition. The depolarization field is screened by the free charge so that the magnitude of the polarization can be maintained as a constant throughout the sample. Under this circumstance, a monodomain state is the global energy minimum.[17] Our model simulation quickly converges to such a single domain state. The initial guess used when solving Eq. (9) was generated by the time-dependent model described in Sec. IV.

The boundary condition $\mathbf{P}\cdot\mathbf{n}=0$ corresponds to the situation of charge injection (or charged defect concentration) near the surface region. This case reflects many realistic situations in which a surface layer develops with reduced polarization.[8–11] We found a strong aspect ratio effect when this boundary condition was applied. The polarization of the stable configuration was always parallel to the long dimension. In other words, the dimensional difference breaks the symmetry degeneracy of the two pairs of solutions under this boundary condition. Only at the critical aspect ratio of 1 do all four possible solutions (with orientation $\langle 10 \rangle$) have equal chances of forming.
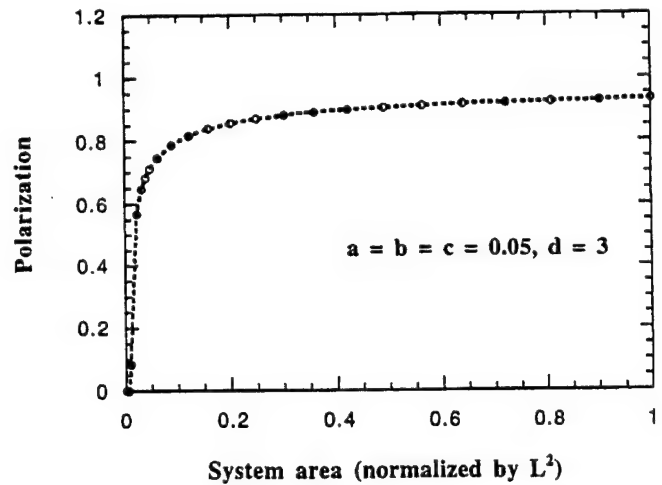

FIG. 1. Reduced effective polarization near surfaces causes a size effect. There is a critical size at which the effective polarization vanishes. The parameters used in the calculations are $a = b = c = 0.05$ and $d = 3$.

The implication of this result is that the natural state for a free standing thin film without surface electrodes should have polarization lying in the plane, although the net polarization would still be zero due to the in-plane random orientation. We must emphasize that this conclusion is only true for a free standing film, otherwise, the polarization orientation will be determined by the constraints originating from lattice constant mismatch between the film and the substrate, which is beyond the scope of this model system.

B. Size effects in a single domain system with P.n=0 boundary conditions

Size effects become increasingly important as material systems become smaller and smaller. Many experimental results showed that material properties degrade as the size decreases.[18–23] To determine this size effect, we used a square system of size $L \times L$ and continuously reduced the value of L. The net effective polarization is shown in Fig. 1. A critical size is clearly shown in the computational results although the actual value of the critical size depends on material parameters, particularly on the gradient coefficients. Our results are similar to those reported earlier by introducing an isotropic surface layer with reduced polarization.[11] The difference is that we did not make the assumption of a surface layer, but, rather, incorporated the gradient anisotropy and boundary conditions. Our model predicts strong size effects only when all the dimensions are being reduced at the same time. If the reduction is only in one of the dimensions, such as in thin films, the polarization can still be formed in the other larger dimension unless a reduced polarization layer is introduced.

Generally speaking, this critical size is directly related to the strength of the nonlocal interaction of the polarization, i.e., the amplitude of the polarization gradient coefficients.

C. Twin structures and their size dependence

Under the quasi-1D approximation, a single twin solution can be derived using the method described in Refs. 4
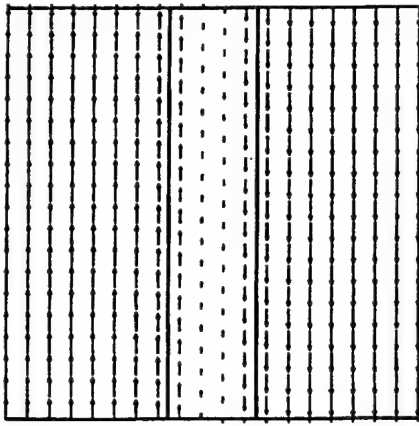
FIG. 2. Equilibrium configuration of a 180° twin with top and bottom surfaces electroded and the left and right boundaries being prescribed with the boundary condition of ±1 for the vertical component and zero for the horizontal component, respectively.

FIG. 4. Dependence of the domain wall thickness on the amplitude of the gradient coefficients. We chose $a=b=c$ for convenience to compare these results with that of 1D models. The dashed line is the square-root relationship obtained from a 1D model.

and 14 for infinite systems. Here, we study a finite system with surface electrodes at the top and the bottom surfaces and prescribe the polarization on the two side surfaces. The 180° twin and 90° twin solutions are shown in Figs. 2 and 3, respectively. In order to compare them with the quasi-1D solutions of Ref. 4, we look at the solution along the middle of the vertical dimension in the 2D structure (maximum domain wall width). The contour lines in Figs. 2 and 3 represent the position where the polarization amplitude has reached 79%[$=\tanh(1)$] of its maximum value. We take the region in between the two contour lines as the "domain wall." One can see that the domain wall thickness for the 90° twin decreases as it approaches the top and bottom surfaces. The corresponding parameters used for the simulation are given in the Figs. 2 and 3 captions.

The results imply that the quasi-1D assumption (plane wall assumption) is inadequate if the systems is very small. As shown in Fig. 3, the symmetry inside a 90° wall is lower
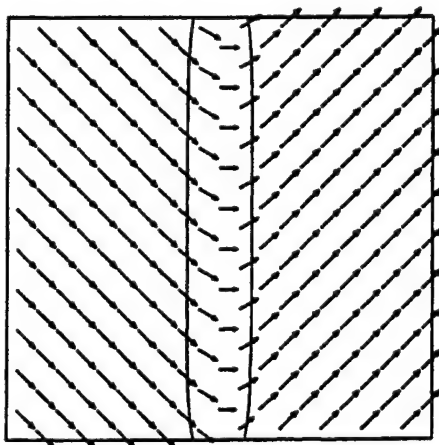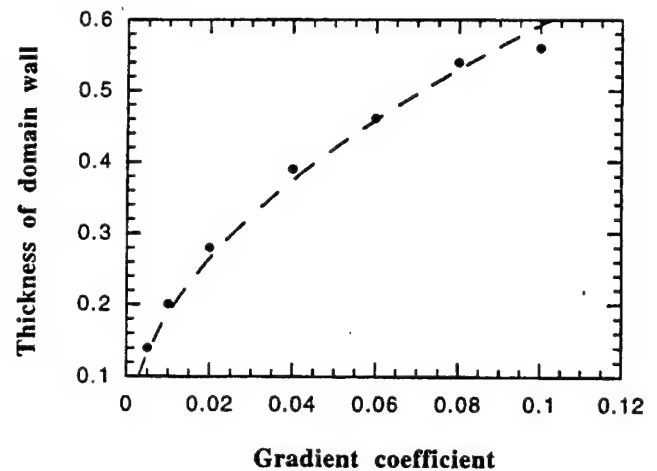

FIG. 3. 2D system with the dimensions parallel to [11] and [$\bar{1}$1]. The equilibrium configuration of a 90° twin is obtained with the top and bottom surfaces electroded and the left and right boundaries prescribed with the boundary condition of the polarization pointing to [10] and [01] directions, respectively (45° with respect to the surface orientations). The contour lines illustrate the change of domain wall width from the center to the top and bottom surfaces.

than that of the single domain regions, and the direction of the polarization at the center of the domain wall is along the diagonal direction of the unit cell (i.e., 45° from the single domain regions). In Fig. 4 we plot the domain wall thickness measured at the center of the simulated systems versus the gradient coefficient (for convenience, we have set a $a=b=c$) while keeping all the other parameters fixed. The dashed line is the square root relationship predicted by the 1D model, and the dots are our computational results. One can see that the simulation results agree well with the 1D analysis even when the wall thickness reached 50% of the system size. The deviation for the large gradient coefficient is caused by the boundary constraints to the domain wall.

IV. RELAXATION IN DOMAIN FORMATION AND FIELD INDUCED SWITCHING PROCESS

A time-dependent Ginzburg–Landau model can provide information about the time evolution of domain formation from a quenched state below T_c. The TDGL used here is a relaxation equation for a nonconserved order parameter, corresponding to model A described by Hohenberg and Halperin.[12] Simulations using periodic boundary conditions have revealed that the domain coarsening slows down considerably upon approaching equilibrium.[6,7] In order to simulate a finite system in direct space within a realizable time scale without having to invoke the periodic boundary condition, we used a variable time-step scheme that is described in the Appendix. The computational efficiency of this method allows us to perform real space finite size simulations and to explore the effects of boundary conditions.

The master equation used here is of the same form as model A described in Ref. 12:

$$\frac{\partial P_i}{\partial t} = -\Gamma \frac{\delta F}{\delta P_i} + R(r,t) + \Gamma E_i, \quad (i=1,2), \qquad (10)$$

where Γ is the kinetic coefficient, F is the volume integration of Eq. (1), $R(r,t)$ represents the Gaussian random noise, and E_i is the external electric field.

J. Appl. Phys., Vol. 86, No. 10, 15 November 1999

Cao, Tavener, and Xie   5743

When carrying out the simulation, $R(r,t)$ $[<10^{-4}]$, was only used for initiating the nucleation process at the beginning from a paraelectric state, and was neglected at later stages because it does not affect the ultimate equilibrium states. Using a normalized time τ and a frequency Ω defined by

$$\tau = -2\alpha_1\Gamma t, \tag{11}$$

$$\Omega = \frac{\omega}{-2\alpha_1\Gamma}, \tag{12}$$

and substituting the dimensionless variables and coefficients defined by Eqs. (6)–(8), we can derive the normalized governing equations for the temporal evolution of the normalized polarization under an external AC electric field.

$$u_{,\tau} = au_{,\xi\xi} + bv_{,\xi\eta} + cu_{,\eta\eta} + u - u^3 - (1+d)uv^2$$
$$- e_\xi\cos(\Omega\tau), \tag{13a}$$

$$v_{,\tau} = av_{,\xi\xi} + bu_{,\xi\eta} + cv_{,\eta\eta} + v - v^3 - (1+d)vu^2$$
$$- e_\eta\cos(\Omega\tau), \tag{13b}$$

where $e = E/(-2\alpha_1 P_R)$ is the amplitude of the dimensionless form of the external electric field.

Figure 5 shows the domain formation process with $\mathbf{P}.\mathbf{n}$ $=0$ boundary conditions from a quenched state below T_c. The simulation was initiated from a small amplitude random disturbance. Because the amplitude is too small to see at the beginning, we have multiplied the magnitude of the local polarization vectors by an amplification factor. For example, the amplitude of the polarization vectors drawn in Fig. 5(d) has been amplified 80 000 times. It is interesting to see that the amplitude of local polarization first shrank to almost zero before re-nucleating into small clusters which grew into many small domains. As the coarsening progressed, the dominant domains grew at the expense of the smaller ones. The final equilibrium state was determined by the nucleus whose local polarization amplitude reached the equilibrium value first. In order to compare the efficiency of the variable time step finite-element method used in our simulation, we define a unified dimensionless time $\Delta t_0 = 10^{-3}$ as the unit. Using this unit as a measure, the polarization evolution from Figs. 5(a)–5(f) will take 42 000 time steps. While using the variable time step method, it only took 140 variable time steps to reach the equilibrium state in Fig. 5(f), and this represents a tremendous saving of computational time. The time steps of both measures are given in the Fig. 5 caption.

Figure 6 is another simulation sequence with surface electrode boundary conditions. In this case, the equilibrium was reached in 14 000 time steps in the unit of Δt_0, but our simulation only required 110 variable time steps. It is important to point out that our simulation showed no size effect with the electroded surfaces in terms of the polarization for this case. This is the main difference between our model and previous models, which assumed a surface layer with reduced polarization.

Letting $\Omega \to 0$ in Eq. (13) we can simulate the quasistatic switching process. It is much easier to form nuclei of the opposite domain near the surface region because of the in-
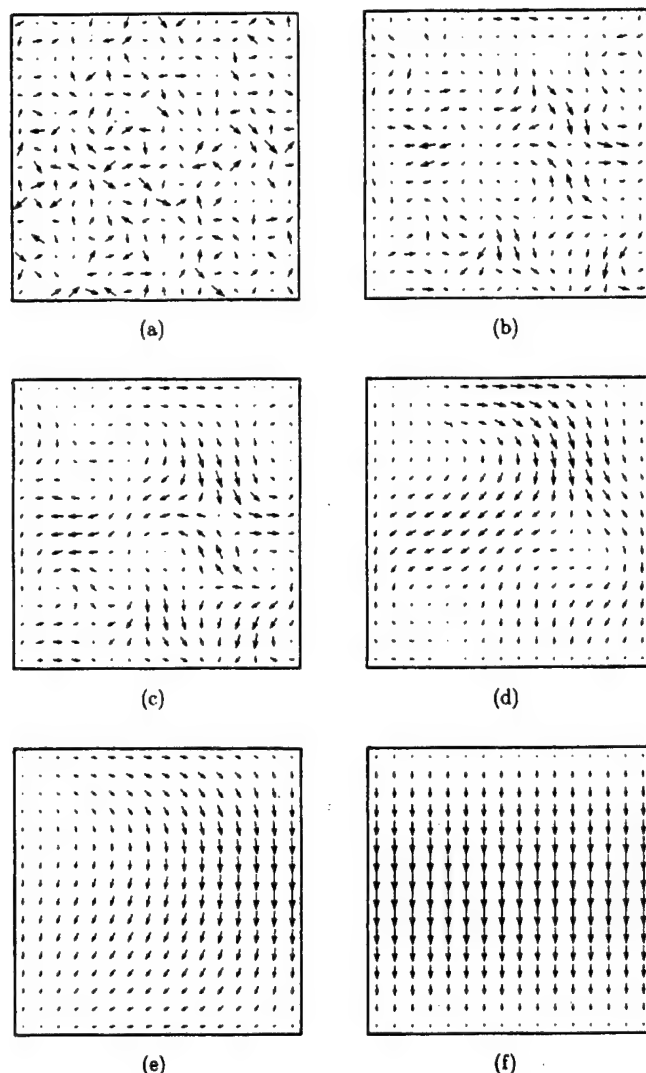

FIG. 5. Time evolution of the domain formation process from a random to a single domain state for the $\mathbf{P}.\mathbf{n}=0$ boundary condition. (a) $\tau=0$ and the amplitude of the local polarization has been amplified 3333 times; (b) 30 variable time steps$=35\Delta t_0$, and the amplitude of the local polarization has been amplified 20 000 times; (c) 35 variable time steps$=97\Delta t_0$ and the amplitude of the local polarization has been amplified 20 000 times; (d) 40 variable time steps$=350\Delta t_0$, and the amplitude of the local polarization has been amplified 80 000 times; (e) 45 variable time steps$=1600\Delta t_0$, and the amplitude of the local polarization has been amplified 6667 times; (f) 140 variable time steps$=42\,000\Delta t_0$ and there was no amplification at the local polarization vectors. The parameters used in the simulation are $a=0.045$, $b=0.055$, $c=0.05$, $d=2.5$, and $e=0$.

fluence of the boundary conditions. In our model the switching does not happen homogeneously in the whole system but, rather, nucleates at the surfaces and then progresses via the movement of domain walls. The time evolution of the domain switching process for a 90° twin structure is illustrated in Fig. 7. The net polarization of the twin was pointing to the right before application of an electric field, which is opposite to the initial polarization direction. Two domain walls formed near the left and the right surface regions at the beginning, then they moved toward each other and finally annihilated one another in the middle of the structure, forming a reversed twin with the effective polarization pointing to the left (the field direction). It is interesting to see that a swirl
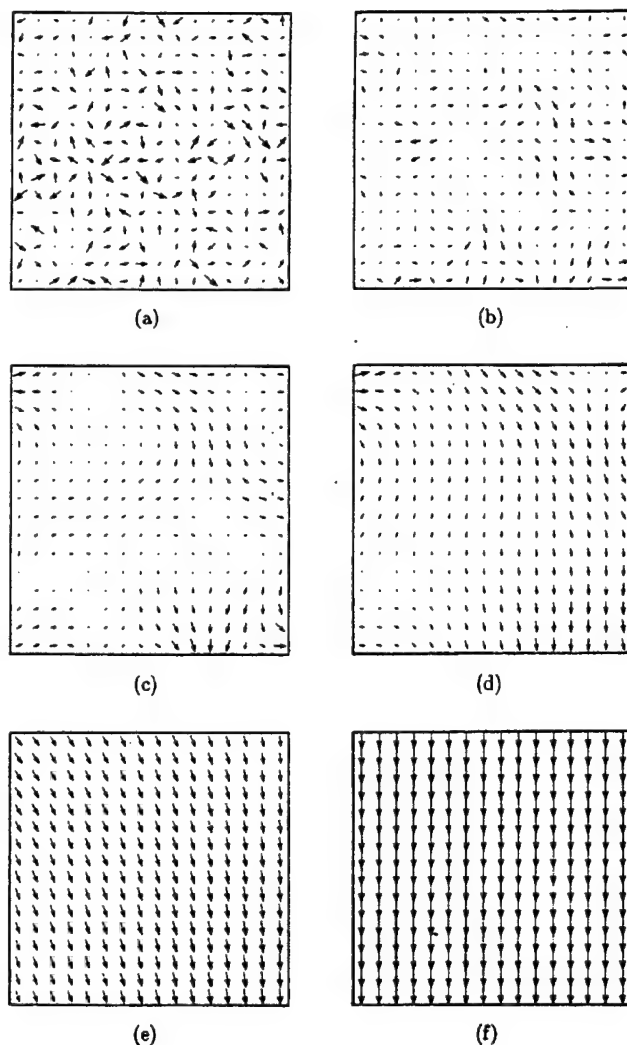
FIG. 6. Time evolution of the domain formation process from a random to a single domain state for a system with shortened surface electrodes (a) $\tau=0$ and the amplitude of the local polarization has been amplified 4000 times; (b) 35 variable time steps$=78\Delta t_0$ and the amplitude of the local polarization has been amplified 24 000 times; (c) 40 variable time steps $=230\Delta t_0$ and the amplitude of the local polarization has been amplified 40 000 times; (d) 45 variable time steps$=780\Delta t_0$, and the amplitude of the local polarization has been amplified 40 000 times; (e) 50 variable time steps$=3300\Delta t_0$ and the amplitude of the local polarization has been amplified 600 times; (f) 110 variable time steps$=14000\Delta t_0$, and there was no amplification of the local polarization vectors. The parameters used in the simulation $a=0.06$, $b=0.04$, 0.05, $d=2$, and $e=0$.

pattern developed in Fig. 7(d). Such a phenomenon can occur because our current model does not include elastic strain coupling. The walls are expected to be planar while moving under the force of the electric field if the elastic constraints are included.

V. SUMMARY AND CONCLUSIONS

A 2D ferroelectric model system has been investigated using a finite-element technique combined with a variable time step numerical scheme. The unique feature of our model is the introduction of the anisotropic gradient energy which is compatible with the structural symmetry. We also directly solved the coupled partial nonlinear differential equations rather than trying to reduce the problem to one
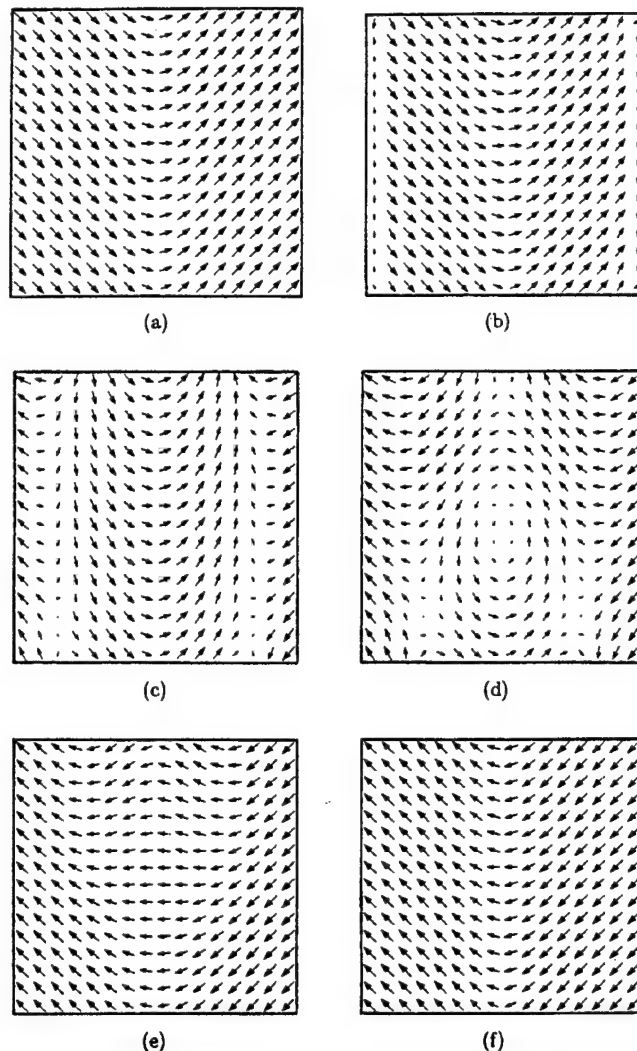

FIG. 7. Switching process of a 90° twin. The starting net polarization was pointing to the right. The time steps are (a) 0; (b) 80 variable time steps $=170\Delta t_0$; (c) 140 variable time steps$=6200\Delta t_0$; (d) 180 variable time steps$=17\,000\Delta t_0$; (e) 280 variable time steps$=30\,000\Delta t_0$; (f) 330 variable time steps$=37\,000\Delta t_0$. The parameters used for the simulations are $a=0.014$, $b=0.01$, $c=0.012$, $d=2.0$, and field amplitude $e=10^{-2}$. The switching process started at both surfaces on the left and right sides and propagates to the interior. Two domains walls form near the surfaces and they move toward each other until annihilation.

dimension. Due to the high efficiency of the numerical method, we were able to simulate both the equilibrium polarization configuration and the temporal evolution of the local polarization formation in a finite system with different boundary conditions. The simulation results agree well with all the known facts for a second-order ferroelectric phase transition, such as size effects, switching via surface nucleation–domain wall movement, and aspect ratio effects. In particular, we have demonstrated the temporal evolution of domain formation and the switching process in a 90° twin system.

ACKNOWLEDGMENTS

APPENDIX

We used the finite-element code ENTWIFE[24] to solve the following coupled system of partial differential equations [see Eq. (13)] in a rectangular domain D:

$$u,_\tau = au,_{\xi\xi} + b\,\nu,_{\xi\eta} + cu,_{\eta\eta} + u - u^3 - (1+d)u\,\nu^2$$
$$- e_\xi \cos(\Omega\tau), \tag{A1a}$$

$$\nu,_\tau = a\,\nu,_{\xi\xi} + bu,_{\xi\eta} + c\,\nu,_{\eta\eta} + \nu - \nu^3 - (1+d)\,\nu u^2$$
$$- e_\eta \cos(\Omega\tau). \tag{A1b}$$

The code ENTWIFE incorporates sophisticated parameter continuation capabilities and the ability to locate bifurcation points at which qualitative changes in the solution set occurs, making it particularly suitable to solve multiparameter problems. The numerical bifurcation techniques implemented in the code have proven to be useful to study a wide range of problems in fluid and other continuous systems.

In order to write Eqs. (A1a) and (A1b) in a form to which we can apply the standard finite-element approach (see, e.g., Refs. 25 and 26), it is convenient to introduce the notation,

$$p = \begin{pmatrix} u \\ \nu \end{pmatrix}, x_1 = \xi, \ x_2 = \eta, \ \frac{\partial}{\partial x_1} = \frac{\partial}{\partial \xi}, \ \frac{\partial}{\partial x_2} = \frac{\partial}{\partial \xi},$$

so that

$$p_{1,l} = u,_\xi \text{ and } p_{2,2} = \nu,_\eta, \text{ etc.}$$

First, consider the steady state problem without an external field. Let $f(p)$ be a vector valued function,

$$f_i(p) = \alpha p_{i,jj} + \beta p_{j,ij} + \gamma p_{k,ki} \quad (i = 1, 2), \tag{A2}$$

where $k = 3 - i$ with a summation over the repeated index $j = 1, 2$ (but not over k). Expanding Eq. (A2) using the original variables we have

$$f(p) = \begin{pmatrix} \alpha(u,_{\xi\xi} + u,_{\eta\eta}) + \beta(u,_{\xi\xi} + \nu,_{\xi\eta}) + \gamma\nu,_{\xi\eta} \\ \alpha(\nu,_{\xi\xi} + \nu,_{\eta\eta}) + \beta(u,_{\xi\eta} + \nu,_{\eta\eta}) + \gamma u,_{\xi\eta} \end{pmatrix}$$
$$= \begin{pmatrix} (\alpha + \beta)u,_{\xi\xi} + (\beta + \gamma)\nu,_{\xi\eta} + \alpha u,_{\eta\eta} \\ \alpha\nu,_{\xi\xi} + (\beta + \gamma)u,_{\xi\eta} + (\alpha + \beta)\nu,_{\eta\eta} \end{pmatrix}.$$

Defining a second vector-valued function $g(p)$ by

$$g(p) = \begin{pmatrix} u - u^3 - (1+d)u\,\nu^2 \\ \nu - \nu^3 - (1+d)u^2\,\nu \end{pmatrix},$$

the static problem without external field becomes

$$f(p) + g(p) = 0, \tag{A3}$$

provided constants α, β, and γ are related to constants a, b, and c as

$$\alpha = c, \quad \beta = a - c, \quad \gamma = b - c.$$

Let the boundary of domain D to be divided into two parts, $\partial D = \partial D_1 + \partial D_2$, where u and ν are specified on ∂D_1, i.e., $p = q$ on ∂D_1, and are not specified on ∂D_2.

We seek a solution $p \in V_q$ of Eq. (A3) where $V_q = \{p : p \in \mathbf{H}^1(D), p = q \text{ on } \partial D_1\}$. Here $\mathbf{H}^1(D)$ is the space of vector functions defined on D whose function values and first derivatives lie in $L^2(D)$. In the usual way, we construct the

weak form of Eq. (A3) by taking the dot product of $(f+g)$ with a (vector) test function r, and requiring that the integral of the dot product over the domain D vanishes for all test functions $r \in V_0$, where

$$V_0 \in \{p : p \in H^1(D_1) : p = 0 \text{ on } \partial D_1\}.$$

Summing over the repeated indexes i and j, notice that

$$\alpha \frac{\partial}{\partial x_j}(p_{i,j}r_i) + \beta \frac{\partial}{\partial x_j}(p_{j,i}r_i) + \gamma \frac{\partial}{\partial x_j}(p_{k,k}r_j)$$
$$= \alpha p_{i,jj}r_i + \beta p_{j,ij}r_i + \gamma p_{k,kj}r_i + \alpha p_{i,j}r_{i,j} + \beta p_{j,i}r_{i,j}$$
$$+ \gamma p_{k,k}r_{j,i}, \tag{A4}$$

where $k = 3 - j$.

By applying the divergence theorem in the plane,

$$\int\int_D (\alpha p_{i,jj}r_i + \beta p_{j,ij}r_i + \gamma p_{k,kj}r_j)d\xi d\zeta$$
$$= \int_{\partial D}(\alpha p_{i,j}r_i n_j + \beta p_{j,i}r_i n_j + \gamma p_{k,k}r_j n_i)ds$$
$$- \int\int_D (\alpha p_{i,j}r_{i,j} + \beta p_{j,i}r_{i,j} + \gamma p_{k,k}r_{j,j})d\xi d\zeta, \tag{A5}$$

where n is the outward surface normal. By including the terms in $g(p)$, the weak form of the steady state equations is

$$\int\int_\Omega \{[p_1 - p_1^3 - (1+d)p_1 p_2^2]r_1 + [p_2 - p_2^3 - (1+d)p_2 p_1^2]r_2$$
$$- [\alpha p_{i,j}r_{i,j} + \beta p_{j,i}r_{i,j} + \gamma p_{k,k}r_{j,j}]\}d\xi d\zeta = 0. \tag{A6}$$

Since the test functions r_i, $i = 1,2$ vanish on ∂D_1 by construction, the "natural" boundary conditions that apply on ∂D_2 arise from the requirement that the boundary integral term in Eq. (A5) vanishes for all possible test functions. The natural boundary conditions on ∂D_2 are, therefore,

$$\alpha p_{1,j}n_j + \beta p_{j,1}n_1 + \gamma n_1 p_{2,2} = 0, \tag{A7a}$$

$$\alpha p_{2,j}n_j + \beta p_{j,2}n_j + \gamma n_2 p_{1,1} = 0. \tag{A7b}$$

Rectangular elements with biquadratic interpolation were used to construct finite-dimensional subspaces $V_q^h \subset V_q$ and $V_0^h \subset V_0$. The finite-element method seeks to determine a (finite-dimensional) function $p_h \in V_q^h$ that satisfies Eq. (A6) for all $r_h \in V_0^h$.

A Gaussian quadrature was used to approximate the double integral in Eq. (A6) and the resulting nonlinear system of equations for the nodal degrees of freedom was solved via Newton's method. A direct method was used to solve the linear system at each Newton iteration.

The time-dependent problem in Eqs. (A1) can be written as an initial value problem of the following form:

$$\frac{dp}{dt} = h[p(t)], \quad t \in (0,T) \text{ with } p(0) = p_0. \tag{A8}$$

In our simulation, the method of Byrne and Hindmarsh[27] was used, which was designed for "stiff" initial value problems of the form

$$\frac{d\mathbf{Y}}{dt} = \mathbf{F}[\mathbf{Y}(t), t], \quad t \in (0, T) \quad \text{with} \quad \mathbf{Y}(0) = \mathbf{Y}_0, \qquad \text{(A9)}$$

where $\mathbf{F}: R^N \times R^I \to R^N$ is continuous and satisfies a Lipschitz condition. Solutions to stiff differential equations develop over a wide range of time scales. Unlike fixed time-step integration techniques, the method of Byrne and Hindmarsh is a variable time-step method based on backward difference formulas of the order 1–5. In such variable time-step methods, the interpolation knots of interpolating polynomials must be distinct but they are otherwise arbitrary, allowing considerable flexibility in the size of the time step. It has changed six orders of magnitude during our calculations of equilibrium states.

An initial estimate for the solution at the nth time step, $\mathbf{y}_{n0}$ is determined from prior solutions $\mathbf{y}_{n-i}$, $(i = 1, ..., q)$, and is subsequently corrected using the residual function $\mathbf{y}_{n0} - \mathbf{F}(\mathbf{y}_{n0}, t_n)$. The order of interpolation q and the stepsize h are varied in response to estimates of local discretization error and user provided tolerances. The order of the method q is restricted to change in steps of ± 1 only.

[1] A. G. Luchaninov, A. V. Shil'nikov, L. A. Shuvolov, and I. Ju. Shipkova, Ferroelectrics **29**, 47 (1980).

[2] A. V. Turik and A. V. Chernobabov, Zh. Tekh. Fiz. **47**, 1944 (1977).

[3] W. Cao and L. E. Cross, Phys. Rev. B **44**, 5 (1991).

[4] W. Cao and L. E. Cross, Ferroelectrics **157**, 19 (1994).

[5] D. Vanderbilt and W. Zhong, Ferroelectrics **206**, 181 (1998).

[6] S. Nambu and D. A. Sagala, Phys. Rev. B **50**, 5838 (1994).

[7] H. L. Hu and L. Q. Chen, J. Am. Ceram. Soc. **81**, 492 (1998).

[8] K. Binder, Ferroelectrics **35**, 99 (1981).

[9] D. R. Tilly and B. Zeks, Ferroelectrics **134**, 313 (1992).

[10] W. L. Zhong, Y. G. Wang, P. L. Zhang, and B. D. Qu, Phys. Rev. B **50**, 698 (1994).

[11] Y. G. Wang, W. L. Zhong, and P. L. Zhang, Phys. Rev. B **51**, 5311 (1995).

[12] P. C. Hohenberg and B. I. Halperin, Rev. Mod. Phys. **49**, 435 (1977).

[13] V. A. Zhirnov, Zh. Eksp. Teor. Fiz. **35**, 1175 (1958) [Sov. Phys. JETP **35**, 822 (1959)].

[14] W. Cao and G. R. Barsch, Phys. Rev. B **41**, 11319 (1990).

[15] W. Cao, J. Phys. Soc. Jpn. **63**, 1156 (1993).

[16] M. J. Haun and L. E. Cross, Ferroelectrics **99**, 13 (1989).

[17] P. Würfel and I. P. Batra, Ferroelectrics **12**, 55 (1976).

[18] M. H. Frey and D. A. Payne, Phys. Rev. B **54**, 3158 (1996).

[19] T. Takeuchi, K. Ado, T. Asai, H. Kageyama, Y. Saito, C. Masquelier, and O. Nakamura, J. Am. Ceram. Soc. **77**, 1665 (1994).

[20] W. Cao and C. A. Randall, J. Phys. Chem. Solids **57**, 1499 (1996).

[21] C. Randall, N. Kim, J. P. Kucera, W. Cao, and T. Shrout, J. Am. Ceram. Soc. **81**, 677 (1998).

[22] I. P. Batra, P. Würfel, and B. D. Silverman, Phys. Rev. B **8**, 3257 (1973).

[23] J. F. Scott, H. M. Duiker, P. D. Beale, B. Pouligny, K. Dimmler, M. Parris, D. Butler, and S. Eaton, Physica B **150**, 169 (1988).

[24] K. A. Cliffe, ENTWIFE (release 6.3) Reference Manual: ENTWIFE, INITIAL DATA, and SOLVER DATA Commands, AEAT-0823, 1996.

[25] C. Johnson, "Numerical solution of partial differential equations by the finite element method" (Cambridge University Press, Cambridge, 1987).

[26] S. C. Brenner and L. R. Scott, *The Mathematical Theory of Finite Element Methods* (Springer, Berlin, 1994).

[27] D. Byrne and A. C. Hinmarsh, ACM Trans. Math. Softw. **1**, 71 (1975).

APPENDIX 66

Acoustic band-gap engineering using finite-size layered structures of multiple periodicity

Mingrong Shen[a] and Wenwu Cao[b]

Materials Research Laboratory, The Pennsylvania State University, University Park, Pennsylvania 16802

The transmission coefficient of a layered structure made of glass and water was calculated using transfer matrix method and also measured as a function of frequency. It was found that acoustic band gaps can be created using only 3–4 cells of a two-phase layered structure. By introducing two or more periods into the layered structure, very sharp passbands and very broad stopbands can be engineered for acoustic waves. Such acoustic band-gap materials could be used for making high-quality acoustic filters, acoustic mirrors and vibration insulation devices in selective frequency range. © *1999 American Institute of Physics.* [S0003-6951(99)01549-1]

Photonic band-gap engineering in mesoscopic systems has been successfully realized by using crystals with periodic structures.[1,2] The fundamental principle is to use the periodic medium to regulate the propagation of electromagnetic waves. In the frequency window of the band gaps, electromagnetic waves cannot go through the crystal. In principle, the band-gap phenomena can be produced when the wavelength of the propagating waves approaches the period of the medium. As an analogue to photonic band-gap engineering, such band-gap phenomena also occur in the case of acoustic waves propagating in a periodic medium with the period comparable to the wavelength. Passbands and stopbands are produced in the frequency spectrum. In the frequency range of an acoustic (or phonotic) stopband, sound waves or ultrasonic vibrations cannot propagate. Such acoustic band-gap materials can have many practical applications, such as elastic/acoustic wave filters, ultrasonic silent blocks, acoustic mirrors, and ultrasonic array transducers. In the past, some interesting microscopic physical phenomena have been duplicated using ultrasonic waves with scale-up designs, such as the Anderson localization of sound and vibrations;[3–5] it is therefore natural to extend the photonic band-gap concept to acoustic waves. This letter reports an interesting study of using multiple periodicity and acoustic impedance difference to engineer large band gaps and/or narrow passbands using layered structure of finite size.

The materials under study are comprised of repeated cells made of two different materials with large acoustic impedance difference. The length scale of the period is the same as the wavelength of the acoustic waves. There has been growing interest in the band-gap materials in recent years. Several theoretical methods were developed in the past few years to study the band-gap formation, for example, the transfer matrix method,[6] plane wave method,[7,8] and effective medium method.[9] The first experimental study on ultrasonic band gaps reported in the literature was the measurement of sound attenuation in a sculpture.[10] Ultrasonic band gaps were also experimentally observed recently in one-

dimensional arrays and two-dimensional periodic composites for longitudinal waves.[11,12]

In this letter, we report a combined theoretical and experimental study on a finite one-dimensional layered medium containing two different periods. The main objective is to use the idea of band-gap engineering to fabricate materials that can have narrow passbands and/or very broad stopbands.

As shown in Fig. 1, the structure is made of two substructures with period d_1 and d_2, respectively, and each of them consists of four cells. Each substructure can produce its own band structures. If the passbands of the two substructures are not overlapped in certain frequency range, acoustic waves cannot pass through the entire structure creating a broader stopband; if they are partially overlapped, only the overlapped frequencies can pass through, thus, a filter of narrow passband could be obtained.

In Fig. 1, element type 1 and type 3 are glass plates while type 2 and type 4 are both water. A longitudinal acoustic plane wave was sent from the left at $x=0$. At time t, the wave function in the nth layer can be written as

$$\psi_{nj}=A_{nj}e^{i(2\pi ft-k_j x)}+B_{nj}e^{i(2\pi ft+k_j x)}$$
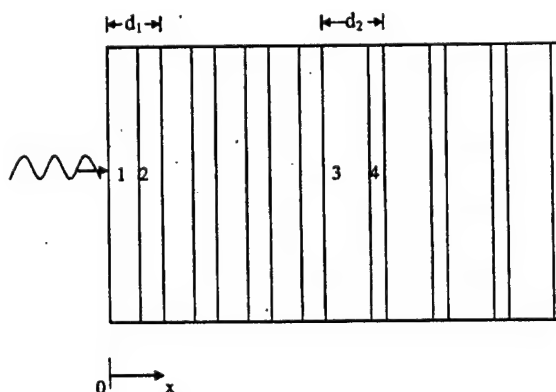
$$(j=1-4, \quad n=1-N), \tag{1}$$

FIG. 1. Schematic of the layered structure studied, which consists of two periodic substructures with period d_1 and d_2, respectively. Materials 1 and 3 are two different glasses and materials 2 and 4 are both water.

[a]Permanent address: Physics Department, Suzhou University, Suzhou 215006, People's Republic of China.
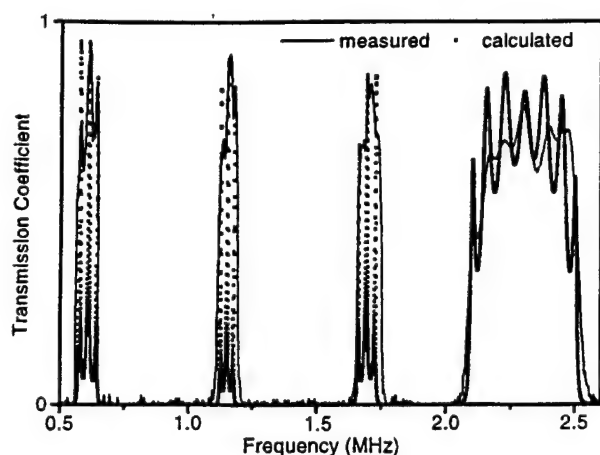[b]Electronic mail: cao@math.psu.edu

FIG. 2. Calculated and measured transmission coefficient as a function of frequency for a layered medium containing glass (1) and water (2). The thickness of glass is 1.23 mm and the water gap is 1.27 mm.
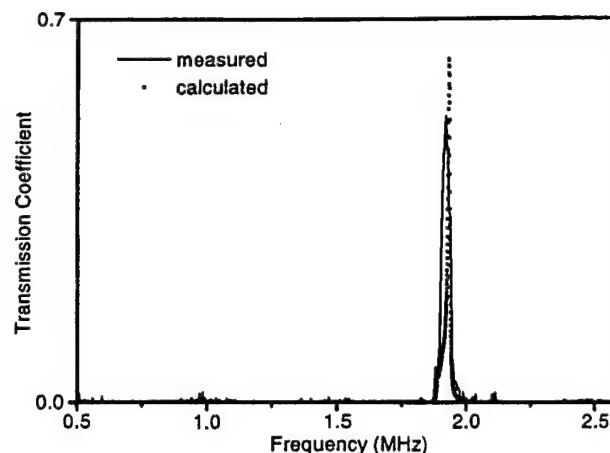

FIG. 3. Calculated and measured transmission coefficient for the structure shown in Fig. 1 as a function of frequency. The thickness of materials 1, 2, 3, and 4 are 1.23, 1.14, 3.00, and 0.51 mm, respectively.

where the first and second terms on the right-hand side of Eq. (1) represent the forward and reflected waves, respectively, $k_j = 2\pi f/c_j$ is the wave vector, and f and c_j are the frequency and phase velocity, respectively. The indices n and j are the cell number and material type, respectively.

The transfer matrix technique of Ref. 6 was used to calculate the acoustic band structures for the design given in Fig. 1. The properties of the materials used in the calculations are as follows:

Material 1: glass with density 2459 kg/m^3 and phase velocity 5660 m/s.

Material 3: glass with density 2767 kg/m^3 and phase velocity 5784 m/s.

Materials 2 and 4: distilled water with density 1000 kg/m^3 and phase velocity 1480 m/s.

Dissipation was included in the numerical calculations by adding a small imaginary component to the phase velocity in the glasses, i.e., $\tilde{c}_1 = (5660 + 10i)$ m/s and $\tilde{c}_3 = (5784 + 10i)$ m/s.

The experiments were conducted in a water tank using a setup similar to the one described in Refs. 12 and 13. Two broadband ultrasonic transducers were used for the measurements, one as transmitter and the other as receiver. In order to cover the interested frequency range of 0.5–2.6 MHz, two pairs of broadband ultrasonic transducers were used. The center frequencies of the transducers are 2.5 and 1.5 MHz, respectively, and the nominal active diameter of the transducers is 12 mm. The transmitting transducer was driven by a DPR35 pulser/receiver and the transmitted signal was received by a digital oscilloscope (Tektronix TDS 460A with fast Fourier transform analysis capabilities), then downloaded to a personal computer. Ten-signal average scheme was used to improve the signal-to-noise ratio during the measurements.

Shown in Fig. 2 are the calculated and measured frequency spectra of the transmission coefficient for a periodic layered structure with dimensions given in the figure caption. There are four passbands between the frequencies of 0.5 and 2.6 MHz. Gibbs type oscillations can be clearly seen in the calculated passbands and they are also confirmed by experiments within the experimental error. The Gibbs type oscillations here is similar to that reported in Ref. 12.

Figure 3 shows the calculated and measured frequency spectra of the transmission coefficient for the structure shown in Fig. 1, which has two different periods. It is intriguing to see that a very narrow passband is indeed obtained near 1.9 MHz. The agreement between the theoretical and experimental results is very good. Figure 4 shows the frequency spectra of the transmission coefficient of another design, for which the two substructures do not have overlapped passbands. As a result, no significant signal can pass through in the whole measured frequency range. Again, the calculated and experimental measured results agreed very well.

In conclusion, we have successfully engineered acoustic band-gap materials with either a very broad stopband or a very sharp passband. By changing the dimensions and type of materials used in the structure, the acoustic band-gap engineering concept of using multiple periodicity can be generalized to higher or lower frequency ranges. The produced acoustic band-gap materials have many potential applications, such as acoustic filters allowing only selective frequencies to pass through, ultrasonic silent block which can provide a vibration-free environment for high precision devices, and acoustic mirrors.
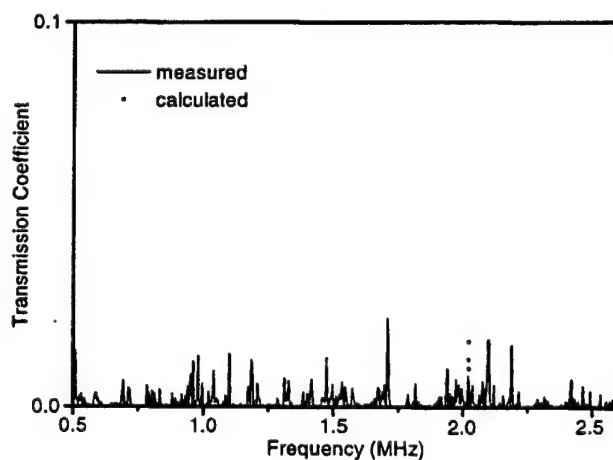

FIG. 4. Calculated and measured transmission coefficient as a function of frequency for another design of the structure shown in Fig. 1. The thickness of materials 1, 2, 3, and 4 are 1.23, 1.27, 3.00, and 0.51 mm, respectively.

[1] E. Yablonovitch, Phys. Rev. Lett. **58**, 2059 (1987).

[2] S. John, Phys. Rev. Lett. **58**, 2486 (1987).

[3] S. Parmley, T. Zobrist, T. Clough, A. Perez-Moller, M. Makela, and R. Yu, Appl. Phys. Lett. **67**, 777 (1995).

[4] R. L. Weaver, Wave Motion **12**, 129 (1990); Phys. Rev. B **47**, 1077 (1993).

[5] M. Belzons, P. Devillard, F. Dunlop, E. Guazzelli, O. Parody, and B. Suillard, Europhys. Lett. **4**, 909 (1987).

[6] W. Cao and W. K. Qi, J. Appl. Phys. **78**, 4627 (1995).

[7] M. S. Kushwaha and B. Djafari-Rouhani, J. Appl. Phys. **84**, 4677 (1998).

[8] C. Potel and J. F. Belleval, J. Acoust. Soc. Am. **93**, 2669 (1993).

[9] M. M. Sigalas and E. N. Economou, Europhys. Lett. **36**, 241 (1996).

[10] R. Martinez-Sala, J. Sancho, J. V. Sanchez, V. Gomez, J. Llinares, and F. Meseguer, Nature (London) **378**, 241 (1995).

[11] F. R. Montero de Espinosa, E. Jimenez, and M. Torres, Phys. Rev. Lett. **80**, 1208 (1998).

[12] R. James, S. M. Woodley, C. M. Dyer, and V. F. Humphrey, J. Acoust. Soc. Am. **97**, 2041 (1995).

[13] H. F. Wang, W. H. Jiang, and W. Cao, J. Appl. Phys. **85**, 8083 (1999).

APPENDIX 67

Field Induced Acoustic Emission (AE) in Ferroelectric Ceramics

Kenji Uchino and Hideaki Aburatani

International Center for Actuators and Transducers (ICAT),
Intercollege Materials Research Laboratory, The Pennsylvania State University,
University Park, PA 16802, USA

Abstract -- Electric field induced acoustic emission (AE) in ferroelectric PZT ceramics has been studied. It was shown that the field induced AE originated from where the displacement was induced and ended when the applied field was being reduced during poling. A larger electric field than the previously applied maximum field was required for new AE generation (Kaiser effect). From the AE event rate and the AE signal amplitude distribution, it was assumed that there were two origins of the bipolar field induced AE in the ferroelectric ceramics: deformation related to domain reorientation and piezoelectric deformation without domain reorientation.

§1. Introduction

In ferroelectric materials, the AE method has been used to determine phase change,[1-3] to detect domain reorientation[4-6] and to monitor crack propagation.[7-9] It has been believed that ferroelectric domain motion is a dominant AE source in the ferroelectrics. However, our recent research has shown a significant measurement problem in the most of previous field induced AE studies.[10] A mechanical vibration of sample is easily excited by an electrical coupling between the power supply feedback and the piezoelectricity of sample, resulting in a vibro-acoustic emission. The vibro-acoustic emission could vary with electric field, and was similar to the reported field induced AE results. The sample vibration could be eliminated by increasing the time constant τ of the voltage (field) application system. It was shown that this modified voltage (field) application method makes the field induced AE measurements at high sensitivities possible without vibro-acoustic emissions. Considerably different AE results from the reported field induced AE were obtained using the modified method. The AE appeared to be observed from where the displacement was induced during poling. New AE will not be generated after sufficient poling.

This paper deals with the electric field induced AE generations in a ferroelectric lead zirconate titanate $Pb(Zr_x,Ti_{1-x})O_3$ (PZT) ceramics. The field induced AE activities were analyzed by comparing them with obtained induced displacement. A fractal dimension analysis of the AE signal amplitude distribution was also applied.

§2. Experimental Setup

Figure 1 shows the field induced AE and displacement measurement system. The sample was placed on the AE sensor (NF Corporation, AE-904E) with its resonant frequency of 450 kHz. The induced displacement was also observed using a L.V.D.T (Millitoron, Nr. 1301). The AE signal was amplified by 40 dB through a low noise pre-amplifier (NF Corporation, AE-9913) and again up to 60 dB with a main amplifier (NF Corporation, AE-922). The amplified AE signals were counted after passing through a high-pass filter (f >100 kHz) and a discriminator.
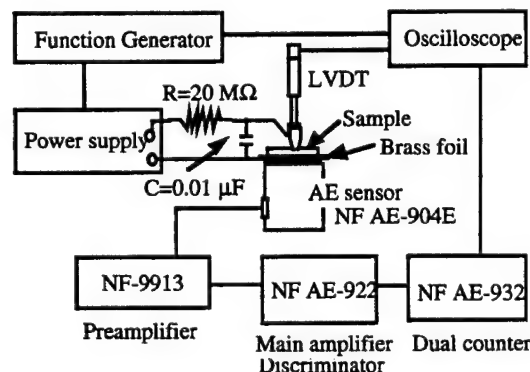

Figure 1 Field induced AE and displacement measurement system.

Disc specimens of commercialized ferro-electric lead zirconate titanate PZT ceramic (Morgan Matroc, PZT-5A) with 12.7 mm in diameter and 0.4 mm in thickness were employed for this study. Gold electrodes were formed on both surfaces by sputtering. The AE

sensor was attached to the sample through brass-foil with 0.025 mm in thickness. A silicone grease was used as a couplant to make a better acoustical contact. An external resistor R ($R = 20$ MΩ) and a capacitor C ($C= 0.01$ µF) were installed to the power supply in order to eliminate the vibro-acoustic emission.

§3. Results and Discussions

3.1 The Kaiser Effect in Field Induced AE

Figure 2 shows the AE event, induced displacement and applied electric field as a function of time for a cyclic application of various electric fields. The threshold level of the AE signal were set to be 400 mV at 100 dB. An unpoled sample was employed for this measurement. At the first cycle (poling), an electric field of 20 kV/cm was applied to the sample. The amplitude of the field was increased to be 25 kV/cm at the second cycle, and again up to 30 kV/cm at the third cycle.
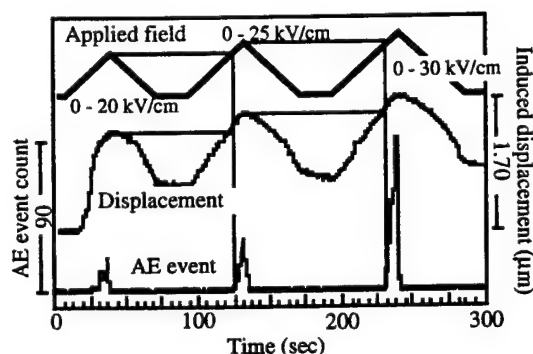

Figure 2 The AE event, induced displacement and applied electric field as a function of time for a cyclic application of various electric fields.

The sample was poled at the first cycle. The induced displacement and total residual displacement observed as a zero point shift increased with amplitude of applied field, because the higher degree of poling is achieved by the applications of the larger electric fields. At first cycle, the AE event occurred from where the displacement was induced and increased with field. The AE was not generated during the field was being reduced. In the second cycle, no AE events were observed until the electric field reached $E = 20$ kV/cm. New AE generation was observed above $E = 20$ kV/cm, and increased with the electric field. In the third cycle, this AE onset field again shifted to be $E = 25$ kV/cm.

The AE was generated only when the applied field exceeded the previous maximum value. This pre-applied electric field (induced displacement) dependence of the AE generation implies a Kaiser effect in the electric field induced deformation of the PZT ceramics.

The domain motion has been believed to be origin of the field induced AE. However, it is shown that all domain motions can not be the origin of the field induced AE, because the field induced AE depends on the pre-applied electric field (Kaiser effect). Therefore, particular domain reorientation processes rather than domain motion should be considered to be the origins of the AE. Another possible AE source is a mechanical stress, since the mechanical stress is supposed to be induced in the sample at high strain (electric field) state.

3.2 The Electric Field Induced AE

Figure 3 shows the AE event count rate and the induced displacement as a function of applied field at 0.0015 Hz with field of $E = \pm 35$ kV/cm. The AE measurement conditions were set to be at 100 dB with a threshold level of 400 mV. A butterfly shape induced displacement due to the domain reorientation was obtained. The critical electric field, where the AE started to be generated, corresponded to the point of inflection of the displacement with respect to the field. (In Fig 3, $d(displacement)/dE$ is shown for the point of inflection.)

The maximum of AE event count rate was not observed at the maximum applied field. The maximum AE event rate was found to be around $E = 27$ kV/cm. Considering that internal stress increases with the applied field in the ferroelectrics, this decrease in the AE event rate might imply that the internal stress could be the origin of the AE, but not only one source. The induced displacement in the ferroelectric ceramics consists of the deformation related to domain reorientation and piezoelectric deformation without the domain reorientation. Therefore, it was supposed that the field induced AE under bipolar electric fields in the PZT ceramics was generated first through deformation related to domain reorientation. After the domain reorientation was completed, the piezoelectric deformation unrelated to domain reorientation, which accompanied with the induced internal stress, was expected to be the origin of the AE. The decrease in the AE event rate might indicate the completion of the domain reorientation related deformation.
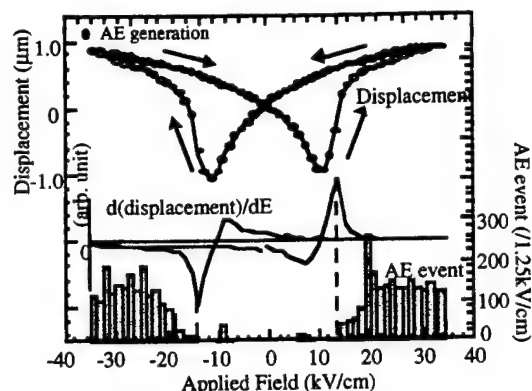
Figure 3   AE event count and the induced displacement as a function of applied field.

3.3 The Fractal Dimension of the Electric Field Induced AE

When the AE event rate $f(x)$ is the minus m-th power of x, where x is the AE signal amplitude,

$$f(x) = cx^{-m} \quad \text{(c: constant).} \quad (1)$$

The number of m is defined as a fractal dimension.[11] The fractal dimension m is used to estimate the damage in the materials.

The integrated AE event $F(x)$,

$$F(x) = \int_x^\infty f(x) \cdot dx = \frac{1}{m-1} cx^{-m+1} \quad (m > 1) \quad (2)$$

was observed through changing the AE signal threshold level in the measurements.

Figure 4 shows the AE event count per cycle as a function of the AE signal threshold level. The observed AE event count logarithmically decreased with the AE signal threshold level when a field of E = ± 25 kV/cm was applied. Thus, a fractal dimension of m=1 $(\frac{d}{dx}[c \log x + A] = c\, x^{-1})$ was obtained for the logarithmic decrease. In general, the fractal dimension is found to be more than 2 for the AE generated from the plastic deformation. The fractal dimension of m = 2 is a critical number to evaluate the condition of materials. If there is a damage (i.e., crack) in the material, the fractal dimension becomes lower than 2. From this concept of the fractal dimension, the obtained dimension indicated that the sample had been damaged. However, it is supposed that the lowered fractal dimension was due to the

existence of ferroelectric domain and the effect of the deformation related to domain reorientation, instead of the crack in the material, since repeatable and stable field induced AE events were observed.[12]
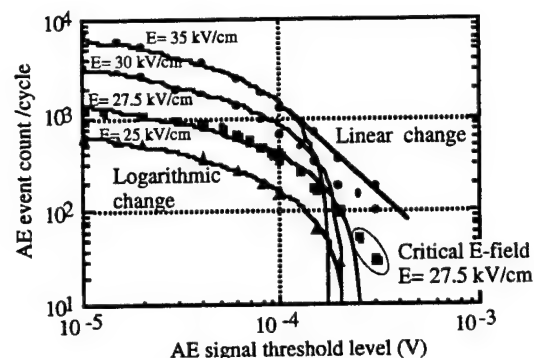

Figure 4   AE event count per cycle as a function of the AE signal threshold level for various bipolar electric field amplitudes.

When the amplitude of electric field was increased, the higher AE signal threshold level parts did not follow to the logarithmic change. A critical amplitude of the electric field, above which non-logarithmic AE distributions were observed, was found to be around E = 27 kV/cm. The lower signal threshold level region still could be fitted to a logarithmic curve and the extended line also ended around the AE signal threshold level obtained for ± 25 kV/cm. The higher AE signal threshold level parts ($>10^{-4}$ mV) showed a linear decrease with the threshold level. When an electric field of E = ±35 kV/cm was applied, a fractal dimension of m = 2.8 was obtained.   Figure 5 shows the induced displacement under unipolar and bipolar fields. Although the butterfly shape induced displacement for the bipolar field is due to the domain reorientation, the bipolar field induced displacement coincided with the unipolar field induced displacement above the electric field E = 27 kV/cm. Thus, it is assumed that the domain reorientation was completed at higher electric fields than the critical electric field E = 27 kV/cm.   The origin of the AE with the fractal dimension of 2.8 was assumed not to be the deformation related to domain reorientation, but the piezoelectric deformation without domain reorientation.
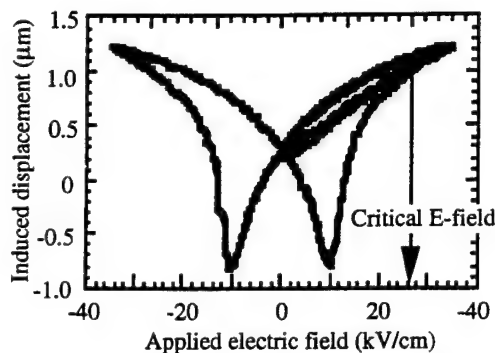
3

Figure 5   Field induced displacement under unipolar and bipolar fields.

It was shown that the fractal dimension of the field induced AE for the deformation related to domain reorientation ($m = 1$) was lower than that for the piezoelectric deformation without domain reorientation ($m = 2.8$). The fractal dimension greater than two corresponded to the plastic deformation. However, it was difficult to categorize the electrically induced deformation of ferroelectric ceramics as the plastic deformation, because the induced displacement recovers to the initial state after removing the field. Hence, it should be noted that the AE generation process in the ferroelectric ceramics could be different from that of reported AE in the materials such as metals and structural ceramics.

§4. Conclusion

The electric field induced acoustic emissions (AE) in the ferroelectric PZT ceramics were studied. It is shown that the Kaiser effect in terms of applied electric field (displacement) took place in the electric field induced deformation of ferroelectric PZT ceramics. The AE event rate as a function of applied field and AE signal threshold level distribution were employed to identify the origin of field induced AE. The AE event rate in ferroelectric PZT showed two origins: deformation related to domain reorientation and piezoelectric deformation without domain reorientation. It is assumed that the fractal dimension of the ferroelectric PZT ceramics consisted of the domain reorientation related $m = 1$ and the domain reorientation unrelated $m = 2.8$. A critical bipolar electric field for the domain reorientation unrelated AE generation was found to be $E = 37$ kV/cm.

Acknowledgment

Reference

1) P. Buchman: Solid State Electronics. **15** (1972) 142.
2) I. J. Mohamad, E. F. Lambson, A. J.Miller and G. A. Saunders: Phys. Lett. **A71** (1979) 115.
3) V.A. Kalitenko, V. M. Perga and I. N. Salivonov: Sov. Phys. Solid State **22** (1980) 1067.
4) H. Iwasaki and M. Izumi: Ferroelectrics **37** (1981) 563.
5) Y. Saito and S. Hori: Jpn. J. Appl. Phys **3 3** (1994) 5555.
6) W.Pan, H. Cao: Ferroelectrics, **129** (1992) 119.
7) D.G.Choi and S.K.Choi: J. Mat. Sci., **32** (1997) 421.
8) E.C. Subbarao, V. Srilkanth, W. Cao, L.E. Cross: Ferroelectrics **145** (1993) 271.
9) H. Aburatani, S. Harada, K. Uchino, A. Furuta and Y. Fuda: Jpn. J. Appl.Phys. **33** (1994) 3091.
10) H. Aburatani and K. Uchino, Jpn. J. Appl. Phys. **35**(1996) L516.
11) H.Nakasa:*Theoretical Bases and Applications of Acoustic Emission*, (Chijin Shokan Co. Ltd., Tokyo, 1994) 1st ed. (in Japanese).
12) H. Aburatani, J. P. Witham and K. Uchino, Jpn. J. Appl.Phys. **37**(1998) 602.

APPENDIX 68

LOSS MECHANISMS IN PIEZOELECTRICS
-- Extrinsic and Intrinsic Losses --

K. Uchino, J. Zheng, Y.H. Chen, X. Du, S. Hirose*, S. Takahashi**
International Center for Actuators and Transducers, Materials Research Laboratory, The Pennsylvania State University, University Park, Pa 16802, kenjiuchino@psu.edu
*Faculty of Engineering, Yamagata University, Yonezawa 992, Japan,
**Research and Development Group, NEC Corporation, 4-1-1 Miyazaki, Miyamae-ku, Kawasaki 216, Japan

ABSTRACT

Losses in piezoelectrics are considered in general to have three different mechanisms; dielectric, mechanical and piezoelectric losses. This paper deals with the phenomenology of losses, first, then how to measure these losses separately in experiments.

INTRODUCTION

Loss or hysteresis in piezoelectrics exhibits both merits and demerits. For positioning actuator applications, hysteresis in the field-induced strain provides a serious problem, and for resonance actuation such as ultrasonic motors, loss generates significant heat in the piezoelectric materials. Further, in consideration of the resonant strain amplified in proportion to a mechanical quality factor, low (extrinsic) mechanical loss materials are preferred for ultrasonic motors [1-3]. On the contrary, for force sensors and acoustic transducers, high mechanical loss, which corresponds to a low mechanical quality factor Q_m, is essential to widen a frequency range for receiving signals.

However, not much research effort has been put into systematic studies of the loss mechanisms in piezoelectrics, particularly in high voltage and high power range [4-6]. Since not many comprehensive descriptions can be found in previous reports [7], this paper will clarify the loss mechanisms in piezoelectrics phenomenologically, first, then how to measure these losses separately in experiments.

GENERAL CONSIDERATION OF LOSS AND HYSTERESIS

Extrinsic Losses

We will start from the Gibbs free energy G in a piezoelectric material expressed by

$$dG = - x \, dX - D \, dE - S \, dT, \tag{1}$$

and

$$G = - (1/2) \, s^E X^2 - d \, X \, E - (1/2) \, \varepsilon^X \varepsilon_0 \, E^2. \tag{2}$$

Here, x is strain, X, stress, D, electric displacement, E, electric field, S, enthalpy and T is temperature. Equation (2) is the energy expression in terms of intensive physical parameters (externally controllable parameters) X and E. Temperature dependence is carried into the elastic compliance s^E, the dielectric constant ε^X and the piezoelectric constant d. We will obtain the following two piezoelectric equations:

$$x = - (\partial G/\partial X) = s^E X + d E, \tag{3}$$
$$D = - (\partial G/\partial E) = d X + \varepsilon^X \varepsilon_0 E. \tag{4}$$

Note that thermodynamical equations and the consequent piezoelectric equations (Eqs. (1)-(4)) cannot yield a loss, without taking into account irreversible thermodynamic equations or dissipation functions, in general. However, the latter considerations are mathematically equivalent to the introduction of complex physical constants into the phenomenological equations, if the loss can be treated as a perturbation.

Therefore, we will introduce complex parameters ε^{X*}, s^{E*}, and d^* in order to consider the hysteresis losses in electric, elastic and piezoelectric coupling energy :

$$\varepsilon^{X*} = \varepsilon^{X}(1 - j \tan \delta'), \tag{5}$$
$$s^{E*} = s^{E}(1 - j \tan \phi'), \tag{6}$$
$$d^* = d (1 - j \tan \theta'). \tag{7}$$

Note that the negative connection in Eqs. (5)-(7) come from the time "delay." θ' is the phase delay of the strain under an applied electric field, or the phase delay of the electric displacement under an applied stress. Both delay phases should be exactly the same if we introduce the same complex piezoelectric constant d^* into Eqs.(3) and (4). δ' is the phase delay of the electric displacement to an applied electric field under a constant stress (i.e., zero stress) condition, and ϕ' is the phase delay of the strain to an applied stress under a constant electric field (i.e., short-circuit) condition. We will consider these phase delays as "extrinsic" losses.

Figures 1(a) - 1(d) correspond to the model hysteresis curves for practical experiments: D vs. E curve under a stress-free condition, x vs. X under a short-circuit condition, x vs. E under a stress-free condition and D vs. X under an open-circuit condition for measuring charge (or under a short-circuit condition for measuring current), respectively.

The stored energies and hysteresis losses for pure electrical and mechanical energies can be calculated as:

$$U_e = (1/2) \varepsilon^{X} \varepsilon_0 E_0^2, \tag{8}$$
$$w_e = \pi \varepsilon^{X} \varepsilon_0 E_0^2 \tan \delta' ; \tag{9}$$

$$U_m = (1/2) s^{E} X_0^2, \tag{10}$$
$$w_m = \pi s^{E} X_0^2 \tan \phi' . \tag{11}$$

The electromechanical loss, when measuring the induced strain under an electric field, is more complicated, because the field vs. strain domain cannot be used for directly calculating the energy. Let us calculate the stored energy U_{em} during a quarter electric field cycle (i.e., 0 to E_0) , first :
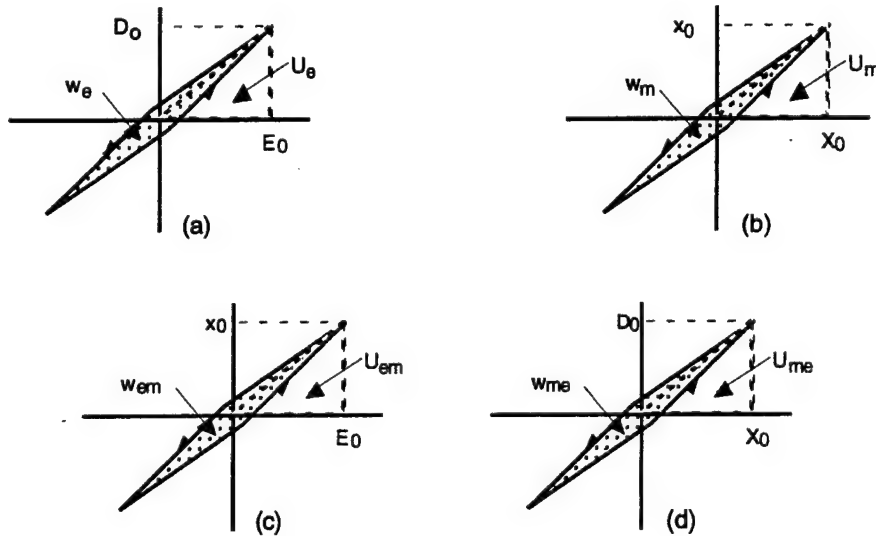

Fig.1   (a) D vs. E (stress free), (b) x vs. X (short-circuit), (c) x vs. E (stress free) and
(d) D vs. X (open-circuit) curves with a slight hysteresis in each relation.

$$U_{em} = -\int x\, dX = (1/2)\, (x_0^2/s^E) = (1/2)\, (dE_0)^2/s^E$$
$$= (1/2)\, (d^2/s^E)E_0^2 \qquad\qquad (12)$$

Replacing d and s^E by $d^* = d\,(1 - j\tan\theta')$ and $s^{E*} = s^E(1 - j\tan\phi')$, we obtain

$$U_{em} = (1/2)\, (d^2/\, s^E)\, E_0^2, \qquad\qquad (13)$$
and
$$w_{em} = \pi\, (d^2/\, s^E)\, E_0^2\, (2\tan\theta' - \tan\phi'). \qquad\qquad (14)$$

Note that the strain vs. electric field measurement seems to provide the piezoelectric loss $\tan\theta'$ directly, however, the observed loss should include an additional elastic loss because the strain should be delayed to the initial stress, which is needed to calculate energy.

Similarly, when we measure the induced charge under stress, the stored energy U_{me} and the hysteresis loss w_{me} during a quarter and a full stress cycle, respectively, are obtained as

$$U_{me} = (1/2)\, (d^2/\, \varepsilon_0\varepsilon^X)\, X_0^2, \qquad\qquad (15)$$
and
$$w_{me} = \pi\, (d^2/\, \varepsilon_0\varepsilon^X)\, X_0^2\, (2\tan\theta' - \tan\delta'). \qquad\qquad (16)$$

Hence, from the measurements of D vs. E and x vs. X, we obtain $\tan\delta'$ and $\tan\phi'$, respectively, and either the piezoelectric (D vs. X) or converse piezoelectric measurement (x vs. E) provides $\tan\theta'$ through a numerical subtraction.

Intrinsic Losses

So far, we discussed the "extrinsic" electric, mechanical and piezoelectric losses. In order to consider real physical meanings of the losses, we will introduce the "intrinsic" losses. When we start from the energy expression in terms of extensive physical parameters (material's intrinsic parameters) x and D, that is,

$$dA = X\, dx + E\, dD - S\, dT, \qquad\qquad (17)$$

we can obtain the piezoelectric equations as follows:

$$X = (\partial A/\partial x) = c^D x - h\, D, \qquad\qquad (18)$$
$$E = (\partial A/\partial D) = -h\, x + \kappa^X\kappa_0\, D. \qquad\qquad (19)$$

We introduce the intrinsic electric, mechanical and piezoelectric losses as

$$\kappa^{X*} = \kappa^X\, (1 + j\tan\delta), \qquad\qquad (20)$$
$$c^{D*} = c^D\, (1 + j\tan\phi), \qquad\qquad (21)$$
$$h^* = h\, (1 + j\tan\theta). \qquad\qquad (22)$$

It is notable that the permittivity under a constant strain (i. e., zero strain or completely clamped) condition, ε^{X*} and the elastic compiance under a constant electric displacement (i. e., open-circuit) condition, s^{D*} can be provided as an inverse value of κ^{X*} and c^{D*}, respectively. Thus, using the exactly the same losses in Eqs. (20) and (21),

$$\varepsilon^{X*} = \varepsilon^X(1 - j\tan\delta), \qquad\qquad (23)$$
$$s^{D*} = s^D(1 - j\tan\phi), \qquad\qquad (24)$$

We will consider these phase delays again as "intrinsic" losses.

Here, we consider the physical property difference between the boundary conditions; E constant and D constant, or X constant and x constant. When an elecric field is applied on a piezoelectric sample as illustrated in the top of Fig. 2, this state will be equivalent to the superposition of the following two steps: first, the sample is completely clamped and the field E_0 is applied (pure electrical energy $(1/2) \, \varepsilon^X \varepsilon_0 \, E_0^2$ is input); second, keeping the field at E_0, the mechanical constraint is released (additional mechanical energy $(1/2) \, (d^2/s^E) \, E_0^2$ is necessary). The total energy should correspond to the total input electrical energy $(1/2) \, \varepsilon^X \varepsilon_0 \, E_0^2$; thus, we obtain the relation,

$$\varepsilon_0 \varepsilon^X = \varepsilon_0 \varepsilon^x + (d^2/s^E), \tag{25}$$

Similarly, from the bottom of Fig. 2,

$$s^E = s^D + (d^2/\varepsilon_0 \varepsilon^X). \tag{26}$$

Hence, we obtain the following equations:

$$\varepsilon^x/\varepsilon^X = (1 - k^2), \tag{27}$$
$$s^D/s^E = (1 - k^2), \tag{28}$$

where

$$k^2 = d^2/(s^E \, \varepsilon_0 \varepsilon^X). \tag{29}$$

Fig. 2 Conceptual figure for explaining the relation between ε^X and ε^x, s^E and s^D.

Similarly,

$$\kappa^X / \kappa^x = (1 - k^2), \tag{30}$$
$$c^E / c^D = (1 - k^2), \tag{31}$$

where

$$k^2 = h^2/(c^D \kappa^x \kappa_0). \tag{32}$$

This k is called the *electromechanical coupling factor*, and is the same as the k in Eq. (29), because the equation $d^2/(s^E \varepsilon_0 \varepsilon^X) = h^2/(c^D \kappa^x \kappa_0)$ can be verified mathematically. We define the k as a real number in this manuscript.

In order to obtain the relationships between the extrinsic and intrinsic losses, the following three equations are essential:

$$\varepsilon_0 \varepsilon^X = [\kappa^x \kappa_0 (1 - h^2/(c^D \kappa^x \kappa_0))]^{-1}, \tag{33}$$
$$s^E = [c^D (1 - h^2/(c^D \kappa^x \kappa_0))]^{-1}, \tag{34}$$
$$d = [h^2/(c^D \kappa^x \kappa_0)] [h (1 - h^2/(c^D \kappa^x \kappa_0))]^{-1}. \tag{35}$$

Replacing the parameters in Eqs. (33) - (35) by the complex parameters in Eqs. (5) - (7), (20) - (22), we obtain the relationships between the extrinsic and intrinsic losses:

$$\tan \delta' = (1/(1 - k^2))[\tan \delta + k^2(\tan \phi - 2 \tan \theta)], \tag{36}$$
$$\tan \phi' = (1/(1 - k^2))[\tan \phi + k^2(\tan \delta - 2 \tan \theta)], \tag{37}$$
$$\tan \theta' = (1/(1 - k^2))[\tan \delta + \tan \phi + (1 + k^2) \tan \theta], \tag{38}$$
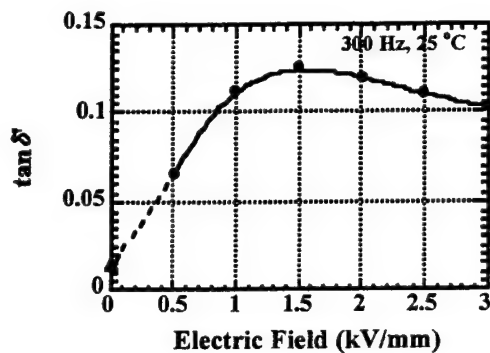
where k is the electromechanical coupling factor defined by either Eq. (29) or Eq. (32), and here as a real number. It is important that the extrinsic dielectric and elastic losses are mutually correlated with the intrinsic dielectric, elastic and piezoelectric losses through the electromechanical coupling k^2, and that the denominator $(1 - k^2)$ comes basically from the ratios, $\varepsilon^x / \varepsilon^X = (1 - k^2)$ and $s^D/s^E = (1 - k^2)$, and this real part reflects to the dissipation factor when the imaginary part is devided by the real part.
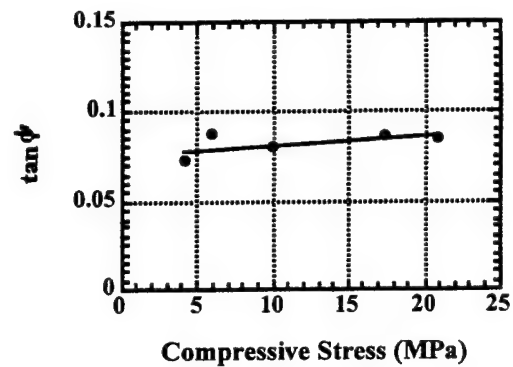
EXPERIMENTAL RESULTS

Figure 3 shows "extrinsic" dissipation factors determined from (a) D vs. E (stress free), (b) x vs. X (short-circuit), (c) x vs. E (stress free) and (d) D vs. X (open-circuit) curves for a PZT based soft multilayer actuator. Figure 4 shows the result for the piezoelectric loss tanθ'. We used the correlation factor between electric field and compressive stress given averagely by $X = (\varepsilon_0 \varepsilon^X/s^E)^{1/2} E$.

From Figs. 3 and 4, we can calculate the "intrinsic" losses as shown in Fig. 5. Note that the piezoelectric losses tanθ' and tanθ are not so small as previously believed, but comparable to the dielectric and elastic losses, and increase gradually with the field or stress. The experimental details will be reported in the successive papers.
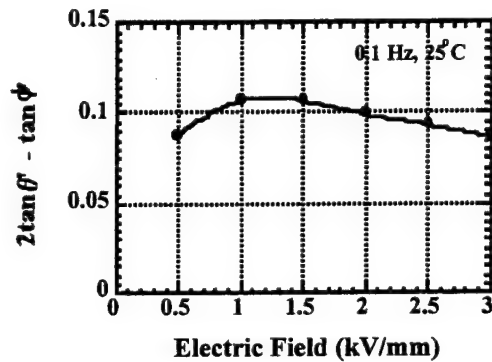
When similar measurements to Figs. 1(a) and 1.(b), but under constrained conditions; that is, D vs. E under a completely clamped state, and x vs. X under an open-circuit state, respectively, we can expect smaller hystereses; that is, intrinsic losses, tanδ and tanφ. These measurements seem to be alternative methods to determine the three losses separately, however, they are rather difficult in practice.
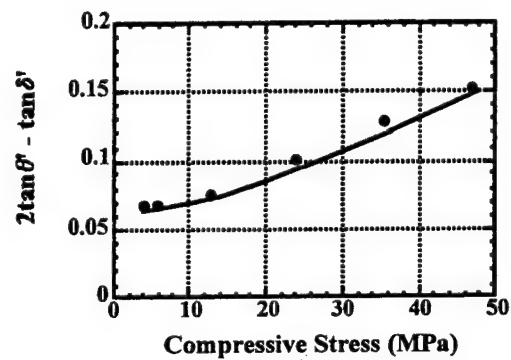
Fig.3 Dissipation factors determined from (a) D vs. E (stress free), (b) x vs. X (short-circuit), (c) x vs. E (stress free) and (d) D vs. X (open-circuit) curves for a PZT based actuator.
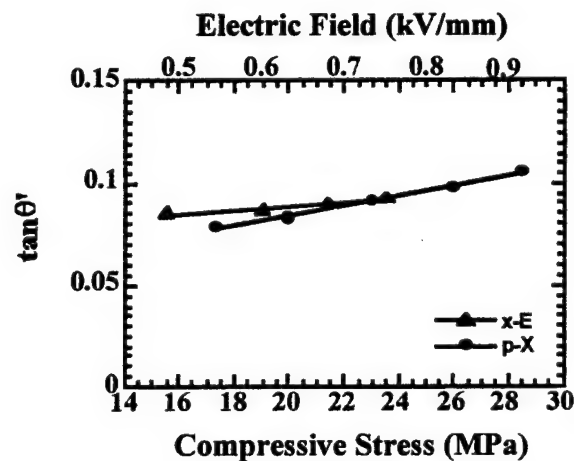

Fig.4 Extrinsic piezoelectric dissipation factor $\tan\theta'$ as a function of electric field or compressive stress, measured for a PZT based actuator.
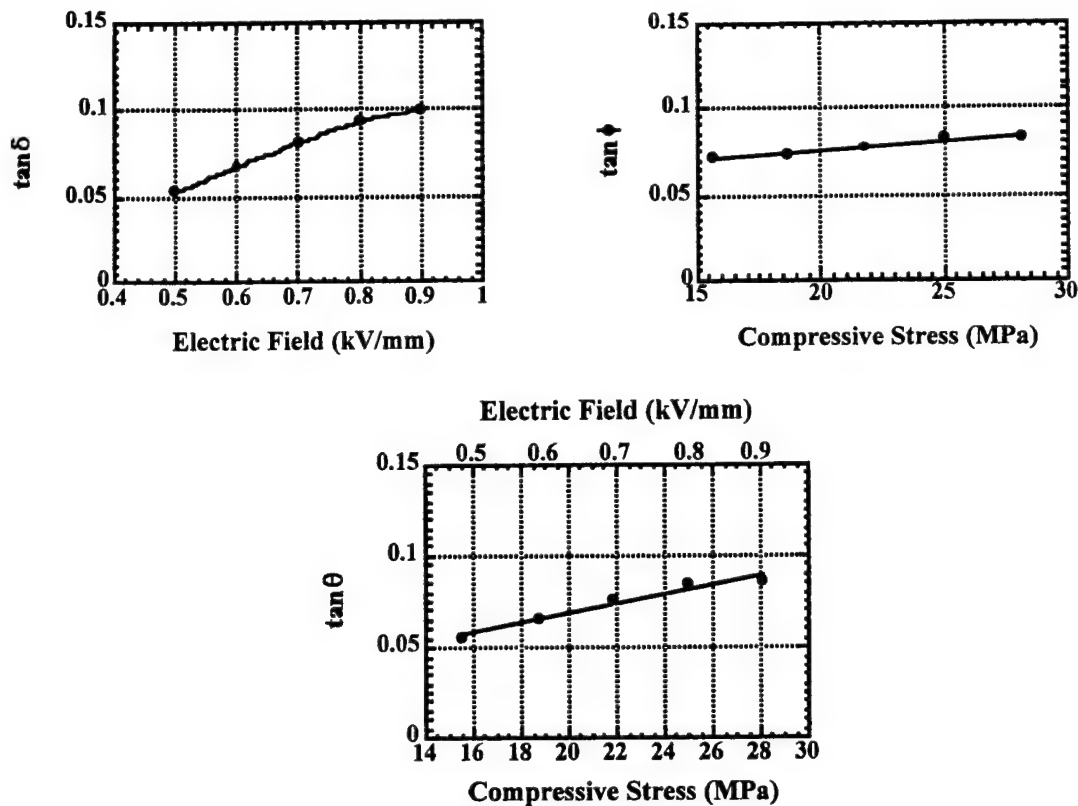
Fig.5 Intrinsic loss factors, $\tan\delta$, $\tan\phi$, and $\tan\theta$ as a function of electric field or compressive stress, measured for a PZT based actuator.

CONCLUSIONS

Theoretical and experimental techniques for measuring the extrinsic and intrinsic electric, mechanical and piezoelectric coupling losses separately have been discussed. We found that the piezoelectric loss is not so small as believed by the previous researchers.

REFERENCES

1. K. Uchino, J. Zheng, A. Joshi, Y. H. Chen, S. Yoshikawa, S. Hirose, S. Takahashi and J. W. C. de Vries, J. Electroceramics, **2**, 33-40 (1998).
2. S. Takahashi and S. Hirose, Jpn. J. Appl. Phys., **32**, 2422-2425 (1993).
3. S. Hirose, M. Aoyagi, Y. Tomikawa, S. Takahashi and K. Uchino, Proc. Ultrasonics Int'l '95, Edinburgh, pp. 184-87 (1995).
4. K. H. Haerdtl, Ceram. Int'l., **8**, 121-127 (1982).
5. P. Gerthsen, K. H. Haerdtl and N. A. Schmidt, J. Appl. Phys. **51**, 1131-1134 (1980).
6. J. Zheng, S. Takahashi, S. Yoshikawa, K. Uchino and J. W. C. de Vries, J. Amer. Ceram. Soc., **79**, 3193-98 (1996).
7. T. Ikeda, Fundamentals of Piezoelectric Materials Science, (Ohm Publication Company, Tokyo, 1984), pp. 83.

APPENDIX 69

LOSS MECHANISMS IN PIEZOELECTRICS

- How to Measure Different Losses Separately -

Kenji Uchino,[*] Member, IEEE, and Seiji Hirose[**], Member, IEEE

ABSTRACT

Losses in piezoelectrics are considered in general to have three different mechanisms; dielectric, mechanical and piezoelectric losses. This paper deals with the phenomenology of losses, first, then how to measure these losses separately in experiments. We found that heat generation at off-resonance is caused mainly by dielectric loss tan δ' (i. e. P-E hysteresis loss), not by mechanical loss, and that a significant decrease in mechanical Q_m with an increase of vibration level was observed in resonant piezoelectric ceramic devices, which is due to an increase in the intrinsic dielectric loss, not in the intrinsic mechanical loss. Finally, we propose the usage of the antiresonance mode rather than the conventional resonance mode, particularly for high power applications, since the mechanical quality factor Q_B at an antiresonance frequency is larger than Q_A at a resonance frequency.

---

*, **) Kenji Uchino is with the International Center for Actuators and Transducers, Materials Research Laboratory, The Pennsylvania State University, University Park, Pa 16802, and Seiji Hirose is with Faculty of Engineering, Yamagata University, Yonezawa 992, Japan.

INTRODUCTION

Loss or hysteresis in piezoelectrics exhibits both merits and demerits. For positioning actuator applications, hysteresis in the field-induced strain provides a serious problem, and for resonance actuation such as ultrasonic motors, loss generates significant heat in the piezoelectric materials. Further, in consideration of the resonant strain amplified in proportion to a mechanical quality factor, low (extrinsic) mechanical loss materials are preferred for ultrasonic motors. On the contrary, for force sensors and acoustic transducers, a low mechanical quality factor Q_m (which corresponds to high mechanical loss) is essential to widen a frequency range for receiving signals.

K. H. Haerdtl wrote a review article on electrical and mechanical losses in ferroelectric ceramics.[1] Losses are considered to consist of four portions: (1) domain wall motion, (2) fundamental lattice portion, which should also occur in domain-free monocrystals, (3) microstructure portion, which occurs typically in polycrystalline samples, and (4) conductivity portion in highly-ohmic samples. However, in the typical piezoelectric ceramic case, the loss due to the domain wall motion exceeds the other three contributions significantly. They reported interesting experimental results on the relationship between electrical and mechanical losses in piezoceramics, $Pb_{0.9}La_{0.1}(Zr_{0.5}Ti_{0.5})_{1-x}Me_xO_3$, where Me represents the doped ions Mn, Fe or Al and x varied between 0 and 0.09. However, they measured the mechanical losses on poled ceramic samples, while the electrical losses on unpoled samples, i.e., in a different polarization state. Thus, they completely neglected piezoelectric losses.

As far as the authors' knowledge, not much research effort has been put into systematic studies of the loss mechanisms in piezoelectrics, particularly in high voltage and high power ranges. Since not many comprehensive descriptions can be found in previous

reports, this paper will clarify the loss mechanisms in piezoelectrics phenomenologically, describe heat generation processes and high power characteristics, and finally, discuss the resonance and antiresonance vibration modes from a viewpoint of a quality factor.

Although T. Ikeda described part of the formulas of this paper in his textbook,[2] he totally neglected the piezoelectric losses, which have been found not to be neglected in our investigtions. We derive the full descriptions of the all losses in this paper.

LOSS AND HYSTERESIS IN THE POLARIZATION CURVE

Relation between Hysteresis and Dissipation Factor

Let us start first with loss and hysteresis in the electric displacement D (nearly equal to polarization P) vs. electric field E curve without considering the electromechanical coupling. Figure 1(a) shows an example P-E hysteresis curve. When the D (or P) traces a different line with increased and decreased applied electric field E, it is called *hysteresis*.

When the hysteresis is not very large, the electric displacement D can be expressed by using a slight phase lag to the applied electric field. Assuming that the electric field oscillates at a frequency f $(= \omega/2\pi)$ as

$$E^* = E_0 e^{j\omega t}, \tag{1}$$

the induced electric displacement oscillates also at the same frequency under the steady state, but with some time phase delay δ':

$$D^* = D_0 e^{j(\omega t - \delta')}. \tag{2}$$

If we express the relation between D^* and E^* as

$$D^* = \varepsilon^* \varepsilon_0 E^*, \tag{3}$$

3

where the complex dielectric constant ε^* is

$$\varepsilon^* = \varepsilon' - j\,\varepsilon'', \tag{4}$$

and where

$$\varepsilon''/\varepsilon' = \tan\delta'. \tag{5}$$

Note that the negative connection in Eq.(4) comes from the time "delay", and that $\varepsilon'\varepsilon_0 = (D_0/E_0)\cos\delta'$ and $\varepsilon''\varepsilon_0 = (D_0/E_0)\sin\delta'$.

The area w_e corresponds to the consumed loss energy during an electric field cycle per unit volume of the dielectrics, and can be related in isotropic dielectrics with ε'' or $\tan\delta'$ as follows:

$$w_e = -\int D\,dE = -\int_0^{2\pi/\omega} D\,(dE/dt)\,dt = \pi\,E_0\,D_0\sin\delta'$$

$$= \pi\,\varepsilon''\varepsilon_0\,E_0^2 = \pi\,\varepsilon'\varepsilon_0\,E_0^2\tan\delta' \tag{6}$$

When there is no phase delay ($\delta' = 0$), $w_e = 0$; i. e. the electrostatic energy stored in the dielectric will be recovered completely after a full cycle (100% efficiency). However, when there is a phase delay, the loss w_e will be accompanied per cycle, and the dielectric material generates heat. The $\tan\delta'$ is called *dielectric dissipation factor*.

In consideration of the stored electrostatic energy during a half cycle from $-E_0$ to E_0 [$= 4\,U_e$, which is illustrated as an area in Fig. 1(a)] provided by

$$4\,U_e = (1/2)(2\,E_0)(2\,\varepsilon'\varepsilon_0\,E_0) = 2\,\varepsilon'\varepsilon_0\,E_0^2, \tag{7}$$

the dissipation factor $\tan\delta'$ can be experimentally obtained by

4

$$\tan \delta' = (1/2\pi)(w_e / U_e). \tag{8}$$

Note that w_e is the hysteresis in a full cycle and U_e is the stored energy in a quarter of cycle.

Temperature, Electric Field and Frequency Dependence of P-E Hysteresis

Figures 2, 3 and 4 show temperature, electric field and frequency dependence of the dissipation factor $\tan \delta'$ calculated from the *P-E* hysteresis loss measured under stress free condition for a PZT-based ceramic. Refer to our paper[3] for the experimental details. The loss $\tan \delta'$ decreases gradually with increasing temperature, but is rather insensitive to frequency. On the contrary, the $\tan \delta'$ increases initially in proportion to the applied electric field, exhibiting a saturation above a certain electric field. After reaching the saturation, this complex physical quantity treatment should not be employed. The value for $E = 0$ (solid triangle mark in the figure) was obtained with an impedance analyzer.

GENERAL CONSIDERATION OF LOSS AND HYSTERESIS

Theoretical Formulas

Let us expand the above discussion into more general cases; i.e., piezoelectric materials. We will start from the Gibbs free energy G expressed by

$$dG = -x \, dX - D \, dE - S \, dT, \tag{9}$$

or

$$G = -(1/2) s^E X^2 - d X E - (1/2) \varepsilon^X \varepsilon_0 E^2. \tag{10}$$

Here, x is strain, X, stress, D, electric displacement, E, electric field, S, enthalpy and T is temperature. Equation (10) is the energy expression in terms of intensive (i.e., externally

controllable) physical parameters X and E. Temperature dependence is carried into the elastic compliance s^E, the dielectric constant ε^X and the piezoelectric constant d. We will obtain the following two piezoelectric equations:

$$x = - (\partial G/\partial X) = s^E X + d\, E,\tag{11}$$

$$D = - (\partial G/\partial E) = d\, X + \varepsilon^X \varepsilon_0\, E.\tag{12}$$

Note that thermodynamical equations and the consequent piezoelectric equations [Eqs. (9)-(12)] cannot yield a delay-time related loss, without taking into account irreversible thermodynamic equations or dissipation functions, in general. However, the latter considerations are mathematically equivalent to the introduction of complex physical constants into the phenomenological equations, if the loss can be treated as a perturbation.

Therefore, we will introduce complex parameters ε^{X*}, s^{E*} and d^* in order to consider the hysteresis losses in dielectric, elastic and piezoelectric coupling energy :

$$\varepsilon^{X*} = \varepsilon^X(1 - j \tan \delta'),\tag{13}$$

$$s^{E*} = s^E(1 - j \tan \phi'),\tag{14}$$

$$d^* = d(1 - j \tan \theta').\tag{15}$$

θ' is the phase delay of the strain under an applied electric field, or the phase delay of the electric displacement under an applied stress. Both delay phases should be exactly the same if we introduce the same complex piezoelectric constant d^* into Eqs.(11) and (12). δ' is the phase delay of the electric displacement to an applied electric field under a constant stress (e.g., zero stress) condition, and ϕ' is the phase delay of the strain to an applied stress under a constant electric field (e.g., short-circuit) condition. We will consider these phase delays as "extrinsic" losses.

6

Figures 1(a) - 1(d) correspond to the model hysteresis curves for practical experiments: D vs. E curve under a stress-free condition, x vs. X under a short-circuit condition, x vs. E under a stress-free condition and D vs. X under an open-circuit condition for measuring charge (or under a short-circuit condition for measuring current), respectively. Notice that these measurements are easily conducted in practice.

In a similar fashion to the previous section, the stored energies and hysteresis losses for pure dielectric and elastic energies can be calculated as:

$$U_e = (1/2) \, \varepsilon^X \varepsilon_0 \, E_0^2, \tag{16}$$

$$w_e = \pi \, \varepsilon^X \varepsilon_0 \, E_0^2 \tan \delta', \tag{17}$$

$$U_m = (1/2) \, s^E X_0^2, \tag{18}$$

$$w_m = \pi \, s^E X_0^2 \tan \phi'. \tag{19}$$

The electromechanical loss, when measuring the induced strain under an electric field, is more complicated. Let us calculate the stored energy U_{em} during a quarter electric field cycle (i.e., 0 to E_0), first :

$$U_{em} = -\int x \, dX = (1/2) \, (x_0^2/s^E) = (1/2) \, (dE_0)^2/s^E$$

$$= (1/2) \, (d^2/s^E) E_0^2. \tag{20}$$

Replacing d and s^E by $d^* = d(1 - j \tan \theta')$ and $s^{E*} = s^E(1 - j \tan \phi')$, we obtain

$$U_{em} = (1/2) \, (d^2/s^E) \, E_0^2, \tag{21}$$

and

$$w_{em} = \pi \, (d^2/s^E) \, E_0^2 \, (2 \tan \theta' - \tan \phi'). \tag{22}$$

Note that the strain vs. electric field measurement seems to provide the piezoelectric loss $\tan\theta'$ directly, however, the observed loss should include an additional elastic loss because the strain should be delayed to the initial stress, which is needed to calculate energy.

Similarly, when we measure the induced charge under stress, the stored energy U_{me} and the hysteresis loss w_{me} during a quarter and a full stress cycle, respectively, are obtained as

$$U_{me} = (1/2)\,(d^2/\,\varepsilon_0\varepsilon^X)\,X_0^{\,2}, \tag{23}$$

and

$$w_{me} = \pi\,(d^2/\,\varepsilon_0\varepsilon^X)\,X_0^{\,2}\,(2\tan\theta' - \tan\delta'). \tag{24}$$

Hence, from the measurements of D vs. E and x vs. X, we obtain $\tan\delta'$ and $\tan\phi'$, respectively, and either the piezoelectric (D vs. X) or converse piezoelectric measurement (x vs. E) provides $\tan\theta'$ through a numerical subtraction.

So far, we discussed the "extrinsic" dielectric, mechanical and piezoelectric losses. In order to consider real physical meanings of the losses, we will introduce the "intrinsic" losses.[2] When we start from the energy expression in terms of extensive (material's own) physical parameters x and D, that is,

$$dA = X\,dx + E\,dD - S\,dT, \tag{25}$$

we can obtain the piezoelectric equations as follows:

$$X = (\partial A/\partial x) = c^D\,x - h\,D, \tag{26}$$

$$E = (\partial A/\partial D) = -h\,x + \kappa^x\kappa_0\,D. \tag{27}$$

We introduce the intrinsic dielectric, elastic and piezoelectric losses as

$$\kappa^{x*} = \kappa^x\,(1 + j\tan\delta), \tag{28}$$

$$c^{D*} = c^D (1 + j \tan \phi), \tag{29}$$

$$h^* = h (1 + j \tan \theta). \tag{30}$$

It is notable that the permittivity under a constant strain (e.g., zero strain or completely clamped) condition, ε^{x*} and the elastic compiance under a constant electric displacement (e.g., open-circuit) condition, s^{D*} can be provided as an inverse value of κ^{x*} and c^{D*}, respectively. Thus, using the exactly the same losses in Eqs. (28) and (29),

$$\varepsilon^{x*} = \varepsilon^x (1 - j \tan \delta), \tag{31}$$

$$s^{D*} = s^D (1 - j \tan \phi), \tag{32}$$

We will consider these phase delays again as "intrinsic" losses.

Here, we consider the physical property difference between the boundary conditions; E constant and D constant, or X constant and x constant. When an elecric field is applied on a piezoelectric sample as illustrated in the top of Fig. 5, this state will be equivalent to the superposition of the following two steps: first, the sample is completely clamped and the field E_0 is applied (pure electrical energy $(1/2)\, \varepsilon^x \varepsilon_0\, E_0^2$ is input); second, keeping the field at E_0, the mechanical constraint is released (additional mechanical energy $(1/2)\, (d^2/s^E)\, E_0^2$ is necessary). The total energy should correspond to the total input electrical energy $(1/2)\, \varepsilon^X \varepsilon_0\, E_0^2$; thus, we obtain the relation,

$$\varepsilon_0 \varepsilon^X = \varepsilon_0 \varepsilon^x + (d^2/s^E), \tag{33}$$

Similarly, from the bottom of Fig. 5,

$$s^E = s^D + (d^2/\varepsilon_0 \varepsilon^X). \tag{34}$$

Hence, we obtain the following equations:

$$\varepsilon^x / \varepsilon^X = (1 - k^2), \tag{35}$$

9

$$s^D/s^E = (1 - k^2),\tag{36}$$

where

$$k^2 = d^2/(s^E \varepsilon_0 \varepsilon^X).\tag{37}$$

Similarly,

$$\kappa^X/\kappa^x = (1 - k^2),\tag{38}$$

$$c^E/c^D = (1 - k^2),\tag{39}$$

where

$$k^2 = h^2/(c^D \kappa^x \kappa_0).\tag{40}$$

This k is called the *electromechanical coupling factor*, and is the same as the k in Eq. (37), because the equation $d^2/(s^E \varepsilon_0 \varepsilon^X) = h^2/(c^D \kappa^x \kappa_0)$ can be verified mathematically. We define the k as a real number in this manuscript.

In order to obtain the relationships between the extrinsic and intrinsic losses, the following three equations are essential:

$$\varepsilon_0 \varepsilon^X = [\kappa^x \kappa_0 (1 - h^2/(c^D \kappa^x \kappa_0))]^{-1},\tag{41}$$

$$s^E = [c^D (1 - h^2/(c^D \kappa^x \kappa_0))]^{-1},\tag{42}$$

$$d = [h^2/(c^D \kappa^x \kappa_0)] [h (1 - h^2/(c^D \kappa^x \kappa_0))]^{-1}.\tag{43}$$

Replacing the parameters in Eqs. (41) - (43) by the complex parameters in Eqs. (13) - (15), (28) - (30), we obtain the relationships between the extrinsic and intrinsic losses:

$$\tan \delta' = (1/(1 - k^2))[\tan \delta + k^2(\tan \phi - 2 \tan \theta)],\tag{44}$$

$$\tan \phi' = (1/(1 - k^2))[\tan \phi + k^2(\tan \delta - 2 \tan \theta)],\tag{45}$$

$$\tan \theta' = (1/(1 - k^2))[\tan \delta + \tan \phi + (1 + k^2) \tan \theta],\tag{46}$$

where k is the electromechanical coupling factor defined by either Eq. (37) or Eq. (40), and here as a real number. It is important that the extrinsic dielectric and elastic losses are

mutually correlated with the intrinsic dielectric, elastic and piezoelectric losses through the electromechanical coupling k^2, and that the denominator $(1 - k^2)$ comes basically from the ratios, $\varepsilon^x/\varepsilon^X = (1 - k^2)$ and $s^D/s^E = (1 - k^2)$, and this real part reflects to the dissipation factor when the imaginary part is devided by the real part. Also note that depending on the vibration mode, the definition of electromechanical coupling k can be changed such as $k^2 = d^2/(s^D \varepsilon_0 \varepsilon^X)$.

Experimental Example

Figure 6 shows "extrinsic" dissipation factors determined from (a) D vs. E (stress free), (b) x vs. X (short-circuit), (c) x vs. E (stress free) and (d) D vs. X (open-circuit) curves for a soft PZT based multilayer actuator used for Figs. 2, 3 and 4. The details on the experiments will be reported in the successive papers. Figure 7 shows the result for the piezoelectric loss $\tan\theta'$. We used the correlation factor between electric field and compressive stress given averagely by $X = (\varepsilon_0\varepsilon^X/s^E)^{1/2} E$.

From Figs. 6 and 7, we can calculate the "intrinsic" losses as shown in Fig. 8. Note that the piezoelectric losses $\tan\theta'$ and $\tan\theta$ are not so small as previously believed, but comparable to the dielectric and elastic losses, and increase gradually with the field or stress. Also it is noteworthy that the intrinsic dielectric loss $\tan\delta$ increases significantly with an increase of the intensive parameter, i.e., the applied electric field, while the intrinsic elastic loss $\tan\phi$ is rather insensitive to the intensive parameter, i.e., the applied compressive stress.

When similar measurements to Figs. 1(a) and 1(b), but under constrained conditions; that is, D vs. E under a completely clamped state, and x vs. X under an open-circuit state, respectively, we can expect smaller hystereses; that is, intrinsic losses, $\tan\delta$ and $\tan\phi$. These measurements seem to be alternative methods to determine the three losses separately, however, they are rather difficult in practice.

LOSS AND HEAT GENERATION

Heat generation in various types of PZT-based actuators has been studied under a relatively large electric field applied (1 kV/mm or more) at an off-resonance frequency, and a simple analytical method was established to evaluate the temperature rise, which is very useful for the design of piezoelectric high-power actuators. Heat generation in a resonating piezoelectric sample is discussed in the following Section.

Zheng et al. reported the heat generation from various sizes of multilayer type piezoelectric ceramic actuators.[3] Figure 9 shows the temperature change with time in the actuators when driven at 3 kV/mm and 300 Hz, and Fig. 10 plots the saturated temperature as a function of V_e/A, where V_e is the effective volume (electrode overlapped part) and A is the surface area. This linear relation is reasonable because the volume V_e generates the heat and this heat is dissipated through the area A. Thus, if we need to suppress the temperature rise, a small V_e/A design is preferred.

According to the law of energy conservation, the rate of heat storage in the piezoelectric resulting from heat generation and dissipation effects can be expressed as

$$q_g - q_{out} = V \rho c (dT/dt), \qquad (47)$$

assuming uniform temperature distribution in the sample. V, ρ, c are total volume, density and specific heat, respectively. The heat generation is considered to be caused by losses. Thus, the rate of heat generation (q_g) in the piezoelectric can be expressed as

$$q_g = u f V_e, \qquad (48)$$

where u is the loss of the sample per driving cycle per unit volume, f, the driving frequency, and V_e is the effective volume where the ceramic is activated. According to the measuring condition, this u corresponds to the extrinsic dielectric loss w_e of Eq. (17), which consists

12

of the intrinsic dielectric loss tan δ and the electromechanical and piezoelectric combined loss (tanϕ - 2 tanθ) in the previous section:

$$u = w_e = \pi \, \varepsilon^x \varepsilon_0 \, E_0^2 \tan \delta'$$

$$= [1/(1 - k^2)][\tan \delta + k^2(\tan \phi - 2 \tan \theta)] \, \pi \, \varepsilon^x \varepsilon_0 \, E_0^2. \tag{49}$$

Note that we do not need to add w_{em} explicitly, because the corresponding electromechanical loss is already included implicitly in w_e.

When we neglect the conduction heat transfer, the rate of heat dissipation (q_{out}) from the sample is the sum of the rates of heat flow by radiation (q_r) and convection (q_c):

$$q_{out} = q_r + q_c$$

$$= \sigma e A(T^4 - T_0^4) + h_c \, A(T - T_0), \tag{50}$$

where σ is the Stehan-Boltzmann constant, e is the emissivity of the sample, h_c is the average convective heat transfer coefficient, and A is the sample surface area.

Thus, Eq.(47) can be written in the form:

$$u \, f \, V - A \, k(T) \, (T - T_0) = V \, \rho \, c \, (dT/dt), \tag{51}$$

where

$$k(T) = \sigma e(T^2 + T_0^2)(T + T_0) + h_c \tag{52}$$

is defined as the overall heat transfer coefficient. If we assume that $k(T)$ is relatively insensitive to temperature change, the solution to Eq.(51) for the piezoelectric sample temperature is given as a function of time (t):

$$T - T_0 = [u \, f \, V_e / \, k(T) \, A] \, [1 - e^{-t/\tau}], \tag{53}$$

13

where the time constant τ is expressed as

$$\tau = \rho c V / k(T) A. \tag{54}$$

As $t \rightarrow \infty$, the maximum temperature rise in the sample becomes

$$\Delta T = u\, f\, V_e / k(T)\, A. \tag{55}$$

As $t \rightarrow 0$, the initial rate of temperature rise is

$$(dT/dt) = u\, f\, V_e / \rho\, c\, V = \Delta T / \tau. \tag{56}$$

Figures 11 and 12 show the dependence of $k(T)$ on applied electric field and frequency. Since $k(T)$ is not really constant, we can calculate the total loss u of the piezoelectric more precisely through Eq.(56). The calculated results are shown in Table I. The experimental data of P-E hysteresis losses under a stress-free condition are also listed for comparison. It is seen that the P-E hysteresis extrinsic loss agrees well with the total loss contributing to the heat generation under an off-resonance drive.

LOSSES AT A PIEZOELECTRIC RESONANCE

So far, we have considered the losses for a quasi-static or off-resonance state. Problems in ultrasonic motors which are driven at the resonance frequency include significant distortion of the admittance frequency spectrum due to nonlinear behavior of elastic compliance at a high vibration amplitude, and heat generation which causes a serious degradation of the motor characteristics through depoling of the piezoceramic. Therefore, the ultrasonic motor requires a very hard type piezoelectric with a high mechanical quality factor Q_m, leading to the suppression of heat generation. It is also notable that the actual mechanical vibration amplitude at the resonance frequency is directly proportional to this Q_m value.

14

Losses at a Piezoelectric Resonance

Piezoelectric resonance without loss

Let us review first the longitudinal mechanical vibration of a piezo-ceramic plate without loss through the transverse piezoelectric effect (d_{31}) as shown in Fig. 13.[4] Assuming that the polarization is in the z-direction and the x-y planes are the planes of the electrodes, the extentional vibration in the x direction is represented by the following dynamic equation:

$$(\partial^2 u/\partial t^2) = F = (\partial X_{11}/\partial x) + (\partial X_{12}/\partial y) + (\partial X_{13}/\partial z), \tag{57}$$

where u is the displacement of the small volume element in the ceramic plate in the x-direction. When the plate is very long and thin, X_2 and X_3 may be set equal to zero through the plate, and the relations between stress, electric field (only E_Z exists) and the induced strain are given by :

$$X_1 = x_1/s_{11}{}^E - (d_{31}/s_{11}{}^E)E_Z. \tag{58}$$

Introducing Eq.(58) into Eq.(57), and allowing for $x_1 = \partial u/\partial x$ and $\partial E_Z/\partial x = 0$ (due to the equal potential on each electrode), leads to a harmonic vibration equation :

$$-\omega^2 \rho\, s_{11}{}^E\, u = \partial^2 u/\partial x^2. \tag{59}$$

Here, ω is the angular frequency of the drive field, and ρ is the density. Substituting a general solution $u = u_1(x)e^{j\omega t} + u_2(x)e^{-j\omega t}$ into Eq.(58), and with the boundary condition $X_1 = 0$ at $x = 0$ and L (sample length), the following solutions can be obtained:

(strain) $\partial u/\partial x = x_1 = d_{31} E_Z [\sin\omega(L-x)/v + \sin(\omega x/v)]/\sin(\omega L/v), \tag{60}$

(total displacement) $\Delta L = \int_0^L x_1 dx = d_{31} E_Z L\,(2v/\omega L)\,\tan(\omega L/2v). \tag{61}$

15

Here, v is the sound velocity in the piezoceramic which is given by

$$v = 1 / \sqrt{\rho s_{11}^{E}} . \tag{62}$$

Since the total current is given by :

$$i = j\omega w \int_{0}^{L} D_{3}\, dx = j\omega w \int_{0}^{L} [(\varepsilon_0 \varepsilon_3^{X} - d_{31}^{2}/s_{11}^{E})E_Z + (d_{31}/s_{11}^{E})x_1]\, dx, \tag{63}$$

and using Eq. (60), the admittance for the mechanically free sample is calculated to be:

$$Y = (1/Z) = (i/V) = (i/E_Z t)$$

$$= (j\omega w L/t)\, \varepsilon_0 \varepsilon_3^{LC}[1 + (d_{31}^{2}/\varepsilon_0 \varepsilon_3^{LC} s_{11}^{E})(\tan(\omega L/2v) / (\omega L/2v)], \tag{64}$$

where w is the width, L the length, t the thickness of the sample, and V the applied voltage. ε_3^{LC} is the permittivity in a longitudinally clamped sample, which is given by

$$\varepsilon_0 \varepsilon_3^{LC} = \varepsilon_0 \varepsilon_3^{X} - (d_{31}^{2}/s_{11}^{E}) = \varepsilon_0 \varepsilon_3^{X}(1 - k_{31}^{2}) . \tag{65}$$

The final transformation is provided by the definition,

$$k_{31} = d_{31} / \sqrt{s_{11}^{E} \varepsilon_0 \varepsilon_3^{X}} . \tag{66}$$

When the drive frequency is much lower than the resonance, taking $\omega \to 0$ in Eq. (64) leads to $Y = (j\omega w L/t)\, \varepsilon_3^{X}$ (corresponding to the static capacitance). The piezoelectric resonance is achieved where the admittance becomes infinite or the impedance is zero. The resonance frequency f_R is calculated from Eq. (64), and the fundamental f_R is given by

$$f_R = v/2L = 1/(2L \sqrt{\rho s_{11}^{E}}). \tag{67}$$

16

On the other hand, the antiresonance state is generated for zero admittance or infinite impedance:

$$(\omega_A L/2v) \cot (\omega_A L/2v) = - d_{31}^2 / \varepsilon_3^{LC} s_{11}^E = - k_{31}^2 / (1 - k_{31}^2).$$ (68)

The resonance and antiresonance states are described by the following intuitive model.[4] In a high electromechanical coupling material with k almost equal to 1, the resonance or antiresonance states appear for $\tan(\omega L/2v) = \infty$ or 0 [i. e., $\omega L/2v = (m-1/2)\pi$ or $m\pi$ (m: integer)], respectively. The strain amplitude x_1 distribution for each state [calculated using Eq. (60)] is illustrated in Fig. 14. In the resonance state, large strain amplitudes and large capacitance changes (called *motional capacitance*) are induced, and the current can easily flow into the device. Note that for a loss-free piezoelectric the strain is calculated to be infinite in Eq. (60). On the other hand, at the antiresonance, the strain induced in the device compensates completely, resulting in no capacitance change, and the current cannot flow easily into the sample. Both ends of the plate correspond to the nodal points, which do not generate any motion to be used for actuators. Thus, for a high k material the first antiresonance frequency f_A should be twice as large as the first resonance frequency f_R.

In a typical case, where k_{31} = 0.3, the antiresonance state varies from the above-mentioned mode and becomes closer to the resonance mode. The low-coupling material exhibits an antiresonance mode where capacitance change due to the size change is compensated completely by the current required to charge up the static capacitance (called *damped capacitance*). Thus, the antiresonance frequency f_A will approach the resonance f_R.

When $(f_A - f_R)$ is not very large due to a small electromechanical coupling, we can derive the following approximate expression for f_A. Assuming that $\omega_A - \omega_R$ is much smaller than ω_R (= $\pi v /L$), and

$$(\omega_A L/2v) \cot [(\omega_A - \omega_R)L/2v - \pi/2)] = - k_{31}^2/(1 - k_{31}^2). \qquad (69)$$

Thus,

$$\omega_A = (\pi v/L)[1 + (4/\pi^2) K_{31}^2], \qquad (70)$$

where we introduced a new parameter K_{31} as

$$K_{31}^2 = k_{31}^2/(1 - k_{31}^2). \qquad (71)$$

It is notable that for a piezoelectric sample with a typical k_{31} value, the two ends of the plate are not the nodal points; that is, we can expect rather large displacements, which can be applied for ultrasonic motors.

Piezoelectric resonance with losses

Now, we will introduce the complex parameters into the admittance curve around the resonance frequency, in a similar way to the previous section: $\varepsilon_3^{X*} = \varepsilon_3^X (1 - j \tan \delta')$, $s_{11}^{E*} = s_{11}^E (1 - j \tan \phi')$, and $d_{31}^* = d(1 - j \tan \theta')$ into Eq. (64):

$$Y = Y_d + Y_m$$

$$= (j\omega wL/t)\varepsilon_0\varepsilon_3^X (1 - k_{31}^2)[1 - j (1/(1-k_{31}^2))((\tan \delta' + k_{31}^2(\tan \phi' - 2 \tan \theta'))]$$

$$+ (j\omega wL/t)\varepsilon_0\varepsilon_3^X k_{31}^2 [(1 - j(2 \tan \theta' - \tan \phi')][(\tan(\omega L/2 v^*) / (\omega L/2v^*)]$$

$$= j\omega C_0 (1 - k_{31}^2) [1 - j (1/(1-k_{31}^2))((\tan \delta' + k_{31}^2(\tan \phi' - 2 \tan \theta'))]$$

$$+ j\omega C_0 k_{31}^2[(1-j(2\tan\theta' - \tan \phi')][(\tan(\omega L/2v^*)/(\omega L/2v^*)]$$

$$= j\omega C_d (1 - j \tan \delta) + j\omega C_d K_{31}^2[(1-j(2\tan\theta' - \tan \phi')][(\tan(\omega L/2v^*)/(\omega L/2v^*)], \quad (72)$$

where

18

$$C_0 = (wL/t) \, \varepsilon_0 \varepsilon_3^X, \tag{73}$$

$$C_d = (1 - k_{31}^2) \, C_0 . \tag{74}$$

Note that the loss for the first term (damped conductance) is represented by the "intrinsic" dielectric loss tan δ, not by the extrinsic loss tan δ'. Taking into account

$$v^* = 1/\sqrt{\rho \, s_{11}^E (1 - j \tan \phi')} = v \, (1 + (1/2) \, j \tan \phi'), \tag{75}$$

we further calculate $1/(\tan(\omega L/2v^*)$ with an expansion-series approximation around $(\omega L/2v) = \pi/2$. The resonance state is defined in this case for the maximum admittance point, rather than the infinite Y.

We will use new frequency paremeters,

$$\Omega = \omega L/2 \, v, \, \Delta\Omega = \Omega - \pi/2 \, (<<1) . \tag{76}$$

Since $\omega L/2 \, v^* = (\pi/2 + \Delta\Omega) [1 - (1/2) \, j \tan \phi']$,

$$1 / (\tan(\omega L/2v^*) = - \Delta\Omega + j \, (\pi/4)\tan \phi' . \tag{77}$$

Thus, using $K_{31}^2 = k_{31}^2 / (1 - k_{31}^2)$, the motional admittance Y_m is approximated aound the first resonance frequency by

$$Y_m = j\omega C_d K_{31}^2 \, [(1-j(2\tan\theta'-\tan \phi')][(\tan(\omega L/2v^*)/(\omega L/2v^*)]$$

$$= j\omega_0 C_d K_{31}^2 \, [(1-j(2\tan\theta'-\tan \phi')]/[(-\Delta\Omega+j(\pi/4)\tan\phi')(\pi/2)(1-(1/2)j\tan\phi')]$$

$$= j(\pi^2/8) \, \omega_0 C_d K_{31}^2 \, [(1+j((3/2)\tan\phi'-2\tan\theta')]/[(- (4/\pi)\Delta\Omega+j\tan\phi'). \tag{78}$$

The maximum Y_m is obtained at $\Delta\Omega = 0$:

$$Y_m^{max} = (\pi^2/8) \, \omega_0 \, C_d \, K_{31}^2 \, (\tan \phi')^{-1}. \tag{79}$$

19

In order to obtain the mechanical quality factor, let us obtain $\Delta\Omega$ which provides $Y_m^{max}/\sqrt{2}$. Since $\Delta\Omega = (\pi/4)\tan\phi'$ is obtained,

$$Q_m = \Omega_0/2\Delta\Omega = (\pi/2)/2(\pi/4)\tan\phi' = (\tan\phi')^{-1}. \tag{80}$$

This verifies the ready-used relation, $Q_m = (\tan\phi')^{-1}$.

Here, the displacement amplification is also considered. From Eq. (61), also by using the complex parameters:

$$u(L) = d_{31}^* E_Z L \,(2v^*/\omega L)\tan(\omega L/2v^*)$$

$$= 2d_{31}(1-j\tan\theta')\,E_Z L\,[v(1+(1/2)j\tan\phi')/\omega L]\tan(\omega L/2\,v^*)$$

$$= 2d_{31}(1-j\tan\theta')\,E_Z L\,[v(1+(1/2)j\tan\phi')/\omega_0 L]/(-\Delta\Omega + j(\pi/4)\tan\phi'). \tag{81}$$

The maximum displacement u_{max} is obtained at $\Delta\Omega = 0$:

$$u_{max} = (\pi^2/8)\,d_{31}\,E_Z L\,(\tan\phi')^{-1}. \tag{82}$$

The maximum displacement at the resonance frequency is $(\pi^2/8)\,Q_m$ times larger than that at a non-resonance frequency $(d_{31}E_Z L)$.

In a brief summary, we obtained a ready-used knowledge: when we observe the admittance or dislpacement spectrum as a function of drive frequency, and obtain the mechanical quality factor Q_m estimated from $Q_m = \omega_0/2\Delta\omega$, where $2\Delta\omega$ is a full width of the 3 dB down (i.e., $1/\sqrt{2}$) of the maximum value at $\omega = \omega_0$, we can obtain the extrinsic mechanical loss $\tan\phi'$.

Equivalent Circuit

The equivalent circuit for the piezoelectric acuator is represented by a combination of L, C and R. Figure 15 (a) shows an equivalent circuit for the resonance state, which has

very low impedance. Taking into account Eq. (72), we can understand that C_d and R_d correspond to the electrostatic capacitance (for a longitudinally clamped sample in the previous case, not a free sample) and the clamped (or "intrinsic") dielectric loss tan δ, respectively, and the components L_A and C_A in a series resonance circuit are related to the piezoelectric motion. For example, in the case of the longitudinal vibration of the above rectangular plate through d_{31}, these components are represented approximately by

$$L_A = (\rho / 8)(Lb / w)(s_{11}^{E2} / d_{31}^{2}), \tag{83}$$

$$C_A = (8 / \pi^2)(Lw / b)(d_{31}^{2} / s_{11}^{E}). \tag{84}$$

The total resistance R_A $(= R_d + R_m)$ should corresponds to the loss tan ϕ', which is composed of the intrinsic mechanical loss tan ϕ and dielectric/piezoelectric coupled loss (tan δ - 2tan θ) (see Eq. (45)). Thus, roughly speaking, R_d and R_m correspond to the intrinsic dielectric and mechanical losses, respectively. Note that we introduced an additional resistance R_d to explain a large contribution of the dielectric loss when a vibration velocity is relatively large. In contrast, the equivalent circuit for the antiresonance state of the same actuator is shown in Fig. 15 (b), which has high impedance.

Losses as a Function of Vibration Velocity

Figure 16 shows the mechanical Q_m versus basic composition x at two effective vibration velocities v_0=0.05 m/s and 0.5 m/s for $Pb(Zr_xTi_{1-x})O_3$ doped with 2.1 at.% of Fe.[5] The decrease in mechanical Q_m with an increase of vibration level is minimum around the rhombohedral-tetragonal morphotropic phase boundary (52/48). In other words, the smallest Q_m material at a small vibration level becomes the best at a large vibration level, and the data obtained by a conventional impedance analyzer with a small voltage/power does not provide data relevant to high power materials.

21

Let us consider here the degradation mechanism of the mechanical quality factor Q_m with increasing vibration velocity. Figure 17 shows an important notion on heat generation from the piezoelectric material.[6] The damped and motional resistances, R_d and R_m, in the equivalent electrical circuit of a PZT sample are separately plotted as a function of vibration velocity. Note that R_m, mainly related to the intrinsic mechanical loss, is insensitive to the vibration velocity, while R_d, related to the intrinsic dielectric loss, increases significantly around a certain critical vibration velocity. Thus, the resonance loss at a small vibration velocity is mainly determined by the intrinsic mechanical loss which provides a high mechanical quality factor Q_m, and with increasing vibration velocity, the intrinsic dielectric loss contribution significantly increases. After R_d exceeds R_m, we started to observe heat generation.

S. Tashiro et. al observed the heat generation in a rectangular piezoelectric plate during a resonating drive.[7] Eventhough the maximum electric filed is not very large, heat is generated due to the large induced strain and stress at the resonance. The maximum heat generation was observed at the nodal point of the resonance vibration, where the maximum strain and stress are generated. This observation supports that the heat generation in a resonating sample is attributed to the "extrinsic" mechanical loss tan ϕ'. This is not contradictory to the result in Section 4, where a high-voltage drive was conducted at an off-resonance frequency. We concluded there that the heat is originated from the "extrinsic" dielectric loss tan δ'. In consideration that both the "extrinsic" dielectric and mechanical losses are composed of the "intrinsic" dielectric and mechanical losses, and that the intrinsic dielectric loss tan δ changes significantly with the external electric field and stress, the major contribution to the heat generation seems to come from the "intrinsic" dielectric loss. Further investigations are waited for the microscopic explanations of this phenomon.

LOSSES AT RESONANCE AND ANTIRESONANCE MODES

Losses at a Piezoelectric Antiresonance State

We consider here the losses at the antiresonance frequency in comparison with the resonance mode. The antiresonance mode is obtained at a frequency which provides the minimum value of admittance Y, instead of zero of Y for the loss-free case. Taking an approximation technique on Eq. (72) around the antiresonance frequency ω_A, similar to the previous section, we obtain:

$$\Omega_A = \omega_A L/2 \, v, \quad \Delta\Omega = \Omega - \Omega_A \; (\ll 1) . \tag{85}$$

If k_{31} is not very large, the following relationship is obtained:

$$\Omega_A = \omega_A L/ \, 2v = (\pi/2) \, (1 + (4/\pi^2) \, k_{31}^{\,2}) \quad . \tag{86}$$

In the following approximation, however, this relation is not used, but we will neglect the higher order of $\Delta\Omega$ and $\tan \phi'$ in Eq. (72):

$$Y = j\omega C_d \{1 + (k_{31}^{\,2}/(1-k_{31}^{\,2})) \tan[(\Omega_A +\Delta\Omega) \, (1- j \, (1/2) \tan\phi')]/$$
$$[(\Omega_A +\Delta\Omega) \, (1- j \, (1/2) \tan\phi')]. \tag{87}$$

Taking into account

$$\tan[(\Omega_A +\Delta\Omega) \, (1- j \, (1/2) \tan\phi')]$$

$$= [(\Omega_A^{\,2}-K_{31}^{\,2}\Delta\Omega+ j(1/2)\Omega_A \tan\phi' K_{31}^{\,2}]/[(-K_{31}^{\,2}- \Omega_A\Delta\Omega) -j\Omega_A(1/2)\Omega_A\tan\phi'], \tag{88}$$

$$Y = j\omega C_d \, [- (\Omega_A^{\,2}+K_{31}^{\,2}+K_{31}^{\,4})\Delta\Omega - j(1/2)\Omega_A \tan\phi' \, (\Omega_A^{\,2}-K_{31}^{\,2}-K_{31}^{\,4})/$$

$$[- K_{31}^{\,2}\Omega_A - (\Omega_A^{\,2}+K_{31}^{\,2})\Delta\Omega - j(1/2)\Omega_A \tan\phi' \, (\Omega_A^{\,2}- K_{31}^{\,2})], \tag{89}$$

where

$$K_{31}^2 = k_{31}^2/(1 - k_{31}^2) \tag{90}$$

Then, Y^{min} can be obtained at $\Delta\Omega = 0$:

$$Y^{min} = \omega C_d (1/2)\tan\phi' (\Omega_A^2 - K_{31}^2 - K_{31}^4)/K_{31}^2. \tag{91}$$

$\sqrt{2} Y^{min}$ can be obtained at

$$\Delta\Omega = (1/2) \Omega_A \tan\phi' (\Omega_A^2 - K_{31}^2 - K_{31}^4) /(\Omega_A^2 + K_{31}^2 + K_{31}^4). \tag{92}$$

Thus, mechanical quality factor at the antiresonance can be obtained as:

$$Q_m = \Omega_A /2\Delta\Omega = [(\Omega_A^2 + K_{31}^2 + K_{31}^4) /(\Omega_A^2 - K_{31}^2 - K_{31}^4)] (\tan\phi')^{-1}. \tag{93}$$

Since $(\Omega_A^2 + K_{31}^2 + K_{31}^4)/(\Omega_A^2 - K_{31}^2 - K_{31}^4)$ is larger than 1, Q_m can be verified to be larger than Q_m at the resonance (= $(\tan\phi')^{-1}$). When k_{31} is small, using Eq. (86) and neglecting k_{31}^4 or higer orders, Q_m is approximated as

$$Q_m = (1 + (8/\pi^2) k_{31}^2) (\tan\phi')^{-1}. \tag{94}$$

Note that this Q_m is equal to the inverse value of the intrinsic mechanical loss, $(\tan\phi)^{-1}$.

Experimental Results

Figure 18 illustrates mechanical quality factors, Q_A, Q_B and the temperature rise for the resonance (A-type) and the antiresonance (B-type) modes for a rectangular-shape har PZT resonator plotted as a function of vibration velocity.[6] The sample size is indicated in the figure (43 mm x 7 mm x 2 mm). Note that an "effective" vibration velocity v_0 is a material's constant independent of the sample size, and is defined as $\sqrt{2} \pi f u_{max}$ where f is the resonance or antiresonance frequency and u_{max} is the maximum vibration amplitude of the piezoelectric device.[8] It is again noteworthy that the mechanical quality factor decreases

significantly above a certain critical vibration velocity (0.1 m/s), where a steep tempreature rise starts. We have suggested that the heat generation is mainly attributed to the intrinsic dielectric loss rather than the mechanical loss. Note also that Q_B is higher than Q_A over the entire vibration velocity range, and that the temperature rise of the sample is less for the B-type resonance (antiresonance) than for the A-type resonance for the same vibration level. This indicates an intriguing idea that the antiresonance mode should be superior to the conventional resonance mode, particularly for high power applications such as ultrasonic motors. In a typical piezoelectric material with k_{31} around 30 %, the plate edge is not a vibration nodal point and can generate a large vibration velocity.

CONCLUSIONS

(1) Various techniques for measuring the electric, mechanical and piezoelectric coupling losses separately have been discussed:

   (a) D vs. E, x vs. X, x vs. E and D vs. X curves for dielectric, mechanical and piezoelectric losses

   (b) heat generation at a resonance or an off-resonance frequency for an extrinsic mechanical or dielectric loss

   (c) resonance/antiresonance technique for extrinsic and intrinsic mechanical losses, respectively

   By combining the above methods, we can investigate the loss mechanisms in practical piezoelectric materials.

(2) The piezoelectric losses $\tan\theta'$ and $\tan\theta$ are not so small as previously believed, but comparable to the dielectric and elastic losses in soft PZTs. Also it is noteworthy that the intrinsic dielectric loss $\tan\delta$ increases significantly with an increase of the intensive

25

parameter, i.e., the applied electric field, while the intrinsic elastic loss tanϕ is rather insensitive to the intensive parameter, i.e., the applied compressive stress.

(3) Heat generation is caused mainly by the extrinsic dielectric loss tan δ' (i.e., P-E hysteresis loss) for an off-resonance state under a high drive electric field, and by the extrinsic mechanical loss tan ϕ' for a resonance state. Both situations are attributed to the large "intrinsic dielectric loss" enhanced by a large external electric field or stress. In order to suppress the temperature rise practically, a transducer design with larger surface area is recommended (for example, a tube rather than a rod).

(4) A significant decrease in mechanical Q_m with an increase of vibration level was observed in resonant piezoelectric ceramic devices, and the data obtained by a conventional impedance analyzer with a small voltage/power do not provide data relevant to high power materials.

(5) Since the mechanical quality factor Q_B at an antiresonance frequency is larger than Q_A at a resonance frequency, the antiresonance mode seems to be superior to the conventional usage of the resonance mode, particularly for high power applications such as ultrasonic motors.

ACKNOWLEDGEMENT

REFERENCES

[1]K. H. Haerdtl, Ceram. Int'l., **8**, 121-127 (1982).

[2]T. Ikeda, Fundamentals of Piezoelectric Materials Science, (Ohm Publication Company, Tokyo, 1984), pp. 83.

[3]J. Zheng, S. Takahashi, S. Yoshikawa, K. Uchino and J. W. C. de Vries, J. Amer. Ceram. Soc., **79**, 3193-3198 (1996).

[4]K. Uchino, Piezoelectric Actuators and Ultrasonic Motors, (Kluwer Academic Publishers, Boston, 1997), pp. 197.

[5]S. Takahashi and S. Hirose, Jpn. J. Appl. Phys., **32**, 2422-2425 (1993).

[6]S. Hirose, M. Aoyagi, Y. Tomikawa, S. Takahashi and K. Uchino, Proc. Ultrasonics Int'l '95, Edinburgh, pp. 184-187 (1995).

[7]S. Tashiro, M. Ikehiro and H. Igarashi, Jpn. J. Appl. Phys., **36**, 3004-3009 (9197).

[8]K. Uchino, J. Zheng, A. Joshi, Y. H. Chen, S. Yoshikawa, S. Hirose, S. Takahashi and J. W. C. de Vries, J. Electroceramics, **2**, 33-40 (1998).

Table and Figure Captions

Table I Loss and overall heat transfer coefficient for PZT multilayer samples (E = 3 kV/mm, f = 300 Hz).
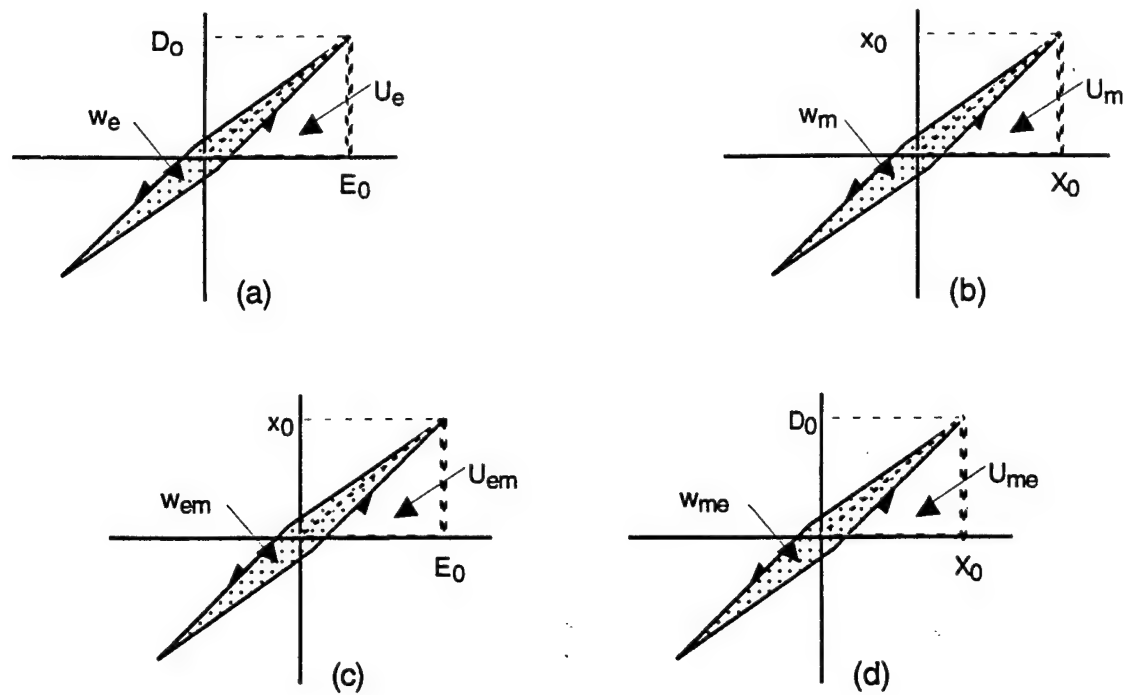
Fig.1 (a) D vs. E (stress free), (b) x vs. X (short-circuit), (c) x vs. E (stress free) and (d) D vs. X (open-circuit) curves with a slight hysteresis in each relation.
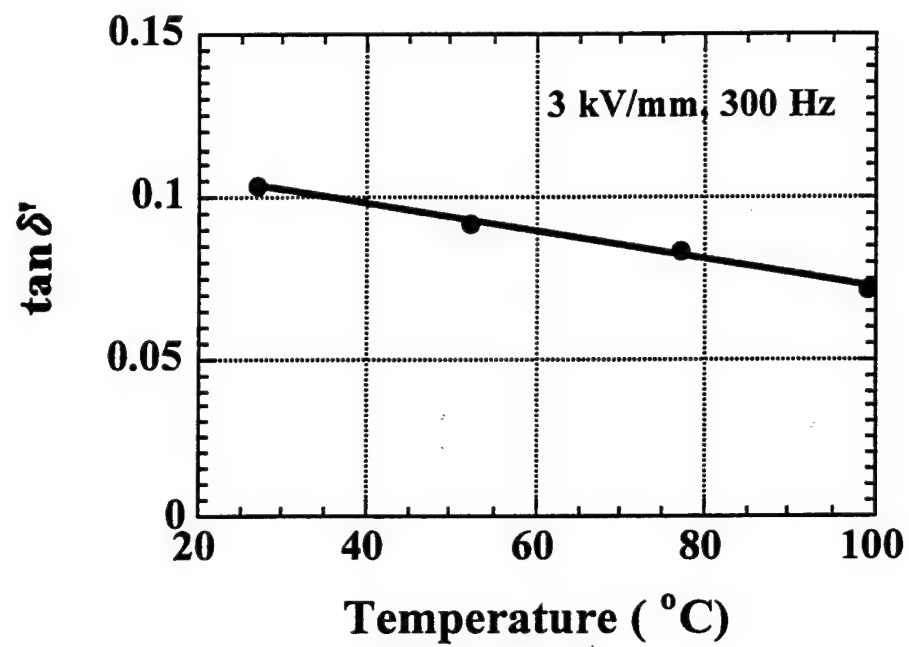
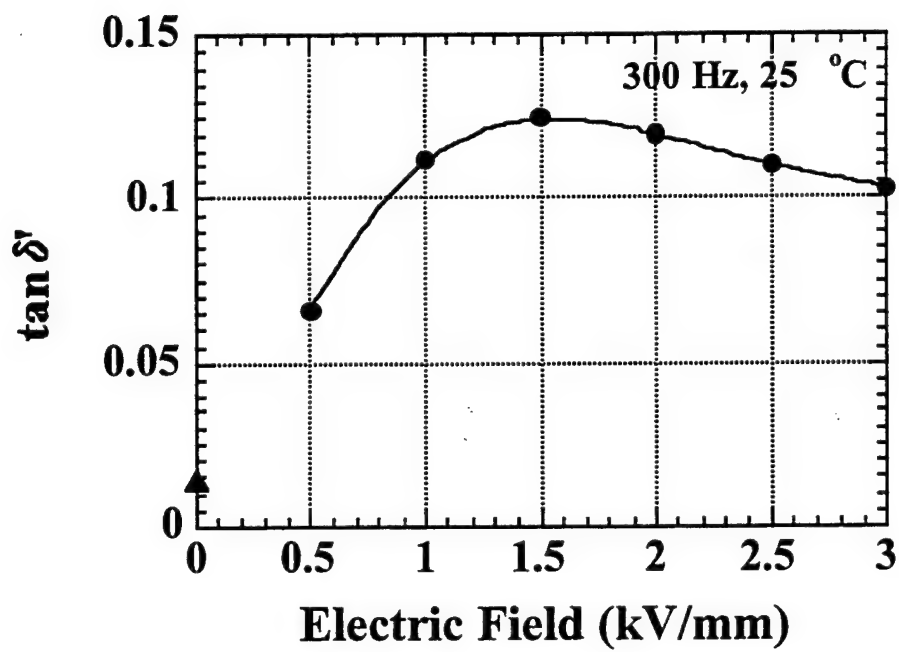Fig.2 Loss tan δ' as a function of sample temperature (3 kV/mm, 300 Hz).

Fig.3 Loss tan δ' as a function of electric field ($T = 25^{\circ}C$, f = 300 Hz).

Fig.4 Loss tan δ' as a funtion of frequency ($T = 25^{\circ}C$, $E = 2$ kV/mm).

Fig.5 Conceptual figure for explaining the relation between ε^X and ε^x, s^E and s^D.

Fig.6 Dissipation factors determined from (a) D vs. E (stress free), (b) x vs. X (short-circuit), (c) x vs. E (stress free) and (d) D vs. X (open-circuit) curves for a PZT based actuator.

Fig.7 Extrinsic piezoelectric dissipation factor $\tan\theta$' as a function of electric field or compressive stress, measured for a PZT based actuator.

Fig.8 Intrinsic loss factors, $\tan\delta$, $\tan\phi$ and $\tan\theta$ as a function of electric field or compressive stress, measured for a PZT based actuator.

Fig.9 Temperature rise for various actuators while driven at 300 Hz and 3 kV/mm.

Fig.10 Temperature rise versus V_e/A (3 kV/mm, 300 Hz), where V_e is the effective volume generating the heat and A is the surface area dissipating the heat.

Fig.11 $k(T)$ as a function of applied electric field (400 Hz, data from the actuator with dimensions of 7 mm x 7 mm x 2 mm).

Fig.12 Overall heat transfer coefficient $k(T)$ as a function of frequency.

Fig.13 Longitudinal vibration through the transverse piezoelectric effect (d_{31}) in a rectangular plate.

Fig.14 Strain generation in the resonance or antiresonance state. The strain magnitude is plotted in the vertical axis as a function of the x coordinate.

Fig.15 Equivalent circuit of a piezoelectric device for the resonance (a) and the antiresonance (b).

Fig.16 Mechanical Q_m versus basic composition x at two effective vibration velocities v_0=0.05 m/s and 0.5 m/s for $Pb(Zr_x Ti_{1-x})O_3$ doped with 2.1 at.% of Fe.

Fig.17 Vibration velocity dependence of the resistances R_d and R_m in the equivalent electric circuit for a PZT sample.

Fig.18 Vibration velocity dependence of the quality factor Q (Q_A,Q_B) and temperature rise for both A (resonance) and B (antiresonance) type resonances of a longitudinally vibrating PZT ceramic transducer through the transverse piezoelectric effect d_{31}.

29

Table I   Loss and overall heat transfer coefficient for PZT multilayer samples (E = 3 kV/mm, f = 300 Hz).

Actuator	4.5x3.5x2 mm	7x7x2 mm	17x3.5x1 mm
Total loss ($\times 10^3$ J/m^3) $$u = \frac{\rho c v}{f v_e} (\frac{dT}{dt})_{t->0}$$	19.2	19.9	19.7
P-E hysteresis loss ($\times 10^3$ J/m^3)	18.5	17.8	17.4
k(T) (W/m^{2}K)	38.4	39.2	34.1

Fig.1   (a) D vs. E (stress free), (b) x vs. X (short-circuit), (c) x vs. E (stress free) and

(d) D vs. X (open-circuit) curves with a slight hysteresis in each relation.

Fig.2   Loss tan δ' as a function of sample temperature (E = 3 kV/mm, f = 300 Hz).

Fig.3   Loss tan δ' as a function of electric field ($T = 25^{\circ}C$, f = 300 Hz).

Fig.4 Loss tan δ' as a funtion of frequency ($T = 25^{o}C$, $E = 2$ kV/mm).

Top row:

Total Input
Electrical Energy
$= (1/2)\, \varepsilon_0 \varepsilon^X E_0^2$

Stored
Electrical Energy
$= (1/2)\, \varepsilon_0 \varepsilon^X E_0^2$

Stored
Mechanical Energy
$= (1/2)\, (d^2/s^E) E_0^2$

Strain
$x = d\, E_0$

Mechanically
clamped

Electrically
short-circuited

Bottom row:

Total Input
Mechanical Energy
$= (1/2)\, s^E X_0^2$

Stored
Mechanical Energy
$= (1/2)\, s^D X_0^2$

Stored
Electrical Energy
$= (1/2)\, (d^2/\varepsilon_0 \varepsilon^X) X_0^2$

Current

Inverse
Field

Electrically
short-circuited

Electrically
open-circuited

Polarization
$P = d\, X_0$
Inverse field
$E = d X_0/\varepsilon_0 \varepsilon^X$

Fig. 5   Conceptual figure for explaining the relation between ε^X and ε^x, s^E and s^D.

Fig.6   Dissipation factors determined from (a) D vs. E (stress free), (b) x vs. X (short-circuit), (c) x vs. E (stress free) and (d) D vs. X (open-circuit) curves for a PZT based actuator.

Fig.7 Extrinsic piezoelectric dissipation factor tanθ' as a function of electric field or compressive stress, measured for a PZT based actuator.

Fig.8   Intrinsic loss factors, tanδ, tanφ and tanθ as a function of electric field or compressive stress, measured for a PZT based actuator.

Fig.9   Temperature rise for various actuators while driven at 300 Hz and 3 kV/mm.

Fig.10 Temperature rise versus V_e/A (3 kV/mm, 300 Hz), where V_e is the effective volume generating the heat and A is the surface area dissipating the heat.

Fig.11 k(T) as a function of applied electric field (400 Hz, data from the actuator with dimensions of 7 mm x 7 mm x 2 mm).

Fig.12 Overall heat transfer coefficient k(T) as a function of frequency.

Fig.13 Longitudinal vibration through the transverse piezoelectric effect (d_{31}) in a
rectangular plate.

Fig.14 Strain generation in the resonance or antiresonance state. The strain magnitude is plotted in the vertical axis as a function of the x coordinate.
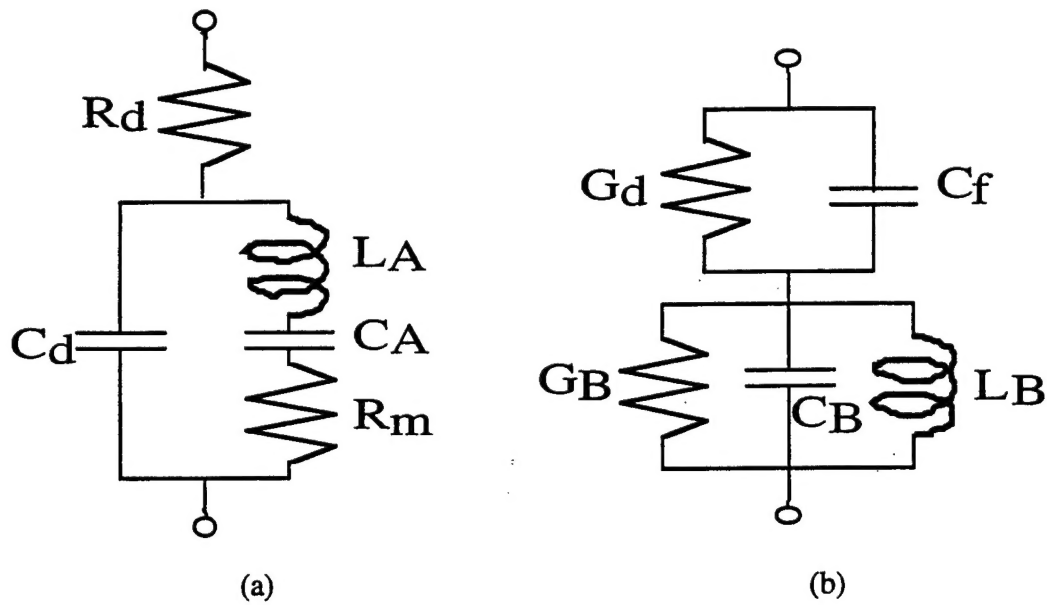
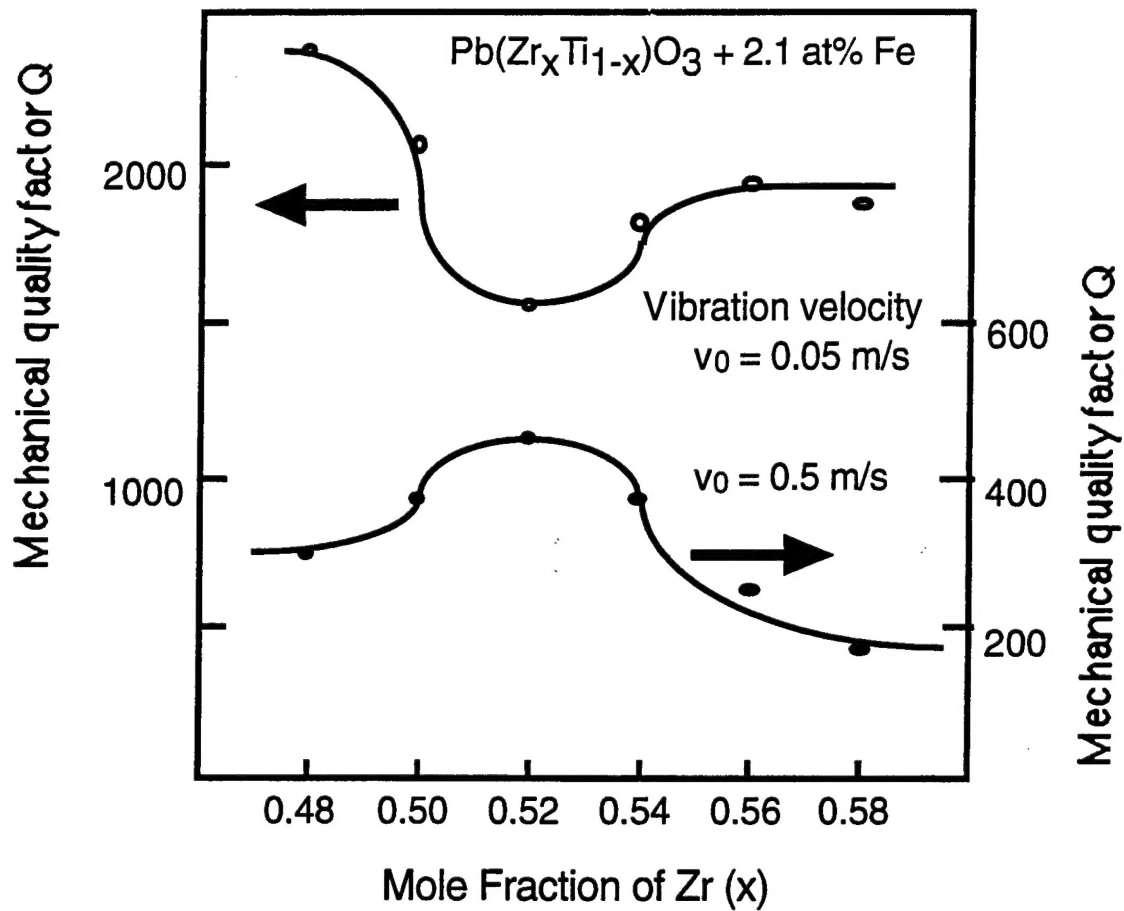Fig.15 Equivalent circuit of a piezoelectric device for the resonance (a) and the antiresonance (b).

Fig.16 Mechanical Q_m versus basic composition x at two effective vibration velocities v_0=0.05 m/s and 0.5 m/s for Pb(Zr$_x$Ti$_{1-x}$)O$_3$ doped with 2.1 at.% of Fe.
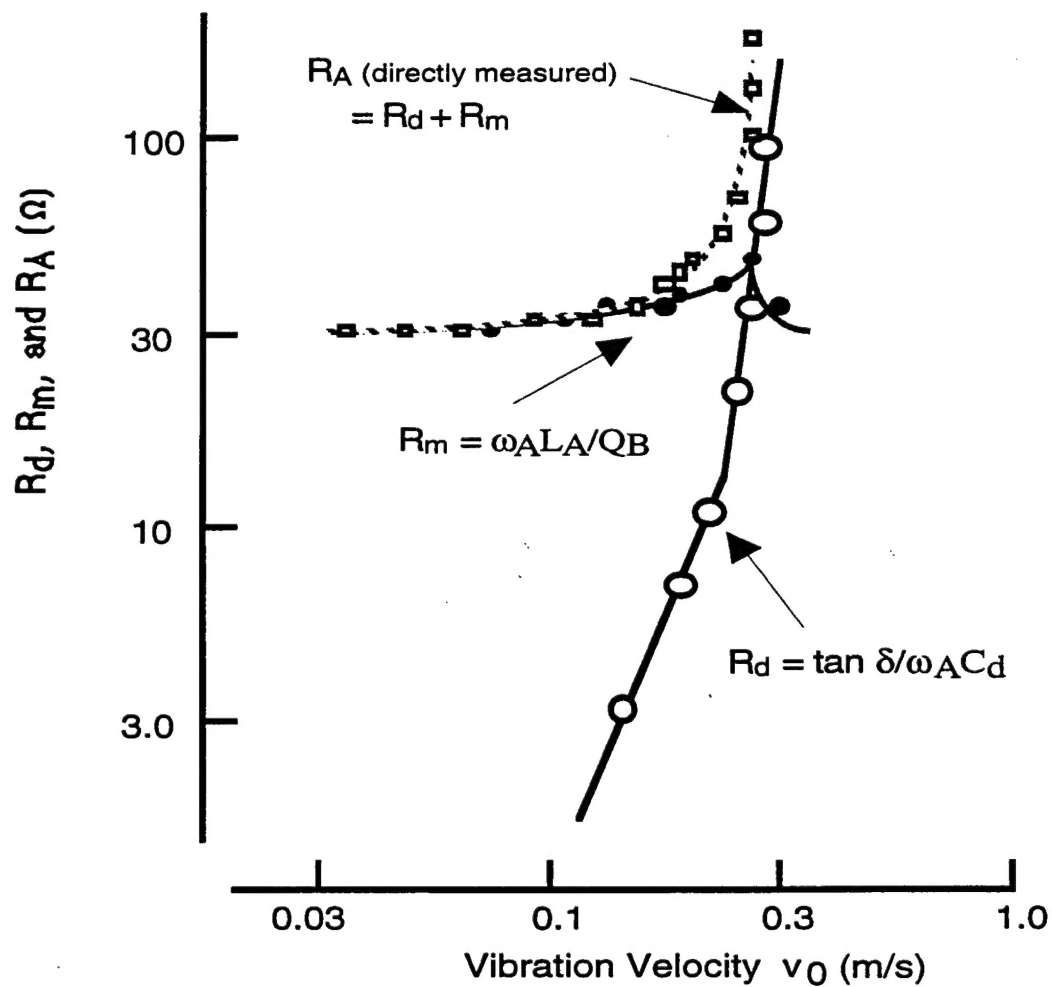
Fig.17 Vibration velocity dependence of the resistances R_d and R_m in the equivalent electric circuit for a PZT sample.
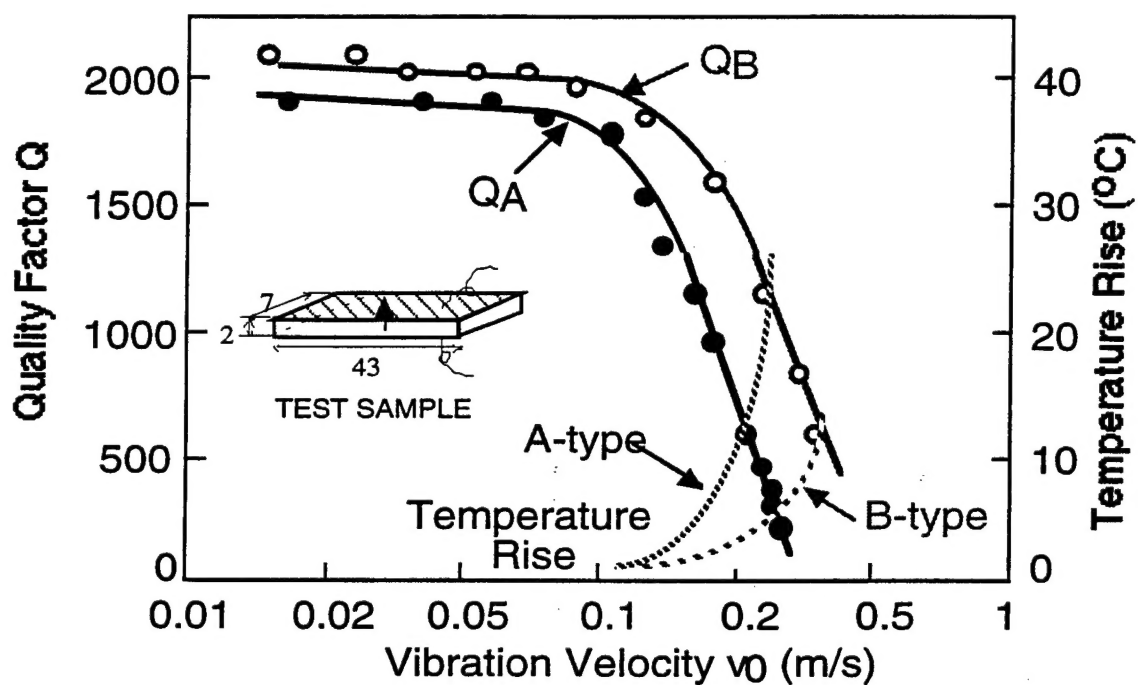
Fig.18 Vibration velocity dependence of the quality factor Q (Q_A, Q_B) and temperature rise for both A (resonance) and B (antiresonance) type resonances of a longitudinally vibrating PZT ceramic transducer through the transverse piezoelectric effect d_{31}.